Master Thesis

Antiferromagnetic Domains in presence of Magnetoelastic Interactions

Author
Bennet Karetta

1st Supervisor
Prof. Dr. Olena Gomonay
2nd Supervisor
Prof. Dr. Karin Everschor-Sitte

Faculty 08 - Institute for Physics
Johannes Gutenberg-Universität Mainz

Abstract

We show that magnetoelastic interactions in collinear antiferromagnets induce an anisotropy of the domain wall orientation for 180° and 90° domain walls. Further, we determine how the energy and size of these domain walls scale with the strength of the magnetoelastic coupling. With the obtained results, we demonstrate that closed 180° domain loops attempt to achieve a square shape due to the coupling. Finally, we verify that 180° and 90° domain walls can be pinned by frozen strains. The pining will be quantified by computing the corresponding pinning force and oscillation frequency of the lowest mode of an excited domain wall.

JOHANNES GUTENBERG UNIVERSITÄT MAINZ

INSPIRE group
INTERDISCIPLINARY SPINTRONICS RESEARCH

TWIST
Topological Whirls In SpinTronics

Ich versichere, dass ich die Arbeit "Antiferromagnetic Domains in presence of Magnetoelastic Interactions" selbstständig verfasst und keine anderen als die in der Arbeit angegebenen Quellen und Hilfsmittel benutzt sowie Zitate kenntlich gemacht habe.

I assure, that the thesis "Antiferromagnetic Domains in presence of Magnetoelastic Interactions" has been composed by me independently. No source materials or aids other than those mentioned have been used and all citations have been marked.

Mainz, den 01.05.2021
Bennet Karetta

Contents

1. Introduction

Every day countless amounts of data are created in our world. Thus, new storage devices are always required, which are smaller, faster and more stable than the preceding ones. In the research field of spintronics, spin properties are combined with electronics to tackle this problem [1–3]. The quantum nature of the spin allows to define data on small scales and to make memories stable and non-volatile [4]. Further spintronics devices do not require currents to maintain their state, which makes them highly energy efficient [5]. Spin currents allow to transport the spin states and thus the data through a material [6, 7]. Therefore, spintronic memory devices will be smaller, faster, and more stable compared to conventional electronic ones.

For a long time ferromagnets (FMs) have been the key component in spintronics devices [8–10]. In such FMs spins prefer to be aligned parallel to their neighbours [11]. Consequently, FMs have a total net magnetization and this magnetization can be manipulated by external magnetic fields or currents [12]. Information can be stored on a FM by defining bits 1 and 0 over two opposite directions of the magnetization [8] and it is possible to write and read the information easily [13–18]. However, FMs also bring some problems within their use as memory devices. The magnetization of the FM couples to all external magnetic fields [11]. External fields close to a FM memory and electromagnetic noise therefore may destroy the data. With the same argument the magnetic field coming from the FM itself (stray field) is a problem. The stray field of each magnetic bit will influence the other neighbouring bits and in order to minimize this effect the bits have to be placed sufficiently far away from each other. This gives a limitation in the operating speed of future FM devices [19]. Another issue is that the writing speed of FM devices is limited to the GHz regime and require large energies to exceed that limit [20–23]. This provides another limitation in how fast FM devices can be made in the future. For these reasons other materials are studied to replace FMs in memory devices and antiferromagnets (AFMs) are a promising candidate to fulfill this task [24–28] .

In an AFM spins align in an order such that the net magnetization of the AFM vanishes [29]. Information can then be stored by different orientations of that magnetic order [30, 31]. Due to the missing net magnetization, AFMs are not (or only weakly) influenced by disturbing magnetic fields [29] and thus more stable than FMs. Further AFMs do not produce stray fields since they

have no magnetization, which allows to place AFM bits much closer to each other compared to a FM memory [30]. AFM memory devices can therefore be made much smaller than FM ones. The natural frequencies of AFMs are usually in the THz regime [32, 33]. Thus, an AFM memory can be up to a thousand times faster than the FM ones. An important challenge is to understand the domain structure of AFMs as magnetic domains play a major role in spintonics memory devices [34–36]. In FMs the magnetic domains are formed due to the demagnetization energy [37] which provides a long range interaction in the crystal. This motivates the idea, that in general long range interactions are responsible for magnetic domains or at least have a significant influence on the domain structure. AFMs do not have a demagnetization energy [29] but still appear in multi-domain states [38] which then must have a different origin than in FMs. One long range interaction appearing in magnetic crystals comes from the magnetoelastic coupling. Elastic effects are always of a long range nature because deformation of an object at one position requires that the whole object is deformed in order not to break [39]. Due to a coupling of magnetic and elastic degrees of freedom [40–42] these long range interactions will also affect the magnetic profile. It has been shown that magnetic domains are formed in an AFM in presence of magnetoelastic interactions [38, 43]. To understand such an AFM multi-domain system we therefore have to study how magnetoelastic effects influence the domain structure and domain walls itself.

This work will focus on effects of the magnetoelastic coupling of a single domain wall in an infinite collinear AFM. We assume to be far below the critical temperature so we can apply a micromagnetic approach to describe the magnetic system [44]. The elastic system will be described by the infinitesimal strain theory as we assume only small deformations of the crystal [45]. A more detailed description of the system and how equilibrium states are found is given in chapter 2. In chapter 3 we study how the magnetoelastic coupling influences the energy of a domain wall of a 180° type (Sec. 3.1) and 90° type (Sec. 3.2). Also, in the chapter we determine the energy scaling with the strength of the coupling and compare the energies of the respective domain walls. Changes in the shape or thickness of a magnetic domain wall are investigated in chapter 4 with different types of strains and for a 180° domain wall (Sec. 4.1.1 and 4.2.1) and a 90° domain wall (Sec. 4.1.2 and 4.2.2). In chapter 5 we compute the shape of a closed 180° domain wall loop in presence of the magnetoelastic coupling. The mathematical foundation for this is build in sec. 5.1 and the energy of the loop is determined in sec. 5.2. The equilibrium shape of the loop is then calculated from that energy in sec. 5.3 and 5.4. Finally, in chapters 6 and 7 we show that strains can be used to pin a 90° and 180° domain wall respectively (sec. 6.1 and 7.1) and determine the forces which have to be applied to overcome the pinning (sec. 6.2 and 7.2).

2. Treatment of Magnetoelastic Coupling in Collinear Antiferromagnets

In an AFM the spins align in an order such that the net magnetization of the system is 0 in the equilibrium [29]. Thus, we define two ferromagnetic sublattices A and B with magnetizations $\mathbf{M}_A$ and $\mathbf{M}_B$ and the relation $|\mathbf{M}_A| = |\mathbf{M}_B| =: M_s$. We describe the system by the antiferromagnetic order parameter (Néel vector) $\mathbf{n} = (\mathbf{M}_A - \mathbf{M}_B)/(2M_s)$ and the normalized magnetization $\mathbf{m} = (\mathbf{M}_A + \mathbf{M}_B)/(2M_s)$. Note that we could also do the subtraction in $\mathbf{n}$ the other way around and the physics has to be the same. The Néel vector therefore always has a $\mathbb{Z}_2$ symmetry and it will thus appear at least quadratically in the energy density. We assume that the two sublattices are in a perfect antiparallel alignment where we have $\mathbf{m} = 0$ and then $\mathbf{n}^2 = 1$. Further we will consider an infinite AFM and work in a micromagnetic picture where $\mathbf{M}_A$ and $\mathbf{M}_B$ are continuous vector fields [46] which live in a Sobolev space [47].The Néel vector then is also a vector field $\mathbf{n} : \mathbb{R}^3 \to S^2$ with the same properties. As for the magnetization in FMs, the Néel vector has an exchange stiffness and gives minimal energy if it is constant over the whole space, as long as there are no other interactions present. Also crystal symmetries lead to anisotropies of the Néel vector i.e. axes along which the Néel vector minimizes (easy directions) or maximizes (hard directions) the energy [48]. In our case we consider an anisotropy with a strong hard axis along the z-direction and one or two easy axes in the xy-plane. The contributions of these interactions to the energy density are

$$\begin{aligned} \mathcal{W}_{\text{exch}} &= \frac{1}{2} A \partial_j \mathbf{n} \partial_j \mathbf{n} \\ \mathcal{W}_{\text{anis}} &= \frac{1}{2} K_{\parallel} n_z^2 - K_2 \mathscr{f}(n_x, n_y) \end{aligned} \tag{2.1}$$

with $A > 0$ and $K_1 \gg K_2 > 0$. The Einstein sum convention was used and the sums goes over x, y and z. The dimensionless anisotropy function $\mathscr{f} : [-1, 1]^2 \to \mathbb{R}_{\geq}$ will be specified for the particular problems respectively. Since $\mathbf{n}$ is not necessarily differentiable, the derivatives ∂_i correspond to weak derivatives.
Another contribution into the energy of the crystal apart from the magnetic

ordering comes from deformations of atoms in the lattice from equilibrium. We assume that the AFM crystal is homogeneous. On length scales, where the micromagnetic approach is valid, the displacements of the atoms are small and we can use the concepts of linear elasticity [49]. Deformations in the crystal are then also described by a continuous vector field $\mathbf{u} : \mathbb{R}^3 \to \mathbb{R}^3$, which we call displacement. In a deformed medium it returns the vector pointing from the initial equilibrium position of each space point to its current one. The strains of the crystal in this theory are then given by a tensor $\hat{u} : \mathbb{R}^3 \to \mathbb{R}^{3\times3}$ over the relation $u_{ij} = 1/2(\partial_i u_j + \partial_j u_i)$ for $i, j \in \{x, y, z\}$. In its most general form, the energy density of the deformed system within the regime of linear elasticity and in terms of the strain tensor is given by

$$\mathcal{W}_{\text{elas}} = \mu_{ijkl} u_{ij} u_{kl}. \tag{2.2}$$

[39, 50] For simplicity we will consider an isotropic medium i.e. a medium, where deformations in all directions are similar and the energy density is invariant under all rotations. In this case we have $\mu_{ijkl} = \mu(\delta_{ik}\delta_{jl} + \delta_{il}\delta_{jk}) + \frac{2\mu\nu}{1-2\nu}\delta_{ij}\delta_{kl}$ [39, 50] and therefore

$$\begin{aligned}\mathcal{W}_{\text{elas}} =& \frac{\mu(1-\nu)}{1-2\nu}(u_{xx}^2 + u_{yy}^2 + u_{zz}^2) + \frac{2\mu\nu}{1-2\nu}(u_{xx}u_{yy} + u_{yy}u_{zz} + u_{zz}u_{xx}) \\ &+ 2\mu(u_{xy}^2 + u_{yz}^2 + u_{zx}^2),\end{aligned} \tag{2.3}$$

with the shear modulus μ and the Poisson ratio ν.
Magnetic and elastic degrees of freedom are coupled [40] and we can formulate the contribution to the energy density in the general form

$$\mathcal{W}_{\text{me}} = \lambda_{ijkl} u_{ij} n_k n_l, \tag{2.4}$$

where strains and Néel vector are written in their lowest possible order (cf. [51] for FMs). Within the picture of an elastically isotropic crystal we can specify this term to

$$\mathcal{W}_{\text{me}} = \lambda \left[(u_{xx} - u_{yy})(n_x^2 - n_y^2) + 4n_x n_y u_{xy}\right]. \tag{2.5}$$

(cf. [52, 53]) where we neglected terms with n_z due to the strong anisotropy along z.
In order to analyse the influence of the magnetoelastic interaction in multidomain systems, we would have to minimize the energy functional, including all the mentioned contributions in the integrand, with respect to Néel vector

and strains for a given multi-domain system. This turns out to be quite difficult due to the complexity of the energy density and the number of degrees of freedom in the Néel vector and strain tensor. We therefore attempt a different approach in which we "guess" a solution for the multi-domain system and then compute corrections to it. Equation 2.5 suggests that in presence of a magnetic ordering the magnetoelastic coupling produces strains inside of the AFM. In AFM multi-domain systems and on length scales much larger than the sizes of domain walls we can assume that the strains correspond to a magnetic profile of a step-like domain wall. This idea has already been used in studies for FMs [54,55] and therefore motivates to do the same here. A domain wall can then be viewed as an elastic defect and we can find the strains of the different domains with a method similar to the Eshelby inclusion [56,57]. We first consider the strains which would correspond to a mono-domain state in each domain respectively. They have the form

$$\begin{aligned} u_{xx} &= -\frac{\lambda}{2\mu}(n_x^2 - n_y^2) \\ u_{yy} &= \frac{\lambda}{2\mu}(n_x^2 - n_y^2) \\ u_{xy} &= -\frac{\lambda}{2\mu}(2n_x n_y) \end{aligned} \tag{2.6}$$

(cf. appendix A) for each domain where all other strain tensor components are 0. At the domain wall the strain tensor components flip step-like between the strains corresponding the two domains. In the following we call such a strain profile spontaneous strain $\hat{u}^{\text{spon}}$. When all domains deform independently according to the respective spontaneous strains, it is possible that the domains deform into each other or break at some positions. This is not possible in reality and produces stresses in the system. Mathematically, we describe this over the incompatibility of the strains. Due to their definition as a symmetric gradient strains have to be "compatible" i.e.

$$\text{inc}(\hat{u}) := (-\epsilon_{ikl}\epsilon_{jmn}\partial_k\partial_m u_{ln})_{i,j=x,y,z} = 0.$$

In a situation of nonphysical deformations, when the spontaneous strains require additional stresses, this incompatibility operator does not return 0 at the domain wall, when it is applied onto the spontaneous strain. Therefore, we need to add another strain $\hat{u}^{\text{comp}}$ in the total strain profile which compensates the incompatibility of the spontaneous strain at the domain walls, such that the incompatibility of the sum of both strains is 0. Physically the new strain arises from the nonzero stress. On shorter length scales, where the domain wall cannot be considered step-like anymore we receive another additional strain contribution from the magnetoelastic coupling localised at the domain wall,

to account for the inhomogeneities of the Néel vector at the domain walls. We call these strains relative strains $\hat{u}^{\text{rel}}$ and compute them by minimizing the energy functional with respect to their corresponding displacement field. For this we first rewrite the elastic energy

$$\mathcal{W}_{\text{elas}} = \mathcal{W}_{\text{elas}}^{\text{spon}} + \mathcal{W}_{\text{elas}}^{\text{rel}} + \mu(u_{xx}^{\text{spon}} - u_{yy}^{\text{spon}})(u_{xx}^{\text{rel}} - u_{yy}^{\text{rel}}), \tag{2.7}$$

where $\mathcal{W}_{\text{me}}^{\text{spon}}$ is the elastic energy if we only apply the spontaneous strain and similar for $\mathcal{W}_{\text{elas}}^{\text{rel}}$. The compensating strains were absorbed in $\hat{u}^{\text{spon}}$ and we also used $u_{xx}^{\text{spon}} + u_{yy}^{\text{spon}} = 0$ which can be obtained from the solution of the homogeneous state. From this term together with the other energy contributions we can now write down the equilibrium conditions for our system by minimizing the energy functional with respect to the Néel vector $\mathbf{n}$ and the displacement associated to the relative strains $\mathbf{u}^{\text{rel}}$. The differential equations we have to solve then are

$$0 = \mathbf{n} \times \left[\frac{\delta \int (\mathcal{W}_{exch} + \mathcal{W}_{anis} + \mathcal{W}_{me}) d^3r}{\delta n_i} \mathbf{e}_i \right] \tag{2.8}$$

$$\nabla^2 \mathbf{u}^{\text{rel}} + \frac{1}{1-2\nu} \nabla(\nabla \cdot \mathbf{u}^{\text{rel}}) = \frac{\mathbf{f}}{\mu} - (\mathbf{e}_x \partial_x - \mathbf{e}_y \partial_y)(u_{xx}^{\text{spon}} - u_{yy}^{\text{spon}}), \tag{2.9}$$

for $f_j = \delta \int \mathcal{W}_{\text{me}}^{\text{rel}} d^3r / \delta u_j^{\text{rel}}$. This reduces the problem from the initial 3+9 degrees of freedom to 3+3. We can even go further by considering $\mathbf{n}^2 = 1$ together with the strong hard z-axis. The Néel vector will always be aligned in the xy-plane and has a constant length i.e. it is fully described by an angle in the plane. Therefore we write $\mathbf{n} = \mathbf{e}_x \cos\phi + \mathbf{e}_y \sin\phi$ and the corresponding energy terms then turn into

$$\begin{aligned} \mathcal{W}_{\text{exch}} &= \frac{1}{2} A (\nabla\phi)^2 \\ \mathcal{W}_{\text{anis}} &= -K_2 \not{\ell}(\phi) \\ \mathcal{W}_{\text{me}} &= \lambda \left[(u_{xx} - u_{yy}) \cos(2\phi) + 2u_{xy} \sin(2\phi) \right], \end{aligned}$$

for a new scalar field $\phi : \mathbb{R}^3 \to \mathbb{R}$. A functional minimization with respect to ϕ rephrases equation 2.8 and yields

$$A\nabla^2\phi = -K_2 \frac{d\not{\ell}}{d\phi} + 2\lambda \left[-(u_{xx} - u_{yy}) \sin(2\phi) + 2u_{xy} \cos(2\phi) \right]. \tag{2.10}$$

Equations 2.9 and 2.10 now allow us to study the effect of the magnetoelastic coupling on multi-domain systems for which we begin with a study of flat static domain walls.

3. Energy and Orientation of Magnetic Domain Walls

3.1. 180° Domain Wall with Uniaxial Anisotropy

In an infinite AFM with only exchange interaction and anisotropy we have a global translational and rotational invariance of the space variables. In other words, the energy does not change under the transformation $\phi(\mathbf{r}) \to \phi(\hat{R} \cdot \mathbf{r} + \boldsymbol{\rho})$ $\forall \mathbf{r}, \boldsymbol{\rho} \in \mathbb{R}^3$, $\hat{R} \in \mathrm{SO}(3)$ in the energy density. Thus, it does not make a difference, where the domain wall is located in a two domain system with a flat domain wall. We cannot generalize this statement to the term with the magnetoelastic coupling, due to the interaction of the independent degrees of freedom. Therefore, the first thing to investigate is whether the position of a domain wall has an influence on the energy due to the presence of magnetoelastic interactions. Since the AFM in our model is infinite we still have translational invariance and only a rotation of the domain wall in the easy plane may produce a new effect. We start by looking at a 180° domain wall in the system which was described in the previous section. To stabilize the domain wall we introduce a uniaxial anisotropy along the x-axis i.e. we use $\mathscr{f} := \mathscr{f}_{180}$ with

$$\begin{aligned} \mathscr{f}_{180}(n_x, n_y) &= \frac{1}{2} n_x^2 \\ \mathscr{f}_{180}(\phi) &= \frac{1}{2} \cos^2 \phi \\ \frac{d\mathscr{f}_{180}}{d\phi} &= -\frac{1}{2} \sin(2\phi). \end{aligned} \tag{3.1}$$

The equilibrium domains in this system are $\phi = 0$ and $\phi = \pi$ and the we consider a magnetic profile with a flat domain wall between these two equilibrium domains. Both domains have the same spontaneous strain, so $\hat{u}^{\mathrm{spon}}$ is a constant with

$$u_{xx}^{\mathrm{spon}} - u_{yy}^{\mathrm{spon}} = -\frac{\lambda}{\mu} \tag{3.2}$$

and all other tensor components equal 0. The incompatibility of the strain at the domain wall is therefore 0 for all orientations of the domain wall and we

have no contribution of a compensating strain. For the additional strains at the domain wall we describe the system in the domain wall coordinates (ξ, η, z), where ξ is the direction normal to the domain wall and η is orthogonal to ξ and z. The relation between (ξ, η) and (x, y) is a rotation by an angle ψ about the z-axis

$$\begin{aligned}\xi &= x\cos\psi - y\sin\psi \\ \eta &= x\sin\psi + y\cos\psi.\end{aligned}$$

The transformation (x, y) $\rightarrow$ (ξ, η) affects only the magnetoelastic coupling term in the energy density because the purely elastic energy is invariant under rotations and ϕ as a scalar field also does not change. The strains of the coupling term in the new coordinate system are related to the ones in the initial system over

$$\begin{aligned}u_{\xi\xi} - u_{\eta\eta} &= (u_{xx} - u_{yy})\cos(2\psi) - 2u_{xy}\sin(2\psi) \\ 2u_{\xi\eta} &= (u_{xx} - u_{yy})\sin(2\psi) + 2u_{xy}\cos(2\psi)\end{aligned} \tag{3.3}$$

and equations 2.9 and 2.10 become

$$A\nabla^2\phi = -\frac{1}{2}K_2\sin(2\phi) + 2\lambda\left[-(u_{\xi\xi} - u_{\eta\eta})\sin(2(\phi+\psi)) + 2u_{\xi\eta}\cos(2(\phi+\psi))\right] \tag{3.4}$$

$$\nabla^2\mathbf{u}^{\mathrm{rel}} + \frac{1}{1-2\nu}\nabla(\nabla\cdot\mathbf{u}^{\mathrm{rel}}) = \frac{1}{\mu}\mathbf{f} \tag{3.5}$$

where ∇ consists of derivatives in the new coordinate system. $\mathbf{f}$ takes the form

$$\begin{aligned}f_\xi &= -\lambda\left[\partial_\xi\cos(2(\phi+\psi)) + \partial_\eta\sin(2(\phi+\psi))\right] \\ f_\eta &= -\lambda\left[\partial_\xi\sin(2(\phi+\psi)) - \partial_\eta\cos(2(\phi+\psi))\right] \\ f_z &= 0\end{aligned}$$

At $\xi \rightarrow \pm\infty$ the angle ϕ and $\hat{u}$ converge to the values of the respective equilibrium domain. In this case the boundary conditions for the 180° domain wall are

$$\xi \rightarrow \pm\infty: \;\; \phi \rightarrow 0, \pi, \;\; \partial_\xi\phi \rightarrow 0, \;\; \hat{u} \rightarrow \hat{u}^{\mathrm{spon}}.$$

Since the strains have the value of the spontaneous strain at infinity, $\hat{u}^{\mathrm{rel}}$ approaches 0 at infinity. With this condition we can solve eq. 3.5 in the Fourier

space to receive $\hat{u}^{\mathrm{rel}}$ (see appendix B). When we further define $\nu_e := 1 + \frac{1}{1-2\nu}$ the solution is

$$\begin{aligned} u^{\mathrm{rel}}_{\xi\xi} &= -\frac{\lambda}{\mu\nu_e}\left[\cos(2(\phi+\psi)) - \cos(2\psi)\right] \\ u^{\mathrm{rel}}_{\xi\eta} &= -\frac{\lambda}{2\mu}\left[\sin(2(\phi+\psi)) - \sin(2\psi)\right] \end{aligned} \tag{3.6}$$

and all other strains tensor components are 0. This solution can be used to receive a closed equation for ϕ by plugging $\hat{u} = \hat{u}^{\mathrm{spon}} + \hat{u}^{\mathrm{rel}}$ into eq. 3.4

$$\begin{aligned} A\partial_\xi^2\phi &= \frac{1}{2}K_2\sin(2\phi) + 2\frac{\lambda^2}{\mu}\sin(2(\phi+\psi))\left[\cos(2\psi) + \frac{1}{\nu_e}(\cos(2(\phi+\psi)) - \cos(2\psi))\right] \\ &\quad - 2\frac{\lambda^2}{\mu}\cos(2(\phi+\psi))\left[\sin(2\psi) + (\sin(2(\phi+\psi)) - \sin(2\psi))\right] \\ &= \frac{1}{2}K_2\sin(2\phi) - 2\frac{\lambda^2}{\mu}\left(1 - \frac{1}{\nu_e}\right)\sin(2(\phi+\psi))\left[\cos(2(\phi+\psi)) - \cos(2\psi)\right]. \end{aligned} \tag{3.7}$$

Together with the boundary conditions for ϕ we can calculate the first integral of the differential equation

$$\frac{1}{2}A(\partial_\xi\phi)^2 = \frac{1}{2}K_2\sin^2\phi + \frac{\lambda^2}{2\mu}\left(1 - \frac{1}{\nu_e}\right)\left[\cos(2(\phi+\psi)) - \cos(2\psi)\right]^2 =: \mathcal{W}_{\mathrm{DW}} \tag{3.8}$$

The lefthandside of eq. 3.8 corresponds to the exchange energy and the righthandside to the anisotropy and the minimum of elastic and magnetoelastic energy with respect to strains. The energy density $\mathcal{W}$ of the system after minimization with respect to the strains is therefore given by $\mathcal{W} = 2\mathcal{W}_{\mathrm{DW}}$. On the first sight, it might seem as if $\mathcal{W}$ is still invariant under the space variable transformation $\phi(\mathbf{r}) \to \phi(\hat{R}\cdot\mathbf{r} + \boldsymbol{\rho})$ as discussed in the beginning because it now only depends on ϕ. This is not the case because such a transformation also changes the boundary conditions and therefore the definition of the axis ξ and the angle ψ which is part of the energy density $\mathcal{W}$. We therefore know, that the energy of the magnetoelastic system is influenced by the alignment of the domain wall. To determine how the energy of the system depends on the domain wall orientation ψ we have to integrate $\mathcal{W}$ along the ξ-axis for different angles of ψ to receive the energy per unit area W. The integral can be simplified to an integral of ϕ over

$$W = \int_{-\infty}^{\infty}\mathcal{W}d\xi = \int_0^\pi \mathcal{W}\frac{d\xi}{d\phi}d\phi = \int_0^\pi \mathcal{W}(\partial_\xi\phi)^{-1}d\phi = \int_0^\pi 2\sqrt{A\cdot\mathcal{W}_{\mathrm{DW}}}d\phi, \tag{3.9}$$

where without loss of generality derivative of ϕ was chosen to be positive. The integral of eq. 3.9 is computed numerically and normalized by the energy corresponding to the $\psi = 0$ solution. For a qualitative analysis, we set the parameters A and K_2 to 1 and $1/\nu_e = 1/2$ as the Poisson ratio varies between 0 and 0.5 for most materials [58]. The specific choice for ν_e will only influence the numeric values of the energy but no qualitative results. The integral solutions for different dimensionless strengths of magnetoelastic coupling $u_0 := \lambda^2/(\mu K_2)$ are shown in Fig. 3.1, where we can observe energy minima for $\psi = \pi/4$ and $\psi = 3\pi/4$. This can be generalized to energy minimal for all $\psi = \pi/4 + \pi/2 \cdot \mathbb{N}$. We therefore have a domain wall anisotropy and domain walls prefer to be aligned along the $(x+y)$-axis or $(x-y)$-axis. This anisotropy comes from the internal strains localized at the domain wall which are different for the different domain wall orientations. To verify this result also for finite samples, the system was also simulated with MuMax3 [59]. The details are presented in the appendix C.1 and the simulations provided similar results for the domain wall anisotropy. Due to the choice of an 180° domain wall we did not have any incompatibilities and no effects of the compensating strains. In the next section we investigate how the domain wall anisotropy is affected in presence of possible incompatibilities.

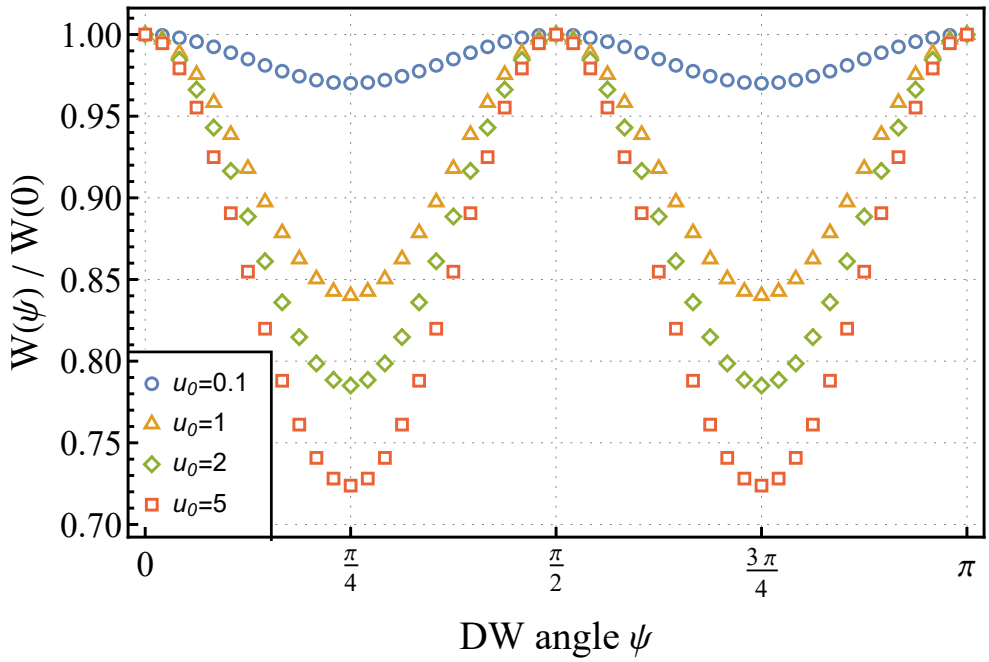

Figure 3.1.: Energy per unit area in the ηz-plane for a 180° domain wall plotted against the domain wall orientation angle ψ for different values of the dimensionless magnetoelastic coupling parameter u_0. The errors from the numerical integration are to small to be shown.

3.2. 90° Domain Wall with In Plane Anisotropy

To also study the effects of incompatibility on the equilibrium domain wall orientation, we have to consider a non 180° domain wall. The simplest case is a 90° wall which we stabilize with two orthogonal easy axes in the xy-plane. Thus, we use the anisotropy function $\mathscr{f} := \mathscr{f}_{90}$ with

$$\begin{aligned} \mathscr{f}_{90}(n_x, n_y) &= \frac{1}{4}\left(n_x^4 + n_y^4\right) \\ \mathscr{f}_{90}(\phi) &= \frac{1}{4}\left(\cos^4\phi + sin^4\phi\right) \\ \frac{d\mathscr{f}_{90}}{d\phi} &= -\frac{1}{4}\sin(4\phi). \end{aligned} \tag{3.10}$$

The possible domains in this case are $\phi = 0, \pi/2, \pi, 3\pi/2$. For a domain wall from $\phi = 0$ to $\phi = \pi/2$ along the axis $\xi = x\cos\psi + y\sin\psi$ as in sec. 3.1 the spontaneous strains are

$$\begin{aligned} u_{xx}^{\text{spon}} &= \frac{\lambda}{2\mu}\Theta\left(\frac{\xi}{x_{\text{el}}}\right) \\ u_{yy}^{\text{spon}} &= -\frac{\lambda}{2\mu}\Theta\left(\frac{\xi}{x_{\text{el}}}\right) \end{aligned} \tag{3.11}$$

and 0 for all other components of the strain tensor. The length scale x_{el} is chosen to be significantly larger than the domain wall width $x_{\text{DW}} = \sqrt{\frac{A}{K_2}}$ (For more details on the domain wall width see chapter 4.) and the shape function Θ is defined as a sign function ($\Theta(\alpha) := \alpha/|\alpha|$ for $\alpha \neq 0$). The incompatibility of such a spontaneous strain is

$$\begin{aligned} \left(\text{inc}\left(\hat{u}^{\text{spon}}\right)\right)_{ij} &= -\epsilon_{ikl}\epsilon_{jmn}\partial_k\partial_m u_{ln}^{\text{spon}} \\ &= -\epsilon_{ixy}\epsilon_{jxy}\partial_x\partial_x u_{yy}^{\text{spon}} - \epsilon_{iyx}\epsilon_{jyx}\partial_y\partial_y u_{xx}^{\text{spon}} \\ &= -\delta_{iz}\delta_{jz}(\partial_x^2 u_{yy}^{\text{spon}} + \partial_y^2 u_{xx}^{\text{spon}}) \\ &= -\frac{\lambda}{\mu}\delta_{iz}\delta_{jz}\left(\frac{\cos^2\psi - \sin^2\psi}{x_{\text{el}}^2}\right)\delta'\left(\frac{x\cos\psi - y\sin\psi}{x_{\text{el}}}\right) \\ &= -\frac{\lambda}{\mu x_{\text{el}}^2}\cos(2\psi)\delta_{iz}\delta_{jz}\delta'\left(\frac{x\cos\psi - y\sin\psi}{x_{\text{el}}}\right) \end{aligned}$$

The strain to compensate the incompatibility fulfils $\text{inc}\left(\hat{u}^{\text{comp}}\right) = -\text{inc}\left(\hat{u}^{\text{spon}}\right)$ and it can be determined over the formula introduced by Eshelby [60]

$$\hat{u}^{\text{comp}}(\mathbf{r}) = \frac{1}{4\pi}\int_{\mathbb{R}^3} d^3r' \frac{\text{inc}\left(\hat{u}^{\text{comp}}(\mathbf{r}')\right) - \text{tr}\left[\text{inc}\left(\hat{u}^{\text{comp}}(\mathbf{r}')\right)\right]\mathbb{I}_{3\times 3}}{|\mathbf{r} - \mathbf{r}'|}$$

with the 3×3 identity matrix $\mathbb{I}_{3\times3}$. Without further calculations we see $u_{xx}^{\text{comp}} = u_{yy}^{\text{comp}}$ are the only nonvanishing components of $\hat{u}^{\text{comp}}$. For them we find

$$\begin{aligned}
u_{xx}^{\text{comp}}(\mathbf{r}) &= -\frac{\lambda}{4\pi\mu x_{\text{el}}^2}\cos(2\psi)\int_{\mathbb{R}^3} dx'dy'dz' \frac{\delta'\left((x'\cos\psi - y'\sin\psi)/x_{\text{el}}\right)}{\sqrt{(x-x')^2+(y-y')^2+(z-z')^2}} \\
&= -\frac{\lambda}{4\pi\mu x_{\text{el}}^2}\cos(2\psi)\int_{\mathbb{R}^3} d\xi'd\eta'dz' \frac{\delta'\left(\xi'/x_{\text{el}}\right)}{\sqrt{(\xi-\xi')^2+(\eta-\eta')^2+(z-z')^2}} \\
&= \frac{\lambda}{4\pi\mu}\cos(2\psi)\int_{\mathbb{R}^2} d\eta'dz' \frac{\xi/x_{\text{el}}}{(\eta'^2+z'^2)^{3/2}} \\
&= \frac{\lambda}{2\mu}\cos(2\psi)\Theta\left(\frac{\xi}{x_{\text{el}}}\right)
\end{aligned}$$

The strains go quadratically into the energy density (cf. equations 2.3 and 2.7) and the energy of the domain wall system is therefore minimal at the minima of $\cos^2(2\psi)$ i.e. for the same orientations as the 180° domain wall ($\psi = \pi/4 + \pi/2\cdot\mathbb{N}$) when the incompatibility of the spontaneous strain is zero. The relative strains at the domain wall were neglected because the energy of strains located at the domain wall scales with the size of the wall. The energy contribution from the compensating strains on the other hand scales with the domain size because the strains itself are constant in the respective domains. Usually the size of the domains much larger (infinite in our case) than the domain wall and the contribution of compensating strains is therefore dominant and responsible for the domain wall anisotropy. The system was also simulated (appendix C.2), where we receive the same result and demonstrate the dominance of incompatibility over relative strains in the domain wall anisotropy. This result implies, that the magnetoelastic coupling induces an anisotropy for all kinds of flat domain walls in the system either from incompatibilities or relative strains at the domain wall.

3.3. Minimum Energies of the Domain Walls

When the energies of the domain walls are minimal i.e. the domain wall is placed on of its axes it is possible to compare both 180° and 90° cases, because both systems have no incompatibilities of spontaneous strain. In order to compare the domain wall energies in our two systems quantitatively, we compute the energy for both the 90° and 180° domain wall without loss of generality for $\psi = \pi/4$.
For the 180° domain wall we have to compute the integral from eq. 3.9 with the fixed value of ψ. We receive

$$\begin{aligned} W_{180} &= \int_0^\pi 2\sqrt{\left(\frac{1}{2}K_2 \sin^2\phi + \frac{\lambda^2}{2\mu}\left(1-\frac{1}{\nu_e}\right)\sin^2(2\phi)\right)} \\ &= \sqrt{2AK_2}\left(\sqrt{(1+4u_\nu)} + \frac{1}{2\sqrt{u_\nu}}\operatorname{arcsinh}(2\sqrt{u_\nu})\right) \end{aligned} \tag{3.12}$$

with $u_\nu := u_0(1-1/\nu_e)$. For the energy of the 90° domain wall, we still have to reformulate the problem to have a closed equation for ϕ. The boundary conditions for a 90° domain wall system can be formulated in the following way

$$\xi \to \pm\infty: \ \phi \to 0, \pi/2, \ \partial_\xi \phi \to 0, \ \hat{u} \to \hat{u}^{\text{spon}}$$

with $2u_{\xi\eta}^{\text{spon}} = \lambda/\mu\ \Theta$ and 0 for all the other components of the matrix. Such spontaneous strain profile follows directly from eq. 3.3 and 3.11. First we have to determine the relative strains which works similar to sec. 3.1 with the condition that $\hat{u}^{\text{rel}}$ approaches 0 at $\xi \to \pm\infty$. The calculations in Fourier space are again in the Appendix B. Note that we only write Θ for the shape function and the argument ξ/x_{el} is included implicitly. The strains then take the form

$$\begin{aligned} u_{\xi\xi} &= \frac{\lambda}{\mu\nu_e}\sin(2\phi) \\ u_{\xi\eta} &= -\frac{\lambda}{2\mu}\left[\cos(2\phi)+\Theta\right]. \end{aligned} \tag{3.13}$$

Similar to sec. 3.1 we find a closed equation for ϕ by plugging $\hat{u} = \hat{u}^{\text{spon}} + \hat{u}^{\text{rel}}$ into eq. 3.4.

$$\begin{aligned} A\partial_\xi^2\phi &= \frac{1}{4}K_2\sin(4\phi) + 2\lambda\Big[-(u_{\xi\xi}-u_{\eta\eta})\sin(2(\phi+\frac{\pi}{4})) \\ &\qquad +2u_{\xi\eta}\cos(2(\phi+\frac{\pi}{4}))\Big] \\ &= \frac{1}{4}K_2\sin(4\phi) - 2\frac{\lambda^2}{\mu}\frac{1}{\nu_e}\cos(2\phi)\sin(2\phi) \\ &\qquad - 2\frac{\lambda^2}{\mu}\sin(2\phi)\left[\Theta-(\cos(2\phi)+\Theta)\right] \\ &= \frac{1}{4}K_2\sin(4\phi) + 2\frac{\lambda^2}{\mu}\left(1-\frac{1}{\nu_e}\right)\sin(2\phi)\cos(2\phi) \end{aligned} \tag{3.14}$$

Together with the boundary conditions for ϕ we can determine the first integral to reformulate the problem in a first order differential equation. The result is

$$\begin{aligned}\frac{1}{2}A(\partial_\xi\phi)^2 &= \frac{1}{8}K_2\sin^2(2\phi) + \frac{\lambda^2}{2\mu}\left(1-\frac{1}{\nu_e}\right)\sin^2(2\phi)\\ &= \left(\frac{1}{8}K_2 + \frac{\lambda^2}{2\mu}\left(1-\frac{1}{\nu_e}\right)\right)\sin^2(2\phi)\end{aligned} \tag{3.15}$$

The energy of the domain wall can be found with a similar integration of ϕ as before but now the integration goes from 0 to $\pi/2$ and for $\mathcal{W}_{\mathrm{DW}}$ we use the righthandside of eq. 3.15. The result of the integration leads to the energy per unit area

$$\begin{aligned}W_{90} &= \int_0^{\pi/2} 2\sqrt{A\left(\frac{1}{8}K_2 + \frac{\lambda^2}{2\mu}\left(1-\frac{1}{\nu_e}\right)\right)}\sin(2\phi)d\phi\\ &= 2\sqrt{A\left(\frac{1}{8}K_2 + \frac{\lambda^2}{2\mu}\left(1-\frac{1}{\nu_e}\right)\right)}\\ &= \sqrt{\frac{AK_2}{2}(1+4u_\nu)}.\end{aligned} \tag{3.16}$$

We can directly see that the energy of the 180° domain wall is larger than the energy of the 90° wall for all values of u_ν. The ratio of both energies reads as

$$\frac{W_{180}}{W_{90}} = 2 + \frac{\operatorname{arcsinh}(2\sqrt{u_\nu})}{\sqrt{u_\nu(1+4u_\nu)}} \tag{3.17}$$

and is plotted in Fig. 3.2. For $u_\nu \to 0$ i.e. $\lambda \to 0$ the ratio is 4 due to the different anisotropies. In the opposite case $u_\nu \to \infty$ ($\lambda \to \infty$) the ratio converges to 2. A purely magnetoelastic 180° domain wall can therefore energetically be decomposed into two 90° domain walls. Away from the domain wall easy axes this result will not hold any more. The strains of the 180° domain wall are only located at the domain wall and therefore its energy is proportional to the size of the wall. In the 90° case we have incompatibilities and compensating strains whose energy is proportional to the domain size, as already discussed in the previous chapter. If, as usual, the domains are much larger than the domain wall, the energy contribution to compensate incompatibilities will lead to larger energies of the 90° domain wall. In the limits we still have $\lim_{u_\nu\to 0} W_{180}/W_{90} = 4$ but in the other direction $\lim_{u_\nu\to\infty} W_{180}/W_{90} = 0$ because the compensating strains are proportional to the magnetoelastic coupling strength.

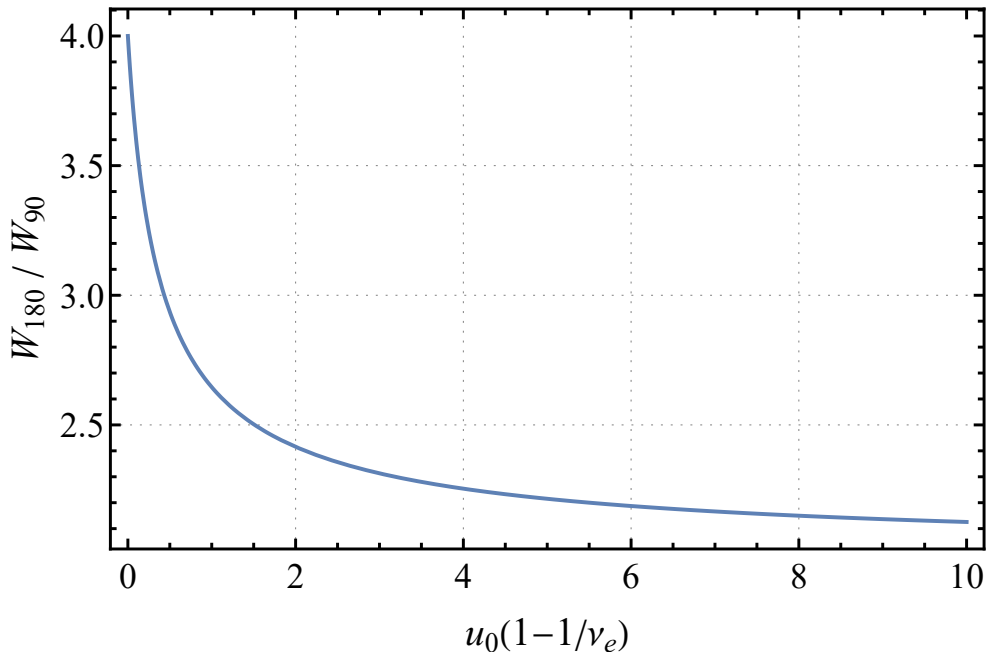

Figure 3.2.: Ratio of the energies per unit area of a magnetoelastic 180° domain wall over a magnetoelastic 90° domain wall. The ratio starts at 4 with zero magnetoelastic coupling and converges to 2 at infinity. The plotted function is written in eq. 3.17.

At this point we found the orientations of the domain walls with minimal energies and further computed these energies, but have no information about the domain wall profile. Therefore, in the next chapter we will study the influence of the magnetoelastic coupling on the profile of the respective domain walls and determine how the size of the domain walls change.

4. Domain Wall Thickness

When the spontaneous strains are fixed, they act as an additional uniaxial anisotropy for the Néel vector along the axis corresponding to the spontaneous strain. We therefore expect the domain wall profile to change and the domain wall to become "thinner" when the magnetoelastic coupling strength and thus the magnitude of the strains increases. In the following this effect will be studied quantitatively. First we look on the change of the domain wall profile for systems with only spontaneous strains. Then we do the same with the full strain distribution, which were determined in sections 3.1 and 3.2, when the domain wall is aligned along an easy direction.

4.1. Spontaneous Strain Profile

4.1.1. 180° Domain Wall with Uniaxial Anisotropy

We start with the investigation of the domain wall shape for the 180° domain wall. We use the anisotropy function $\mathscr{f}_{180}$ which provides uniaxial anisotopy along the x-axis. The axis of the domain wall normal again will be called ξ and lies in the in the xy-plane. In this subsection ξ can be chosen arbitrarily but will be specified in the following ones. Let us fist consider the case without magnetoelastic coupling $\lambda = 0$. The angle ϕ corresponding to minimal energy can then be obtained from equation 2.10 and is given by

$$A\partial_\xi^2\phi = \frac{1}{2}K_2 \sin(2\phi). \tag{4.1}$$

The boundary conditions for a 180° domain wall in the system can be written as $\phi(\xi \to -\infty) = 0$, $\phi(\xi \to \infty) = \pi$ and $\partial_\xi\phi(\xi \to \pm\infty) = 0$. These conditions allow us to write the the first integral of eq. 4.1

$$\frac{1}{2}A(\partial_\xi\phi)^2 = \frac{1}{2}K_2 \sin^2\phi. \tag{4.2}$$

For a domain wall from $\phi = 0$ to $\phi = \pi$, as we increase ξ, the derivative of ϕ is always positive. Thus, we take the positive square root of eq. 4.2 and solve it for a domain wall centered at $\xi = 0$ without loss of generality. The solution for ϕ then is

$$\phi = 2\,\mathrm{arccot}\left(\exp\left[-\sqrt{\frac{K_2}{A}}\xi\right]\right) \tag{4.3}$$

The solution yields a characteristic length scale for the two domain system which describes how broad the domain wall is. We therefore call it the domain wall width $x_{\mathrm{DW}} := \sqrt{A/K_2}$. In terms of the Néel vector the solution is

$$\begin{aligned} n_x &= \cos\left(2\,\mathrm{arccot}\left(\exp\left[-\frac{\xi}{x_{\mathrm{DW}}}\right]\right)\right) = -\tanh\left(\frac{\xi}{x_{\mathrm{DW}}}\right) \\ n_y &= \sqrt{1-\tanh^2\left(\frac{\xi}{x_{\mathrm{DW}}}\right)} = \mathrm{sech}\left(\frac{\xi}{x_{\mathrm{DW}}}\right) \end{aligned} \tag{4.4}$$

When the magnetoealstic coupling is turned on again ($\lambda \neq 0$) we receive an additional term in the equation for ϕ. The two domains in the system are $\mathbf{n} = \mathbf{e}_x$ and $\mathbf{n} = -\mathbf{e}_x$ so we apply the spontaneous strain $u_{xx} - u_{yy} = -\lambda/\mu$ and all other components of the strain tensor are set to 0. Further we define the dimensionless magnetoelastic coupling $u_0 := \lambda^2/(\mu K_2)$ to receive the equation for ϕ from equation 2.10

$$\begin{aligned} x_{\mathrm{DW}}^2 \partial_\xi^2 \phi &= \frac{1}{2}\sin(2\phi) + 2u_0 \sin(2\phi) \\ &= \left(\frac{1}{2} + 2u_0\right)\sin(2\phi). \end{aligned} \tag{4.5}$$

Again we can compute the first integral of the differential equation. As a boundary condition we require that ϕ does not change any more for large values of $|\xi|$ as in the case without coupling. The result then is

$$\frac{1}{2}x_{\mathrm{DW}}^2(\partial_\xi\phi)^2 = \frac{1}{2}\left(1+4u_0\right)\sin^2\phi. \tag{4.6}$$

This differential equation can be solved similar as for the zero coupling case (cf. eq. 4.3 and 4.4) and the solution is visualized in Fig. 4.1. The result for the antiferromagnetic order parameter then is

$$\begin{aligned} n_x &= -\tanh\left(\frac{\xi}{x_{\mathrm{DW}}}(1+4u_0)\right) \\ n_y &= \mathrm{sech}\left(\frac{\xi}{x_{\mathrm{DW}}}\sqrt{1+4u_0}\right). \end{aligned} \tag{4.7}$$

The shape of the domain wall in this case does not change but the domain wall becomes thinner and eventually approaches a step like function if the

magnetoelastic coupling is much larger than the anisotropy. Quantitatively we can describe this by a rescaled domain wall width

$$x_{\mathrm{DW}}^{\lambda} = \frac{x_{\mathrm{DW}}}{\sqrt{1+4u_0}} = \sqrt{\frac{A}{K_2 + 4\lambda^2/\mu}}. \tag{4.8}$$

A plot of the domain wall width against u_0 is shown in Fig. 4.1. This result fits to our prediction of decreasing domain wall. Eq. 4.8 demonstrates how the magnetoelastic coupling acts as an effective anisotropy because it appears with the anisotropy in the denominator. Without calculations we can predict that this phenomenon will also appear in the case of a 90° domain wall with spontaneous strain and it will be quantified in the next section.

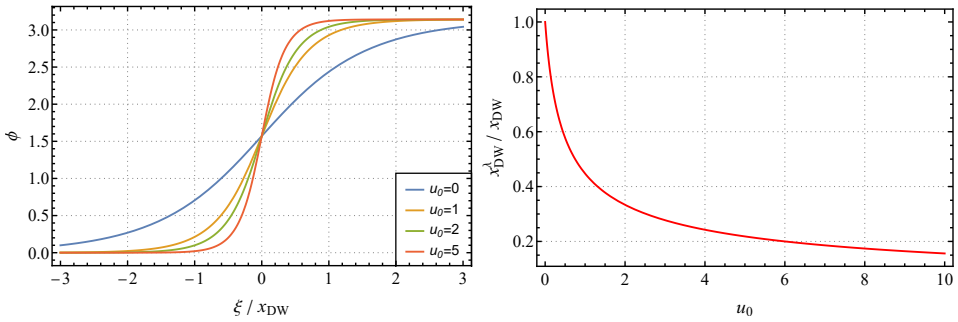

Figure 4.1.: (Left) Solutions from eq. 4.6 to describe the orientation of the Néel vector given by the angle ϕ against the axis ξ normal to the domain wall. (Right) Domain wall width against the dimensionless magnetoelastic coupling parameter u_0 for a 180° domain wall with spontaneous strains.

4.1.2. 90° Domain Wall with In-Plane Anisotropy

We repeat the procedure of the previous section for a 90° domain wall in presence of spontaneous strains. The qualitative behaviour should be the same as for the 180° case but some numerical factors may change. To stabilize the domain wall we use the anisotropy function $\not{f}_{90}$. In the case of zero coupling the differential equation for ϕ is obtained from eq. 2.10 and reads as

$$A\partial_\xi^2\phi = \frac{1}{4}K_2 \sin(4\phi). \tag{4.9}$$

The boundary conditions for the 90° domain wall are $\phi(\xi \to -\infty) = 0$, $\phi(\xi \to \infty) = \pi/2$ and $\partial_\xi\phi(\xi \to \pm\infty) = 0$ from which we obtain the first integral of eq. 4.9

$$\frac{1}{2}A(\partial_\xi\phi)^2 = \frac{1}{8}K_2\sin^2(2\phi). \tag{4.10}$$

The choice of the boundary conditions for ϕ again allow us to take the positive square root. The differential equation can then be solved similar as in the previous section and we find

$$\phi = \operatorname{arccot}\left(\exp\left[-\sqrt{\frac{K_2}{A}}\xi\right]\right) \tag{4.11}$$

with the same characteristic length scale $x_{\mathrm{DW}} = \sqrt{A/K_2}$ as before. Both 90° and 180° domain wall scale similar in the anisotropy and exchange constant. The solution for the Néel vector components then takes the form

$$\begin{aligned} n_x &= \frac{1}{\sqrt{1+\exp\left[-2\xi/x_{\mathrm{DW}}\right]}} \\ n_y &= \frac{\exp\left[-\xi/x_{\mathrm{DW}}\right]}{\sqrt{1+\exp\left[-2\xi/x_{\mathrm{DW}}\right]}}. \end{aligned} \tag{4.12}$$

In the case with nonzero magnetoelastic coupling we do expect a change of the scaling behaviour compared to the 180° wall. In this situation we align the domain wall along an easy direction where the spontaneous strains are compatible. The applied spontaneous strain obeys $u_{xx} - u_{yy} = \lambda/\mu\Theta(\xi/x_{\mathrm{el}})$ with the same step function Θ as in section 3.2. The other components of the strain tensor are 0. As before ϕ can then be determined over eq. 2.10 which becomes

$$x_{\mathrm{DW}}^2\partial_\xi^2\phi = \frac{1}{4}\sin(4\phi) - 2u_0\sin(2\phi)\Theta(\xi). \tag{4.13}$$

Note that if the axis ξ is not an easy axis of the domain wall, we still have the same equation but the value u_0 receives an additional contribution to compensate the incompatibility of spontaneous strains. Together with the boundary conditions we find the first integral of eq. 4.13

$$\frac{1}{2}x_{\mathrm{DW}}^2(\partial_\xi\phi)^2 = \frac{1}{8}\sin^2(2\phi) - u_0\left(1-\Theta(\xi)\cos(2\phi)\right) \tag{4.14}$$

This is possible despite of the explicit dependence of ξ in equation 4.13. The domain wall is centered at $\xi = 0$ due to the spontaneous strain i.e. $\phi(\xi = 0) = \pi/4$ and $\cos(2\phi(\xi = 0))$, then the lefthandside of eq. 4.14 is continuous and the derivative with respect to ξ will lead to eq. 4.13. To solve equation 4.14

we use a numerical approach. The domain wall width is set to 1 so that all length are given in units of the domain wall width and the value u_0 is varied. The solutions for some given values of u_0 are shown in Fig. 4.2 which show the expected behaviour. To further find the scaling of the domain wall width with respect to u_0 we calculate the values $\phi_0^{\pm} := \phi(\pm x_{\mathrm{DW}})$ for the solution where λ is 0. Then we solve $\phi_0^{\pm} = \phi(x^{\pm})$ for $x^{\pm}$ the present coupling and have the new domain wall width $x_{\mathrm{DW}}^{\lambda} = (x^{+} - x^{-})/2$. The error of $x_{\mathrm{DW}}^{\lambda}$ is given by the step size in the of the integration algorithm to solve eq. 4.14. Therefore, we have $\Delta x_{\mathrm{DW}}^{\lambda} = 0.005 x_{\mathrm{DW}}$. After repeating this for enough different coupling strengths we can perform a fit on the data to get the general scaling behaviour. For the fit we use the model $x_{\mathrm{DW}}/\sqrt{1+\alpha u_0}$ which is optimized with respect to α. The ansatz for the fit model was chosen similar to the formula in the 180° case in sec. 4.1.1 but due to the different anisotropy and strain function the factor 4 in eq. 4.8 may be different. From he fit we receive the parameter $\alpha = 5.60\pm$. The data for the domain wall width against the coupling u_0 together with the fit are shown in Fig. 4.2. With this result the domain wall width with magnetoelastic coupling can be written as

$$x_{\mathrm{DW}}^{\lambda} = \frac{x_{\mathrm{DW}}}{\sqrt{1+5.60u_0}} = \sqrt{\frac{A}{K_2 + 5.60\lambda^2/\mu}}. \tag{4.15}$$

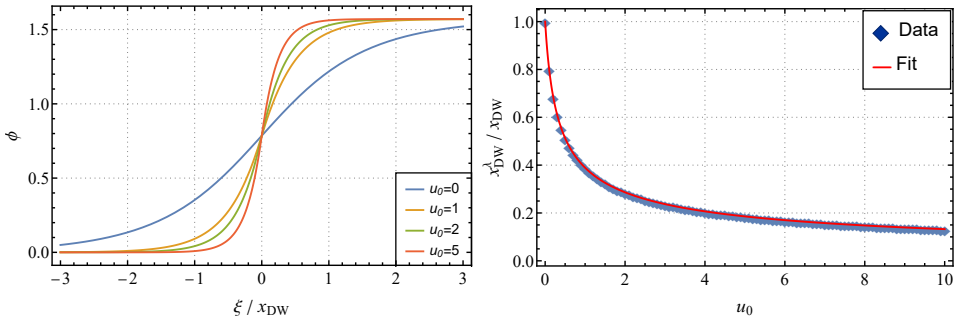

Figure 4.2.: (Left) Solutions from eq. 4.14 to describe the orientation of the Néel vector given by the angle ϕ against the axis ξ normal to the domain wall. (Right) Data and Fit of the domain wall width against the dimensionless magnetoelastic coupling parameter u_0 for a 90° domain wall with spontaneous strains. The Fitmodel is $x_{\mathrm{DW}}/\sqrt{1+\alpha u_0}$ with $\alpha = 5.60\pm$. The errors are to small to show.

As expected the behaviour of the domain wall is similar to the 180° case. The only difference is that the 90° wall decreases "faster" that the 180° wall. The situation may change if we consider the influence of the relative strains because they also depend on the explicit domain wall profile. We still expect

a decrease in the domain wall width with increasing coupling but the explicit scaling may be different. This phenomenon will be studied in the following two sections.

4.2. Full Strain Profile

4.2.1. 180° Domain Wall with Uniaxial Anisotropy

In the previous chapter we have seen that there are some additional strains at the domain wall aside from the spontaneous strains. We include these strains now into the system and attempt to calculate the domain wall width again. We begin with the 180° domain wall which we align along one of its easy axes. We can use eq. 3.7 with the angle $\psi = \pi/4$ to receive the equation

$$x_{\mathrm{DW}}^2(\partial_\xi \phi)^2 = \sin^2\phi + u_0\left(1 - \frac{1}{\nu_e}\right)\sin^2(2\phi). \tag{4.16}$$

We solve the equation similar to the one in sec. 4.1.2 with $u_0(1 - 1/\nu_e)$ as the scanning parameter. The resulting domain wall width plotted against the coupling strength together with the fit is shown in Fig. 4.3. There we see that the fitmodel, which we use for the other cases, does not work for the data of the full strain profile and that the domain wall width scales differently. This is not surprising if we look at the solutions of eq. 4.16. For large values of the magnetoelastic coupling the domain wall has a decreasing slope at the center as if there are two 90° domain walls close to each other. This decrease prevents the domain wall to be a single step function at $u_0 \to \infty$ and the width cannot scale to 0. We therefore have to adapt the fit model to $\beta x_{DW}/\sqrt{1 + \alpha u_0(1 - 1/\nu_e)} + \gamma x_{\mathrm{DW}}$ for the parameters α, β and γ. This fit is also shown in Fig. 4.3 and the fitting parameters are in Tab. 4.1. There we can extract the final result for the domain wall width of a 180° domain wall with uniaxial anisotropy and magnetoelastic coupling

$$\frac{x_{\mathrm{DW}}^{\lambda}}{x_{\mathrm{DW}}} = \frac{0.815}{\sqrt{1 + 0.902u_0\left(1 - \frac{1}{\nu_e}\right)}} + 0.171.$$

	α	β	γ
Fit 1	0.547 ± 0.008	1	0
Fit 2	0.902 ± 0.011	0.815 ± 0.002	0.171 ± 0.002

Table 4.1.: Fitting parameters of the fits in Fig. 4.3. The used model was $\beta/\sqrt{1 + \alpha u_0} + \gamma$ with fixed values $\beta = 1$, $\gamma = 0$ in Fit 1.

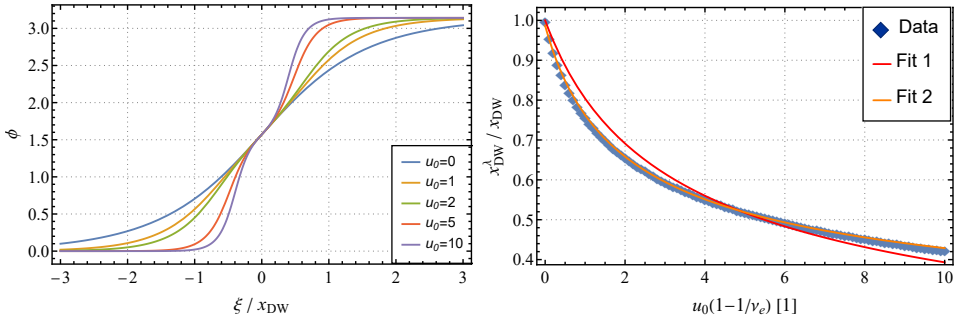

Figure 4.3.: (Left) Solutions from eq. 4.16 with $1/\nu_e = 0.5$ to describe the orientation of the Néel vector given by the angle ϕ against the axis ξ normal to the domain wall. (Right) Domain wall width against the dimensionless magnetoelastic coupling parameter u_0 for a 180° domain wall with spontaneous and internal strains. The fitmodel is $\beta x_{DW}/\sqrt{1+\alpha u_0(1-1/\nu_e)}+\gamma x_{\mathrm{DW}}$ with the parameters in Tab. 4.1. The errors are to small to be shown.

4.2.2. 90° Domain Wall with In-Plane Anisotropy

At last we consider the additional strains on top of spontaneous strains for a 90° domain wall. The domain wall is aligned along one of its easy axis so we can apply eq. 3.15 to our problem to get

$$x_{\mathrm{DW}}^2(\partial_\xi\phi)^2 = \frac{1}{4}\sin^2(2\phi) + u_0\left(1-\frac{1}{\nu_e}\right)\sin^2(2\phi) = \frac{1}{4}\left(1+4u_0\left(1-\frac{1}{\nu_e}\right)\right)\sin^2(2\phi). \tag{4.17}$$

This equation is rather simple and can be solved directly similar to the case without magnetoelastic coupling (cf. sec. 4.1.2). In terms of Néel vector the solution reads as

$$\begin{aligned} n_x &= \frac{1}{\sqrt{1+\exp\left[-2\xi/x_{\mathrm{DW}}\sqrt{1+4u_0\left(1-\frac{1}{\nu_e}\right)}\right]}} \\ n_y &= \frac{\exp\left[-\xi/x_{\mathrm{DW}}\sqrt{1+4u_0\left(1-\frac{1}{\nu_e}\right)}\right]}{\sqrt{1+\exp\left[-2\xi/x_{\mathrm{DW}}\sqrt{1+4u_0\left(1-\frac{1}{\nu_e}\right)}\right]}}. \end{aligned} \tag{4.18}$$

where scaling of the domain wall can be read out of the solution. It is plotted in Fig. 4.4 and has the form

$$x_{\mathrm{DW}}^{\lambda} = \frac{x_{\mathrm{DW}}}{\sqrt{1 + 4u_0\left(1 - \frac{1}{\nu_e}\right)}} = \sqrt{\frac{A}{K_2 + 4\frac{\lambda^2}{\mu}\left(1 - \frac{1}{\nu_e}\right)}}.$$

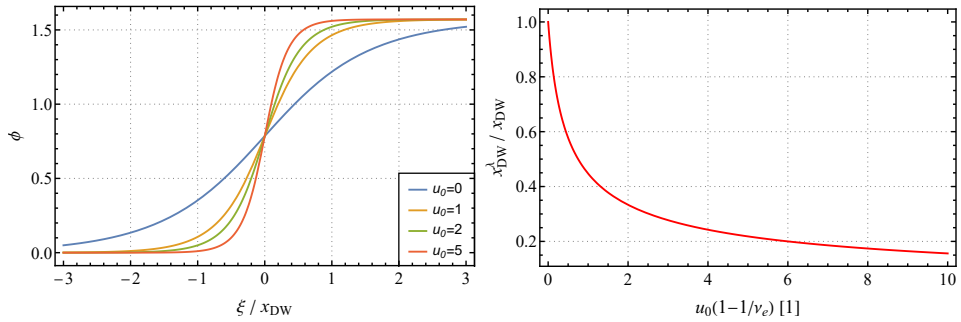

Figure 4.4.: (Left) Solutions from eq. 4.17 for $1/\nu_e = 0.5$ to describe the orientation of the Néel vector given by the angle ϕ against the axis ξ normal to the domain wall. (Right) Domain wall width against the dimensionless magnetoelastic coupling parameter u_0 for a 90° domain wall with spontaneous and internal strains.

Up to now we have studied the energy and shape of infinite flat domain walls with magnetoelastic coupling. The next step is to investigate domain walls, when they are not flat any more. The domain wall anisotropy prevents nonflat domain walls, which are still open and infinite, when we have magnetoelastic interactions. Therefore, we do not consider open domain walls in the next chapter but study the effects of the magnetoelastic coupling on a closed domain wall loop.

5. Closed Domain Wall Loop for 180° Domain Wall

Infinite domain walls in presence of the magnetoelastic interaction will be most likely flat, due to the domain wall anisotropy. If the domain wall is closed, it cannot be flat everywhere anymore for obvious reasons. Still, we expect that the domain wall anisotropy plays a role for the closed domain wall loop and influences it shape. In the following we investigate how the shape of a closed domain wall loop is changing with the magnetoelastic coupling. We are now restricted to the case of a 180° domain wall, but aside from numerical factors the results should be similar in the 90° case.

5.1. Mathematical Description of the Domain Wall Loop

Based on ideas of [61, 62] we describe the domain wall by a curve $\boldsymbol{\gamma}$ in the xy-plane

$$\boldsymbol{\gamma} : [a, b] \to \mathbb{R}^2 \times \{0\}$$

with $\boldsymbol{\gamma}(a) = \boldsymbol{\gamma}(b)$ for $a, b \in \mathbb{R}$, $a < b$. The values a and b stay unspecified for now so we can chose them later to fit to a respective parametrization. In the following the variable of the curve is s and we therefore always have $s \in [a, b]$. The curve has a tangential vector $\mathbf{T}(s) := \boldsymbol{\gamma}'(s)/|\boldsymbol{\gamma}'(s)|$ and a normal vector $\mathbf{N}(s) := (\mathbf{e}_z \times \boldsymbol{\gamma}'(s))/|\boldsymbol{\gamma}'(s)|$. We can write the signed curvature of $\boldsymbol{\gamma}$ as $\kappa(s) = \mathbf{e}_z \cdot (\boldsymbol{\gamma}'(s) \times \boldsymbol{\gamma}''(s))/|\boldsymbol{\gamma}'(s)|^3$. The region around the domain wall loop is parametrized by

$$\boldsymbol{\Gamma}(s, t) = \boldsymbol{\gamma}(s) + t\mathbf{N}(s)$$

with the constraint $|\kappa(s)t| \ll 1$ for the variable t. The metric tensor of this parametrization is $\hat{g}_{\boldsymbol{\Gamma}}(s, t) = \mathrm{diag}(|\boldsymbol{\gamma}'(s)|^2(1-\kappa(s)t)^2, 1)$. The magnetic profile is described by the angle ϕ as in the previous chapters and we approximate

$$\begin{aligned}\cos\phi &= -\tanh(t/x_{\mathrm{DW}}^{\lambda}) \\ \sin\phi &= \pm\sqrt{1-\tanh^2(t/x_{\mathrm{DW}}^{\lambda})} = \pm\,\mathrm{sech}(t/x_{\mathrm{DW}}^{\lambda})\end{aligned}$$

for a 180° domain wall at $t = 0$ with the domain wall width $x^{\lambda}_{\mathrm{DW}}$ from section 4.2. Although the domain wall width was only determined for a domain wall along an easy axis, we assume a similar scaling of the width when the domain wall loop goes along a different axis. In this approximation the energy density $\mathcal{W}$ becomes a function of s and t and the energy reads as

$$W = \int \mathcal{W}(s,t)\sqrt{\det(\hat{g}_{\mathbf{\Gamma}}(s,t))}dsdt = \int \mathcal{W}(s,t)|\boldsymbol{\gamma}'(s)|(1-\kappa(s)t)dsdt. \quad (5.1)$$

Integration over t yields an energy functional $W[\boldsymbol{\gamma}(s)]$ which we can then minimize with respect to the curve parametrization.

5.2. Effective Energy Density

In order to integrate the righthandside of equation 5.1 over t we have to first determine the integration interval $[t^-, t^+]$ which depends on the curve parameter s. The boundaries for t have to be chosen such that $|\kappa(s)t| \ll 1$ but we also need the whole domain wall to be covered in the integral range. For converging terms we can therefore apply the limits $t^{\pm} \to \pm\infty$ as an approximation. In the rest of this section the boundaries will not be explicitly written at the integral sign. The result from the integration of the energy density can be interpreted as an effective energy density along the curve.
To perform the integration we split the energy density in its different parts and start with the exchange term. For this we have

$$\mathcal{W}_{\mathrm{exch}} = \frac{1}{2}A(\nabla\phi)^2 = \frac{1}{2}A(\nabla \arccos(-\tanh(\frac{t}{x^{\lambda}_{\mathrm{DW}}})))^2 = \frac{A}{2x^{\lambda}_{\mathrm{DW}}}\operatorname{sech}^2(\frac{t}{x^{\lambda}_{\mathrm{DW}}}). \quad (5.2)$$

sech^2 is an even function in t and therefore we have $\int w_{\mathrm{exch}}tdt = 0$. The effective energy for the exchange part can then be computed

$$\begin{aligned}\mathcal{W}^{\mathrm{eff}}_{\mathrm{exch}} &= \frac{A}{2x^{\lambda}_{\mathrm{DW}}}|\boldsymbol{\gamma}'(s)| \int \operatorname{sech}^2\left(\frac{t}{x^{\lambda}_{\mathrm{DW}}}\right)dt \\ &= \frac{A}{2x^{\lambda}_{\mathrm{DW}}}|\boldsymbol{\gamma}'(s)| \left[\tanh(\frac{t}{x^{\lambda}_{\mathrm{DW}}})\right]^{\infty}_{-\infty} \\ &= \frac{A}{x^{\lambda}_{\mathrm{DW}}}|\boldsymbol{\gamma}'(s)|.\end{aligned} \quad (5.3)$$

The next term in the energy density is the anisotropy. We choose the anisotropy function $\mathscr{f}_{180}$ for the 180° domain wall loop. The energy density then has the form

$$\mathcal{W}_{\text{anis}} = \frac{1}{2}K_2 - \frac{1}{2}K_2\cos^2\phi = \frac{1}{2}K_2 - \frac{1}{2}K_2\tanh^2(\frac{t}{x^\lambda_{\text{DW}}}) = \frac{1}{2}K_2\,\text{sech}^2(\frac{t}{x^\lambda_{\text{DW}}}), \tag{5.4}$$

where we added a constant for the integral to converge. The integration works similar to the exchange energy and the result is

$$\begin{aligned}\mathcal{W}^{\text{eff}}_{\text{anis}} &= \frac{1}{2}K_2|\boldsymbol{\gamma}'(s)|\int \text{sech}^2\left(\frac{t}{x^\lambda_{\text{DW}}}\right)dt \\ &= K_2 x^\lambda_{\text{DW}}|\boldsymbol{\gamma}'(s)|.\end{aligned} \tag{5.5}$$

The last contribution to the energy is the minimized magnetoelastic (and elastic) term. On a small local frame the domain wall loop can be viewed as flat thus we approximate the energy term by the solution from sec. 3.1. It has the form

$$\begin{aligned}\mathcal{W}_{\text{me}} =& \frac{\Lambda}{2}\left[\cos(2(\phi+\psi)) - \cos(2\psi)\right]^2 \\ =& 2\Lambda\left[\sin^4\phi\cos^2(2\psi) + \sin^2\phi\cos^2\phi\sin^2(2\psi) + 2\sin^3\phi\cos\phi\sin(2\psi)\cos(2\psi)\right] \\ =& 2\Lambda\left[\text{sech}^4\left(\frac{t}{x^\lambda_{\text{DW}}}\right)\cos^2(2\psi) + \text{sech}^2\left(\frac{t}{x^\lambda_{\text{DW}}}\right)\tanh^2\left(\frac{t}{x^\lambda_{\text{DW}}}\right)\sin^2(2\psi)\right. \\ &\left. + 2\,\text{sech}^3\left(\frac{t}{x^\lambda_{\text{DW}}}\right)\tanh\left(\frac{t}{x^\lambda_{\text{DW}}}\right)\sin(2\psi)\cos(2\psi)\right],\end{aligned} \tag{5.6}$$

where we define $\Lambda := \lambda^2(1 - 1/\nu_e)/\mu$. The angle ψ again is given by the angle between the domain wall normal and the x-axis. The terms with sech^4 and $\text{sech}^2\tanh^2$ are even functions and the one with $\text{sech}^3\tanh$ is odd in the variable t. The nonvanishing integrals (over t) in the energy functional from equation 5.1 therefore are

$$\begin{aligned}\int \text{sech}^4\left(\frac{t}{x^\lambda_{\text{DW}}}\right)dt &= \frac{4}{3}x^\lambda_{\text{DW}} \\ \int \text{sech}^2\left(\frac{t}{x^\lambda_{\text{DW}}}\right)\tanh^2\left(\frac{v}{x^\lambda_{\text{DW}}}\right)dt &= \frac{2}{3}x^\lambda_{\text{DW}} \\ \int v\,\text{sech}^3\left(\frac{t}{x^\lambda_{\text{DW}}}\right)\tanh\left(\frac{t}{x^\lambda_{\text{DW}}}\right)dt &= \frac{2}{3}(x^\lambda_{\text{DW}})^2.\end{aligned}$$

The explicit calculations of the integrals are similar to the previous two terms and are therefore not shown. With these integrals we can determine the effective energy density for the magnetoelasic term.

$$\begin{aligned}\mathcal{W}_{\text{me}}^{\text{eff}} &= \frac{4\Lambda}{3} x_{\text{DW}}^{\lambda} \left[2\cos^2(2\psi) + \sin^2(2\psi) - 2\kappa(s) x_{\text{DW}}^{\lambda} \sin(2\psi)\cos(2\psi)\right] \\ &= \frac{4\Lambda}{3} x_{\text{DW}}^{\lambda} \left[\cos^4\psi + \sin^4\psi - 2\kappa(s) x_{\text{DW}}^{\lambda} \left(\cos^3\psi \sin\psi - \sin^3\psi \cos\psi\right)\right]\end{aligned} \tag{5.7}$$

By definition of the angle ψ as the angle between the domain wall normal and the x-axis, we can write $\cos\psi = \gamma_y'(s)/|\boldsymbol{\gamma}'(s)|$ and $\sin\psi = \gamma_x'(s)/|\boldsymbol{\gamma}'(s)|$. This connection is illustrated in Fig. 5.1. Together with the effective energy densities, this allows us to rewrite the energy from eq. 5.1 as a functional of the curve $\boldsymbol{\gamma}$

$$\begin{aligned}W[\boldsymbol{\gamma}(s)] = \int \Bigg[&\left(\frac{A}{x_{\text{DW}}^{\lambda}} + K_2 x_{\text{DW}}^{\lambda}\right) |\boldsymbol{\gamma}'(s)| + \frac{4\Lambda}{3} x_{\text{DW}}^{\lambda} \frac{\gamma_x'^4(s) + \gamma_y'^4(s)}{|\boldsymbol{\gamma}'(s)|^3} \\ &+ \frac{8\Lambda}{3} (x_{\text{DW}}^{\lambda})^2 \frac{(\gamma_x'(s)\gamma_y''(s) - \gamma_y'(s)\gamma_x''(s))(\gamma_x'^3(s)\gamma_y'(s) - \gamma_y'^3(s)\gamma_x'(s))}{|\boldsymbol{\gamma}'(s)|^6} \Bigg] ds.\end{aligned} \tag{5.8}$$

5.3. Equilibrium Shape of the Closed Domain Wall Loop with Fixed Curve Length

A domain wall in a magnetic system costs energy due to the exchange and anisotropy terms in the energy density. The energy W will therefore be minimized if $\boldsymbol{\gamma}$ collapses to a single point (i.e. $\boldsymbol{\gamma}' \equiv 0$). To omit this effect we impose that the length of the curve is fixed to a value $L \gg x_{DW}^{\lambda}$. Then each possible shape of the domain wall loop has the same exchange and anisotropy contributions and the shape corresponding to minimal energy is purely determined by the magnetoelastic coupling. To find the equilibrium states of the closed domain wall loop we have to minimize the energy functional $W[\boldsymbol{\gamma}(s)]$ with respect to the function $\boldsymbol{\gamma}$. To do this we look at each term in equation 5.8 individually.
The first term is proportional to $|\boldsymbol{\gamma}(s)|$ inside the integral. The integration gives

$$\int |\boldsymbol{\gamma}(s)| ds = L$$

independent of the shape of the curve and the first term of equation 5.2 will be just a constant contribution to the energy. Physically, this term corresponds to exchange and anisotropy and therefore was expected to be a constant (i.e.

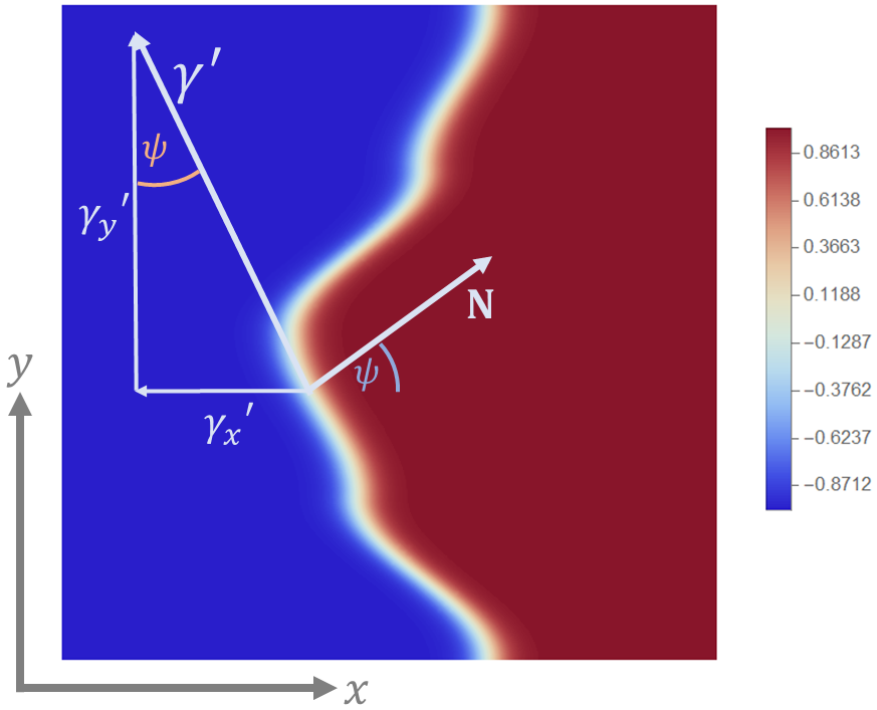

Figure 5.1.: Visualization of a domain wall string to show the connection between the derivative γ' of the curve and the domain wall angle ψ. The colors indicate the value of the x-component of the Néel vector $\mathbf{n}$. The curve γ itself runs along the domain wall i.e. the white space between the red and blue domains.

independent of the domain wall shape) in the desired system.
The second term of equation 5.8 only includes the first derivative $\boldsymbol{\gamma}'$ of $\boldsymbol{\gamma}$. Therefore this term will be minimal for a curve that has a parametrization with constant $\boldsymbol{\gamma}'$. We consider $\boldsymbol{\gamma}$ to be parametrized in arc length ($|\boldsymbol{\gamma}'(s)| = 1$) and find the minimum of the term for $\gamma_x' \equiv \pm\sqrt{2}/2$ and $\gamma_y' \equiv \pm\sqrt{2}/2$. To make a closed loop out of this result we can define $\boldsymbol{\gamma}$ piecewise over the derivative

$$\boldsymbol{\gamma}'(s) = \begin{cases} (\sqrt{2}/2, \sqrt{2}/2, 0) & s \in [a, s_1) \\ (-\sqrt{2}/2, \sqrt{2}/2, 0) & s \in [s_1, s_2) \\ (-\sqrt{2}/2, -\sqrt{2}/2, 0) & s \in [s_2, s_3) \\ (\sqrt{2}/2, -\sqrt{2}/2, 0) & s \in [s_3, b] \end{cases} \tag{5.9}$$

for $a < s_1 < s_2 < s_3 < b$, $l_1 := s_1 - a = s_3 - s_2$ and $l_2 := s_2 - s_1 = b - s_3$. This parametrization corresponds to a rectangle with axes running along the easy domain wall axes, that already were determined in section 3.1.

To be consistent the last term of equation 5.8 will also be treated for a parametrization in arc length. In this case we write $\gamma_y'(s) = \pm\sqrt{1-\gamma_x'^2(s)}$ the two terms in the bracket read as

$$\begin{aligned}\gamma_x'(u)\gamma_y''(s) - \gamma_y'(s)\gamma_x''(s) &= -\frac{\gamma_x''(s)}{\sqrt{1-\gamma_x'^2(s)}}\\ \gamma_x'^3(s)\gamma_y'(s) - \gamma_y'^3(s)\gamma_x'(s) &= \gamma_x'(s)\sqrt{1-\gamma_x'^2(s)}\left(2\gamma_x'^2(s)-1\right)\end{aligned}$$

and the full third term in the energy density then becomes

$$\begin{aligned}&-\int \gamma_x'(s)\gamma_x''(s)\left(2\gamma_x'^2(s)-1\right)du\\ =&-\int \gamma_x'(s)\left(2\gamma_x'^2(s)-1\right)d\left(\gamma_x'(s)\right)\\ =&-\frac{1}{2}\left[\gamma_x'^2(s)\left(\gamma_x'^2(s)-1\right)\right]_{s=a}^{s=b},\end{aligned}$$

for a curve parametrization in C^1 (i.e. no δ-functions in the first or second derivative). This term ends up to be 0, because it should be independent of the starting point such that we have $\boldsymbol{\gamma}'(a)^2 = \boldsymbol{\gamma}'(b)^2$. The curve from equation 5.9 has a parametrization in C^1 with

$$\begin{aligned}\gamma_x'(s) &= -l_i\ \mathrm{sign}\left(\cos\left(\frac{\pi s}{2l_i}\right)\right)\sin\left(\frac{\pi s}{l_i}\right)\\ \gamma_y'(s) &= l_i\ \mathrm{sign}\left(\sin\left(\frac{\pi s}{2l_i}\right)\right)\sin\left(\frac{\pi s}{l_i}\right)\end{aligned}$$

with $i = 1$ if $s \in [a, s_1] \cup [s_2, s_3]$ and $i = 2$ otherwise. Therefore this curve also gives 0 in the third term and does not add more energy compared to other curves in this term.

In total, the curve parametrized by equation 5.9 minimizes the energy from equation 5.8 but there are some constraints. To be consistent with the approximation $t^{\pm} \to \pm\infty$ in the integration we require $l_1, l_2 \gg x_{\mathrm{DW}}^{\lambda}$ i.e. the facing domain walls are not allowed to be to close to each other. Also the curve needs to fulfill the conditions for its curvature that were imposed before i.e. $|t^{\pm}(s)\kappa(s)| \ll 1$. At the edges of the curve from equation 5.9 the curvature diverges with the consequence $t^{\pm} \to 0$ on each edge. That again contradicts the assumption $t^{\pm} \to \pm\infty$ in the integration over t. This can be treated by formally restricting the curvature to $|\kappa(s)| \leq 1/nx_{\mathrm{DW}}^{\lambda}$ for a sufficiently large n to keep the assumption but still with $L \gg nx_{\mathrm{DW}}^{\lambda}$. The curve will still attempt to go along its easy axes as long as possible and therefore achieve its

maximal allowed curvature close the edges. In other words the sharp edges are replaced by quarter circles with curvature $1/nx_{\mathrm{DW}}^{\lambda}$. The change of length of the complete curve is negligible due to $L \gg nx_{\mathrm{DW}}^{\lambda}$ so we do not contradict the length conservation by the replacement of the edges on length scales of L. Thus, on such length scales a rectangle as in eq. 5.9 describes the shape of a closed domain wall loop, when its length is fixed.

5.4. Equilibrium Shape of the Closed Domain Wall Loop with Fixed Area

Another possibility to prevent the collapse of the curve to one point is fixing the area, that is enclosed in the curve. This will show how the competition between magnetoelastic coupling against anisotropy and exchange acts out in the loop. Therefore in this section the area is fixed to a value $V \gg (x_{\mathrm{DW}}^{\lambda})^2$ and the length of the curve is allowed to vary. As the first term of the energy in equation 5.8 is proportional to the curve length, it will be minimized for a curve with the shortest length for a given area. Thus, we find the minimum of the first term for a circle with radius $r := \sqrt{V/\pi}$. The second term of the energy will still be minimal for $\boldsymbol{\gamma}' \propto (\pm 1, \pm 1)$ on a local level but also is attempting to minimize its area. We therefore will receive a square shape at the minimum of this term. The third term of the energy expression gives no contribution into the energy for closed loops as before. The equilibrium shape of the domain wall loop is therefore determined by the first two terms and has the form of something in between a circle and a square depending on the strength of the magnetoelastic coupling. We can approximate such shapes by a superellipse [63] i.e. by a shape with $|\gamma_x/a|^n + |\gamma_y/b|^n = 1$. For $a = b$ the superellipse can be parametized with

$$\begin{aligned} \gamma_x^{\mathrm{se}}(s) &= a\ \mathrm{sign}(\cos(s))\ |\cos(s)|^{2/n} \\ \gamma_y^{\mathrm{se}}(s) &= a\ \mathrm{sign}(\sin(s))\ |\sin(s)|^{2/n} \end{aligned} \tag{5.10}$$

for $s \in [0, 2\pi]$ and $n \geq 2$ in our case. For $n \to \infty$ the curve will be a square with the sides parallel to the x- and y-axis. To make the approximation feasible, we have to additionally rotate the superellipse by 45° and use the parametrization

$$\begin{aligned} \gamma_x(s) &= (\gamma_x^{\mathrm{se}}(s) + \gamma_y^{\mathrm{se}}(s))/\sqrt{2} \\ \gamma_y(s) &= (\gamma_x^{\mathrm{se}}(s) - \gamma_y^{\mathrm{se}}(s))/\sqrt{2} \end{aligned} \tag{5.11}$$

Each quarter of the superellipse contributes equally to the energy, so we restrict s to the interval $[0, \pi/2]$. On this interval the sine and cosine are both positive and the parametrization simplifies to its final form

$$\begin{aligned}\gamma_x(s) &= a(\cos^{2/n}(s) + \sin^{2/n}(s))/\sqrt{2} \\ \gamma_y(s) &= a(\cos^{2/n}(s) - \sin^{2/n}(s))/\sqrt{2}\end{aligned} \tag{5.12}$$

The integral in W cannot be solved analytically for all n, so we attempt a numerical approach. The area of a superellipse is $V = \sqrt{\pi}4^{1-1/n}a^2\Gamma(1 + 1/n)/\Gamma(1/2 + 1/n)$ [64] where Γ marks the Gamma function [65]. Conserving this area gives a relation between the free parameters of our parametrization namely

$$a = \frac{2^{-1+1/n}\sqrt{V\Gamma(1/2 + 1/n)}}{\pi^{1/4}\sqrt{\Gamma(1 + 1/n)}}. \tag{5.13}$$

For fixed values A, K_2 and Λ we perform the integrals for multiple values of n numerically and determine which value minimizes the energy of the closed domain wall loop. We set $x_{\mathrm{DW}} = 1$ and $V = 1$ and repeat the calculations for different values of the ratio $\Lambda/K_2(= u_\nu)$. The error is dominated the step size in n compared to the error of the numerical integration. We therefore set the error for the n of minimal energy to $\Delta n = 0.01$. The values n which correspond to minimal energy for different values of the magnetoelastic coupling are shown in Fig. 5.2. There we see the expected behaviour, zero coupling corresponds to $n = 2$ and the curve has the shape of a circle. For infinite coupling n diverges and the curve approaches a square. To predict n (and a) for values Λ/K_2 beyond 10 the data was fitted. The used fit model is $\alpha \exp(\beta(\Lambda/K_2)) + \gamma(\Lambda/K_2) + \delta$ with the parameters listed in Tab. 5.1. For applications it would be more convenient to always approximate the shape not by a super ellipse but by the square shape which we have at $\Lambda \to \infty$. To see when this is possible we compare the ratio of the energies of a square and the energy of the superellipse for the same value of Λ/K_2. The ratio is visualized in Fig. 5.3. The superellipse shape has 95% of the square energy at the value of $\Lambda/K_2 = 0.845 \pm 0.001$ and 99% of the square energy at $\Lambda/K_2 = 3.75 \pm 0.01$. Depending on the accuracy goal we can therefore approximate the shape of a closed domain wall loop with fixed area by a square with sides along the domain wall easy axes for values below 4 (or even 1) of the ratio of magnetoelastic coupling to anisotropy.

α	β	γ	δ
0.477 ± 0.012	0.392 ± 0.002	1.53 ± 0.01	1.57 ± 0.01

Table 5.1.: Fitting parameters of the fit in Fig. 5.2 with the model $\alpha \exp(\beta(\Lambda/K_2)) + \gamma(\Lambda/K_2) + \delta$.

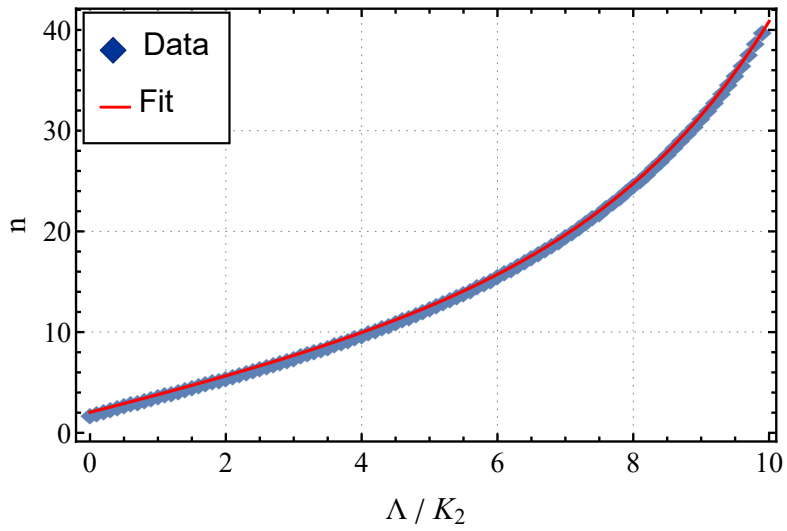

Figure 5.2.: Data and fit of the parameter n of the superellipse corresponding to minimal energy with respect to the magnetoelastic coupling. The used fitmodel is $\alpha \exp(\beta(\Lambda/K_2)) + \gamma(\Lambda/K_2) + \delta$ with the parameters from Tab. 5.1 The error bars to the data are too small to be represented in the data.

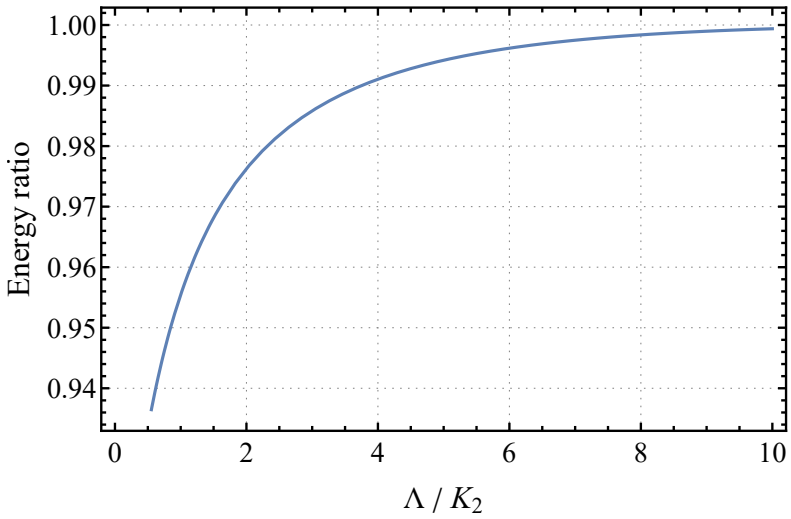

Figure 5.3.: Energy ratio of a closed domain wall loop with shape of a square (sides along domain wall easy axes) over a superellipse as in eq. 5.12. The parameters n and a correspond to their respective energy minima for a given value Λ/K_2. They can be determined over the fit in Tab. 5.1 and eq. 5.13

This concludes the study of static domain walls in this work. We know about the energy and shape of flat domain walls and how a closed domain wall loop is shaped under magnetoelastic interactions. In the next step we want to investigate dynamical effects of magnetoelastic domain walls. We take a step back to flat domain walls and determine how they react to disturbances.

6. Pinning of a 90° Domain Wall with Frozen Spontaneous Strains

In order to study dynamical phenomena on magnetoelastic domain walls, we consider a model in which the acoustic modes of the lattice have significantly lower frequencies than the AFM magnetic modes. Thus, on the time scales of the AFM we can assume that the lattice and therefore strains are "frozen" i.e. do not depend on time. This assumption is reasonable because the acoustic modes in crystals often are in the GHz regime (cf. e.g. [66–68]), which is significantly lower than the THz AFM dynamics. In such a situation the spontaneous strains corresponding to a 90° domain wall (cf. eq. 3.11) act as an effective inhomogeneous uniaxial anisotropy. A shift of the domain wall or a change in its profile therefore increases the energy due to the effective anisotropy. This effect is visualized in Fig. 6.1. Thus, the domain wall prefers to stay at the position corresponding to the initialized spontaneous strains. This gives rise to the idea that 90° domain walls can be pinned by their spontaneous strains. In the following sections we demonstrate this pinning and further determine its strength.

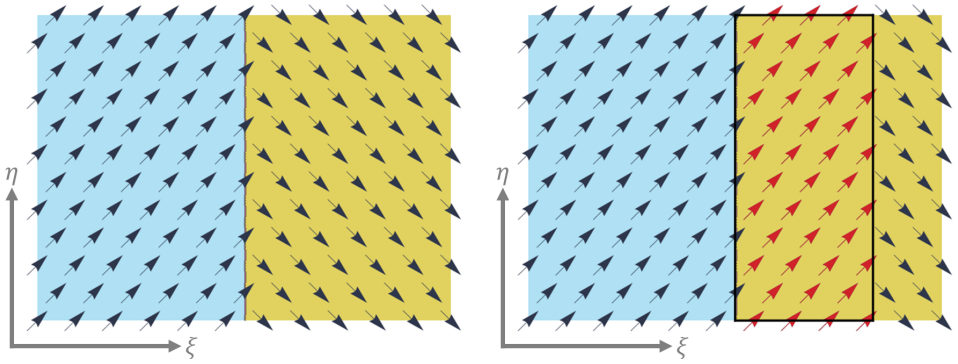

Figure 6.1.: Visualization of shifting a domain wall with frozen strains. The background color indicates the spontaneous strain profile, while different color corresponds to opposite sign. The arrows indicate the orientation of the Néel vector. On the left the equilibrium of a 90° domain wall normal to the axis ξ is shown. On the right the domain wall is shifted. Thus, in the marked rectangle the strains do not minimize the energy of the corresponding magnetic profile..

6.1. Localized Modes of Excitations of the Domain Wall

6.1.1. Derivation of the Eigenvalue Equation of a Domain Wall Excitation

To describe the dynamics of our magnetoelastic system we have to consider the AFM Lagrangian density

$$\mathcal{L} = \frac{1}{2}\tilde{\tau}^2 \left[\dot{\mathbf{n}} + \mathbf{n} \times \mathbf{h}\right]^2 - \mathcal{W}, \tag{6.1}$$

[69] for $\tilde{\tau} \in \mathbb{R}$, where $\mathcal{W}$ is the energy density consisting of exchange, anisotropy and magnetoelastic contributions (cf. chapter 2) and $\mathbf{h}$ is the applied external field. In the field free case the kinetic term reduces to $\dot{\mathbf{n}}^2 = \dot{\phi}^2$ and the equation of motion is found by the Euler Lagrange equation. With the anisotropy function $\mathscr{f}_{90}$ we receive

$$\tau^2 \ddot{\phi} = x_{\mathrm{DW}}^2 \nabla^2 \phi - \frac{1}{4}\sin(4\phi) - 2\frac{\lambda}{K_2}\left(-(u_{xx} - u_{yy})\sin(2\phi) + 2u_{xy}\cos(2\phi)\right). \tag{6.2}$$

for $\tau := \tilde{\tau}/\sqrt{K_2}$. We impose the frozen strain profile corresponding to a 90° domain wall and set $u_{xx} - u_{yy} = u_0 \mu K_2/\lambda \Theta(\xi)$ and $u_{xy} = 0$ such that u_0 describes the dimensionless strength of the magnetoelastic coupling. Θ acts as a sign function (cf. chapter 3) and ξ is a space variable corresponding to an axis in the xy-plane. ϕ will then only vary along the ξ-axis and the derivative ∇^2 can be replaced by ∂_ξ^2. In the static case the solution for ϕ will describe a 90° domain wall as we have seen in Fig. 4.2. Let ϕ_0 be that static solution of eq. 6.2 and ϕ_1 a small deviation ($|\phi_1| \ll |\phi_0|$) such that $\phi_0 + \phi_1$ still solves eq. 6.2. Let us further assume that ϕ_1 is harmonic in time i.e. $\phi_1(\xi, t) = \varphi(\xi)\exp(i\omega t)$. In this case we can expand eq. 6.2 in φ about ϕ_0 up to first order to receive a linear equation for φ

$$\tau^2\omega^2\varphi = -x_{\mathrm{DW}}^2 \partial_\xi^2 \varphi + \left[\cos(4\phi_0) + 4u_0\Theta(\xi)\cos(2\phi_0)\right]\varphi. \tag{6.3}$$

We do not have a zero order term in the upper equation because it corresponds to the static eq. 6.2 with the field ϕ_0 and is therefore 0 on both sides. Due to the domain wall shape (cf. 4.2) we approximate $\cos(2\phi_0) = -\tanh(\xi/x_{\mathrm{DW}}^\lambda)$ where x_{DW}^λ is taken from sec. 4.1.2. Together with the new variable $\mathcal{X} := \xi/x_{\mathrm{DW}}$ eq. 6.3 changes to

$$\tau^2\omega^2\varphi = -\partial_{\mathcal{X}}^2\varphi + \left[1 - 2\,\mathrm{sech}\,(\alpha_\lambda \mathcal{X}) - 4u_0\Theta(\xi)\tanh(\alpha_\lambda \mathcal{X})\right]\varphi. \tag{6.4}$$

with $\alpha_\lambda := x_{\mathrm{DW}}/x^{\lambda}_{\mathrm{DW}} = \sqrt{1+5.60u_0}$. The term in the square brackets will be referred to as the potential V_{90} and is shown in Fig. 6.2 for some values of u_0. We further define $\mathcal{H}_{90} := \partial^2_{\mathcal{X}} + V_{90}$. The potential is symmetric with a minimum at 0 and no maxima. It converges to $1+4u_0$ at $\mathcal{X} \to \pm\infty$. Thus, eq. 6.4 has free solutions (if we interpret eq. 6.4 as a Schrödinger equation) for $\tau^2\omega^2 > 1+4u$. If there are also bound solutions (solutions with $\tau^2\omega^2 < 1+4u_0$) with nonzero eigenvalue we can conclude that the domain wall is pinned. In this case a small excitation (e.g. a shift) of the domain wall does not provide freely propagating magnons but an oscillation on top of the equilibrium solution ϕ_0 localized at the domain wall center and the domain wall stays at the inhomogeneity of the strain distribution. Thus, to prove that domain walls can be pinned by strains, we attempt to find bound states of $\mathcal{H}_{90}$ with nonzero eigenvalues. Before we begin with this, let us consider the case $u_0 = 0$. In this situation eq. 6.4 is known [70] and has one bound state $\varphi \propto \mathrm{sech}(\mathcal{X})$ with $\tau^2\omega^2 = 0$. We therefore expect to also find one bound state for nonzero u_0 and that the eigenvalue as a function $\tau^2\omega^2(u_0)$ converges to 0 for $u_0 \to 0$.

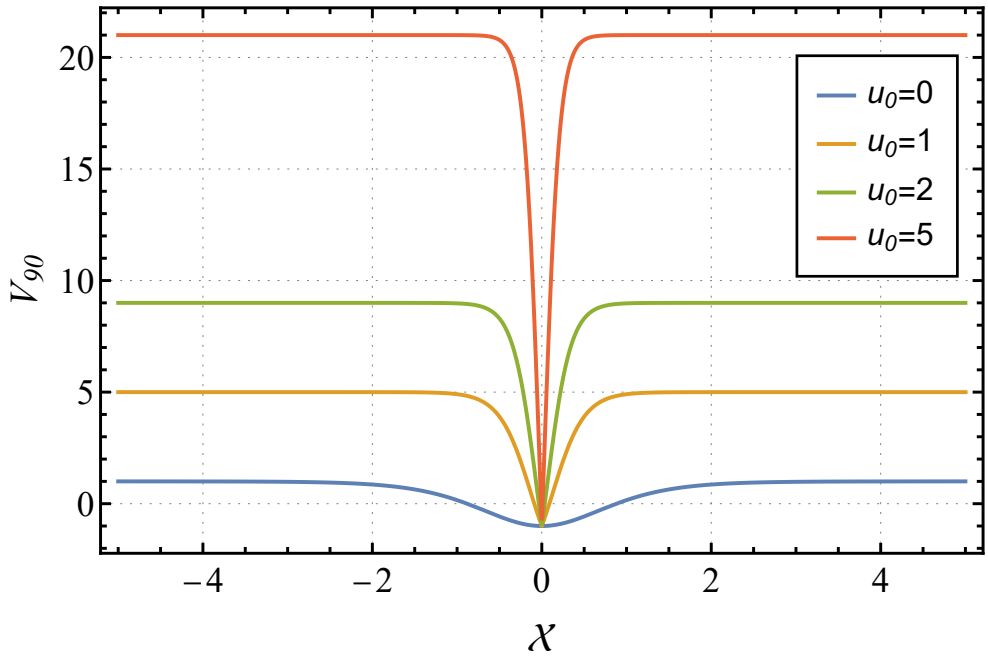

Figure 6.2.: Potential $V_{90}(\mathcal{X})$ for different values of u_0.

6.1.2. Ground State Eigenvalue with the WKB Approximation

Eq. 6.4 is similar to the Schrödinger equation in one dimension [71]. This allows us to apply methods that are usually used in quantum mechanics to find

the energy eigenvalues. We receive a first guess of the ground state eigenvalue below $1+4u_0$ by applying the WKB approximation [72]. In this approximation, the eigenvalues E_n for a Hamiltonian with potential $V(\mathcal{X})$ can be obtained by the relation

$$\int_{x_{\text{turn}}^-}^{x_{\text{turn}}^+} d\mathcal{X}\sqrt{E_n - V(\mathcal{X})} = \pi\left(n+\frac{1}{2}\right) \tag{6.5}$$

where $V(x_{\text{turn}}^{\pm}) = E_n$. $x_{\text{turn}}^- < x_{\text{turn}}^+$ are the turning points of the potential and $n \in \mathbb{N}_0$ enumerates the discrete eigenvalues such that $E_n < E_{n+1}$ for all possible n. In the case of $V \equiv V_{90}$ the turning points for the ground state $E_0 = \tau^2\omega^2$ if $\tau^2\omega^2 < 1 + 4u_0$ are

$$x_{\text{turn}}^{\pm} = \pm\frac{1}{2\alpha_\lambda}\ln\left[\frac{1+\tau^2\omega^2+2\sqrt{\tau^2\omega^2+4u_0^2}}{1-\tau^2\omega^2+4u_0}\right].$$

The ground state energy can then be determined by solving eq. 6.5 for $\tau^2\omega^2$. We do this numerically by scanning through different values $\tau^2\omega^2$ in a range between 0 and $1 + 4u_0$. If the integral of eq. 6.5 corresponds to 0 within the error for one value of $\tau^2\omega^2$ we take this value as the ground state energy which then is a bound state. The step size of the scan gives the error of the estimate for $\tau^2\omega^2$, in our case we have $\Delta\tau^2\omega^2 = 0.01$. The results of that procedure are shown in Fig. 6.3 together with a linear Fit on the data. The parameters of the fit are listed in 6.1. From the parameters we receive a ground state eigenvalue for zero coupling of 0.480 ± 0.009 which significantly differs form the real value 0. This is due to the fact, that the WKB approximation is inaccurate for low eigenvalues and gets better if the value increases because. The reason is that in terms of quantum mechanics a large eigenvalue corresponds to large energy and small de Broglie wave length, which is a requirement for the WKB [72]. Thus, for large u_0 the ratio to the real eigenvalue should shrink as the eigenvalue increases and the approximation is more accurate. We therefore expect a similar i.e. a linear behaviour of the real ground eigenvalue with respect to u_0 in the large u_0 limit. This demonstrates the existence of a bound state in the eigensystem of eq. 6.5 and that the frequency ω scales with $\sqrt{u_0}$. The domain wall is therefore pinned and the strength of the pinning increases with u_0 because of the increasing frequency. The procedure was repeated for the next order eigenvalue $n = 1$ but there were no real turning points in the range $\tau^2\omega^2 \in [0, 1 + 4u_0)$, which implies that the $n = 0$ bound state is the only one. For a more accurate quantitative analysis of the lowest order state we have to move on to other methods which will be applied in the following two sections.

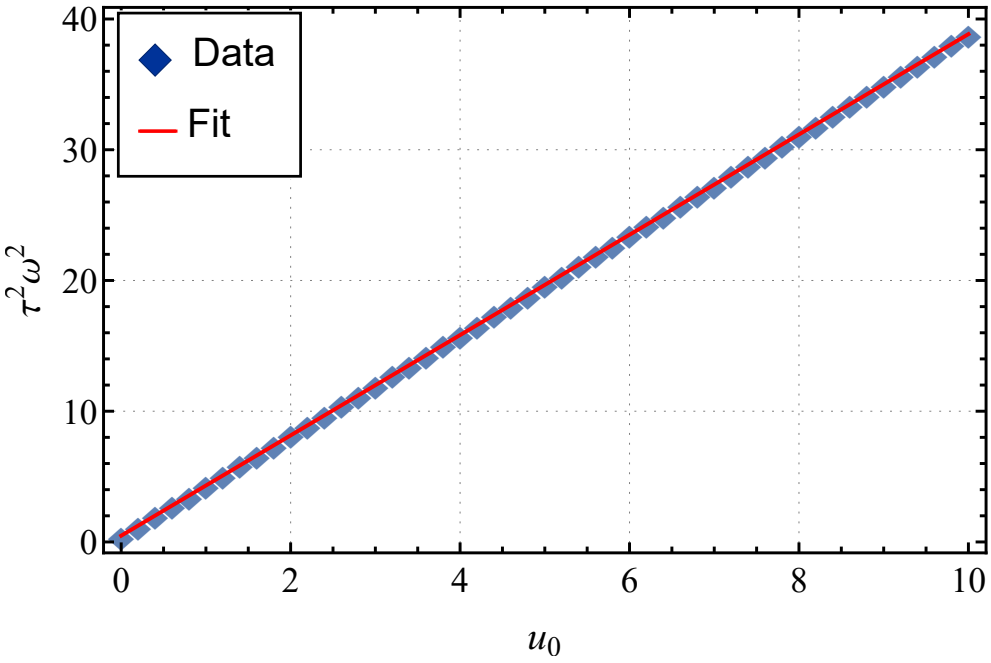

Figure 6.3.: Data and linear fit of the lowest order eigenvalue of eq. 6.4 determined over the WKB approximation. The parameters of the fit are given in Tab. 6.1. The error bars are to small to be shown in the plot.

a	b
3.84 ± 0.01	0.480 ± 0.009

Table 6.1.: Parameters of the fit in Fig. 6.3 to the model $au_0 + b$.

6.1.3. Ground State Eigenvalue with the Variational Principle

For a Schrödinger equation $(-\partial_{\mathcal{X}}^2 + V(\mathcal{X}))\varphi = E\varphi$ with the ground state energy E_0 any normalized wave function φ fulfils the relation

$$\langle\varphi|\left(\partial_{\mathcal{X}}^2 + V(\mathcal{X})\right)|\varphi\rangle := \int_{\mathbb{R}} d\mathcal{X}\varphi^*(\partial_{\mathcal{X}}^2 + V(\mathcal{X}))\varphi \geq E_0 \tag{6.6}$$

[71]. If the exact ground state is not known but we can approximate its wave function, this relation can be used to find an upper bound of the ground state energy close to the real value. In our case we can use this to find the bound state eigenvalue from eq. 6.4 by approximating the wave function with a free parameter. Then we can minimize the integral of eq. 6.7 with respect to the parameter to have the upper bound of the ground state. This procedure is (as the WKB approximation) one of the fundamental approximation methods [71].

Since the ground state for zero coupling is proportional to $\mathrm{sech}(\mathcal{X})$, we use $\varphi_\beta(\mathcal{X}) = \sqrt{\beta/2}\,\mathrm{sech}(\beta\mathcal{X})$ as an approximation for the real ground state. Then, for given u_0, we scan through different values of $\beta > 1$ and determine which value minimizes $\langle\varphi_\beta|\,\mathcal{H}_{90}\,|\varphi_\beta\rangle$. The results for u_0 from 0 to 10 is shown in Fig. 6.4 with a linear fit whose fitting parameters are in Tab. 6.2. The fitfunction is always below $1 + 4u_0$ which shows again the existence of a bound state and the linear behaviour of the data shows the square root scaling between ω and u_0. The results for the eigenvalue are also below the ones from the WKB approximation so the best estimate for the oscillation frequency of the ground state for now is

$$\omega = \frac{\sqrt{0.147 + 3.26u_0}}{\tau} \tag{6.7}$$

with an error estimate of $\sqrt{0.147}/\tau$ at each value of u_0. This is due to the analytical solution from which we know that $u_0 = 0$ has $\omega = 0$.

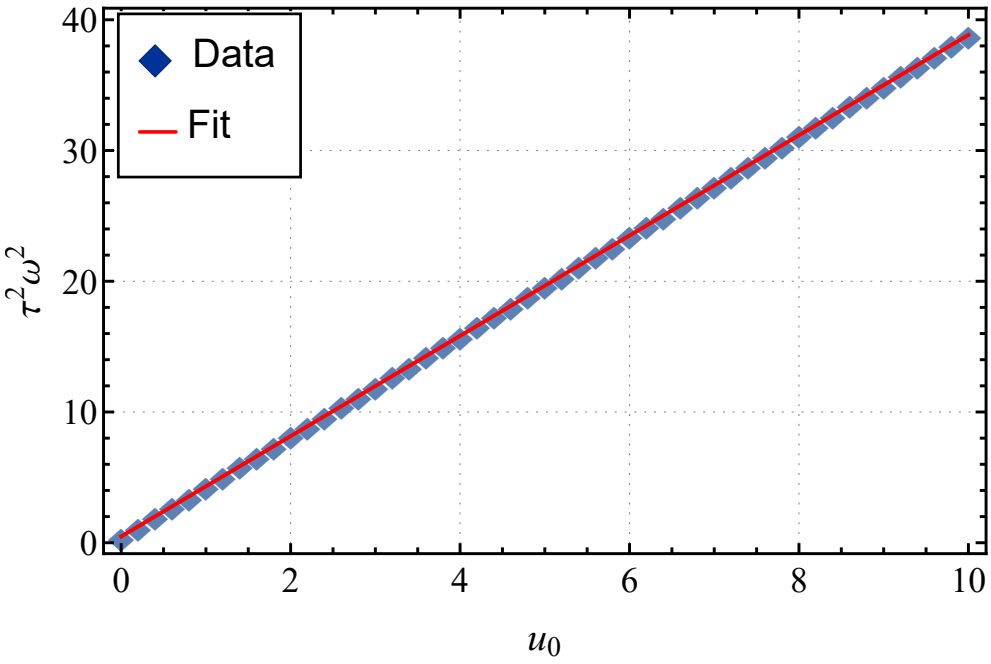

Figure 6.4.: Data and linear fit of the lowest order eigenvalue of eq. 6.4 determined over the variational principle. The parameters of the fit are given in Tab. 6.2. The error bars are to small to be shown in the plot.

Although the approximation $\varphi \sim$ sech makes sense in regarding the solution without coupling, we have no evidence that the approximation is valid. To justify the result a bit more, we repeat the procedure with other test functions

a	b
3.26 ± 0.01	0.147 ± 0.006

Table 6.2.: Parameters of the fit in Fig. 6.4 to the model $au_0 + b$.

φ. Considering the shape of the potential, we know that the ground state wave function is symmetric around $\mathcal{X} = 0$ and decreases continuously from the center. Therefore, the other test functions have a Gaussian and a Lorentzian shape. The results of these functions are presented in the appendix D.1 and provide similar but slightly larger eigenvalues than the hyperbolic approach. Therefore, we keep the relation from eq. 6.7 as our best estimate of the ground state but still do not know how far the ground state energy will be below this estimate. To answer this and to verify the variational method we compute the ground state eigenvalue again, using the software package Mathematica in the next section.

6.1.4. Ground State Eigenvalue with the Software Mathematica

The software Mathematica has an implemented function "NDEigensystem" (since version 10.2) to determine the eigenfunction and -value of a linear operator over a given region. In the context of a Hamilton operator the term region corresponds to infinite potential outside of the input region and the potential of the input Hamiltonian inside. In our real system there is are no borders with infinite potential beyond them. It would therefore be intuitive to choose a region as large as possible. However, this approach will not provide correct results because in the numerical computation each segment along $\mathcal{X}$ is weighted the same. If the potential is approximately constant for a large part of the input region, deviations from that constant in the potential have a small weight compared to the large approximately constant part. Thus, in our case we receive $\tau^2\omega^2 \approx 1 + 4u_0$ for too large ranges, which contradicts the previous results. On the other hand, the region cannot be chosen too small, otherwise the potential in Mathematica and the real potential differ too much and we compute the wrong eigenvalues. In order to find an appropriate range in positive and negative direction, which defines the region, we have to compare the eigenvalues for different ranges. For this, we first look at the solution of the lowest order eigenvalue for a range of 10 $x^{\lambda}_{\mathrm{DW}}$. In that and all following calculations the version 12.2 of Mathematica [73] has been used. The results are shown in Fig. 6.5 together with a fit and the fit parameters are in Tab. 6.3. The linear scaling coincides with the solutions from the previous sections. To quantify the scaling we now compute and fit the eigenvalue for different ranges and compare the parameters a and b of a linear fit of the model $au_0 + b$. These results are visualized in Fig. 6.5. We see a plateau for ranges in between of 10 and 40 $x^{\lambda}_{\mathrm{DW}}$. In this territory, we expect to receive the best estimate for

the lowest order eigenvalue of the real potential V_{90}. We perform a weighted average over all such values and receive receive

$$a = 3.23 \pm 0.01$$
$$b = 0.159 \pm 0.005$$

for $\tau^2\omega^2 = au_0 + b$ is the best estimate of the lowest order eigenvalue for $\mathcal{H}_{90}$ with Mathematica. The value is larger than the one from the variational principle for all $u_0 > 0$. Thus, the variational principle provides the best approximation for the real ground state eigenvalue for $\mathcal{H}_{90}$ because it has the lowest of all determined eigenvalues, which still has to be greater than the real value. All methods have shown that the domain wall is pinned by frozen spontaneous strains and the frequency of the excitation increases with the coupling over $\omega \sim \sqrt{u_0}$. To further quantify the strength of the pinning we will determine the force, that is required to overcome the pinning with respect to u_0 in the following section.

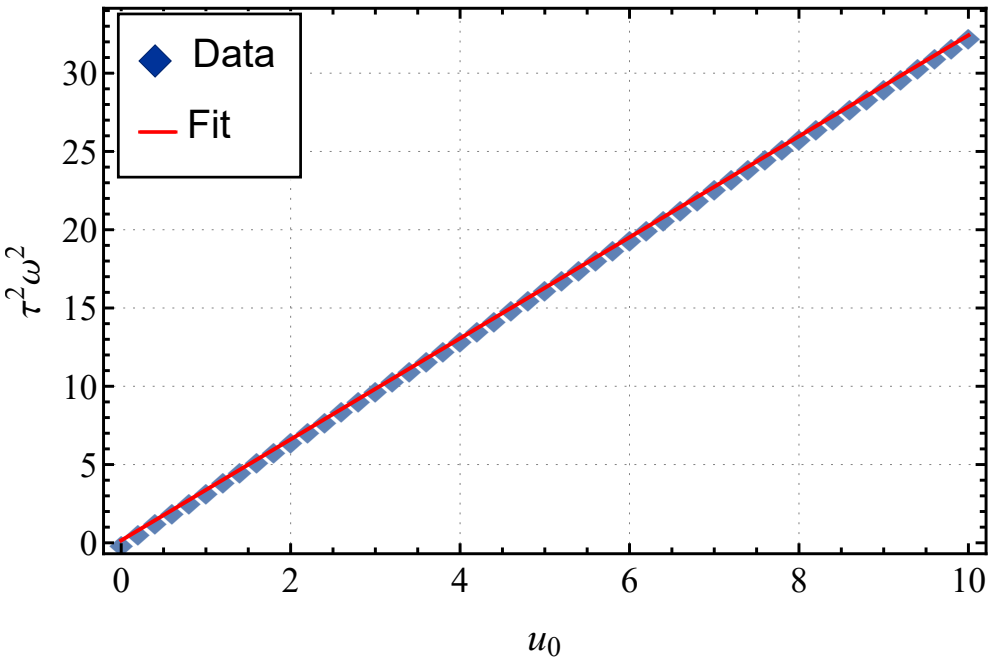

Figure 6.5.: Data and linear fit of the lowest order eigenvalue of $\mathcal{H}_{90}$ computed with Mathematica in a range of 10 $x_{\mathrm{DW}}^{\lambda}$. The fitting parameters are shown in Tab. 6.3.

a	b
3.23 ± 0.01	0.153 ± 0.007

Table 6.3.: Fitting parameters of the fit in Fig. 6.5 for the model $au_0 + b$.

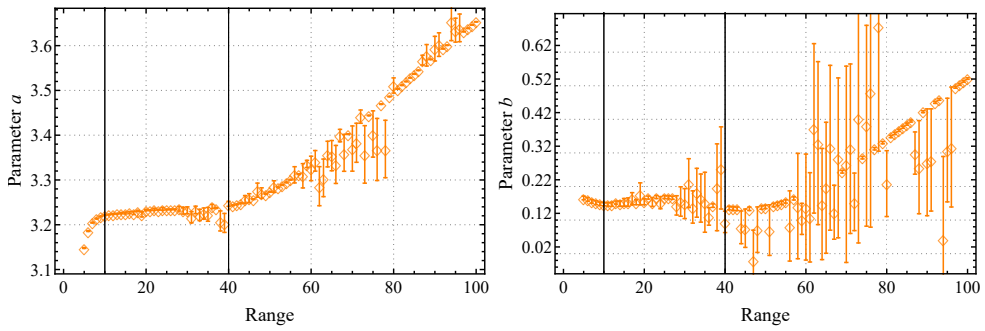

Figure 6.6.: Fitting parameters of the eigenvalues of $\mathcal{H}_{90}$ with respect to u_0. The eigenvalues were determined with Mathematica for different ranges in the input regions and the fit model was $au_0 + b$. The vertical lines mark the borders of the plateau.

6.2. Pinning Force

We have observed that the 90° domain wall is pinned by the spontaneous stains. Now we want to quantify the strength of that pinning. To do this we compute the pinning potential

$$U_{\text{pin}}(X) = \int_{\mathbb{R}} d\mathcal{X}\ \mathcal{W}(\mathcal{X}, \phi(\mathcal{X} - X)) = \int_{\mathbb{R}} d\mathcal{X}\ \mathcal{W}_{\text{me}}(\mathcal{X}, \phi(\mathcal{X} - X)) + k. \quad (6.8)$$

This potential corresponds to the energy that increase by shifting the domain wall by the value X, when the strains are frozen. Since there is only an explicit space dependence in the magnetoelastic term from the spontaneous strain, the other energy contributions will add up to a constant $k \in \mathbb{R}$ in the pinning potential. Thus, for simplicity we shift the potential $U_{\text{pin}}(X) \to U_{\text{pin}}(X) - k$. In the case of a 90° domain wall with spontaneous strains under the approximation $\cos(2\phi) = -\tanh(\alpha_\lambda \mathcal{X})$ the potential has the form

$$U_{\text{pin}}(X) = 4u_0 \int_{\mathbb{R}} d\mathcal{X}(1 - \Theta(\mathcal{X}) \tanh(\alpha_\lambda(\mathcal{X} - X))) = \frac{4u_0 K_2}{\alpha_\lambda} \ln\cosh(2\alpha_\lambda X), \quad (6.9)$$

where a constant $4u_0$ was added to the energy density for the integral to converge. The potential is shown in Fig. 6.7. From the pinning potential we can compute the force per unit area in the domain wall plane, that

acts onto the domain wall after being shifted by X in real space coordinates over $F := -U'_{\mathrm{pin}}(X) = -8u_0K_2\tanh(2\alpha_\lambda X)$ in units of the reciprocal rescaled domain wall width. Alternatively we can describe the shift in real space coordinates $\Xi := x^\lambda_{\mathrm{DW}}X$ to receive the force $F := -dU_{\mathrm{pin}}(\Xi/x^\lambda_{\mathrm{DW}}) = -8u_0K_2\tanh(2\alpha_\lambda X)/x^\lambda_{\mathrm{DW}}$. This force is also plotted in Fig. 6.7. F in monotonous and converges against $\mp 8u_0K_2/x^\lambda_{\mathrm{DW}}$ at $\pm\infty$. This shows, that the domain wall always feels a repulsive force when shifted away from the center which always increases with distance. When we manually want to remove the domain wall from the pinning center we need to apply a force larger or equal to $8u_0K_2/x^\lambda_{\mathrm{DW}}$ in its absolute. Since this value defines how strong the pinning of the domain wall is due to the spontaneous strain we call this the pinning force F_{pin} of our domain wall system. The pinning force increases with the magnetoelastic coupling $F_{\mathrm{pin}} \sim u_0$ so we have to apply stronger forces to overcome the pinning when the strength of coupling increases.
We have shown that 90° domain walls are pinned by spontaneous strains on short time scales, where the strains are approximately frozen. The strength of such pinning scales with the strength of the coupling between the strains and the Néel vector. Although we only considered 90° domain walls, it is reasonable to argue that we observe similar effects for all kinds of domain walls, where the spontaneous strain is different for both domains. This is due to the role of strains as an effective inhomogeneous anisotropy such that the domains have minimal energy when the wall stays at the inhomogeneity of the strain profile. When the spontaneous strain is constant i.e. for 180° domain walls this argument does not hold anymore and a potential pinning needs to have a different origin. We therefore study this case explicitly in the next chapter.

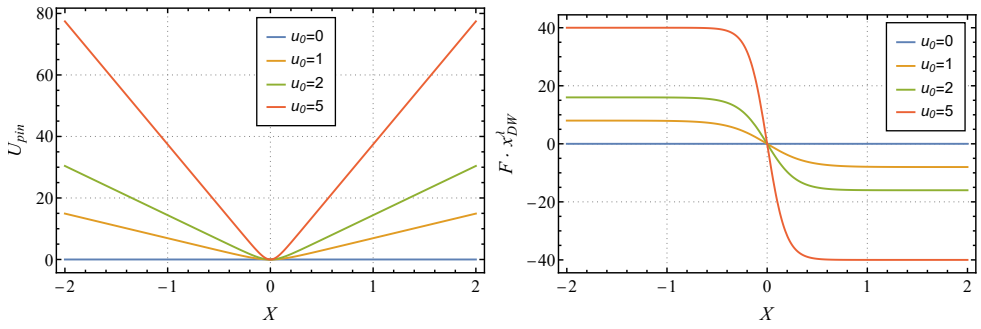

Figure 6.7.: Potential (left) and force (right) which correspond to a shift of a 90° domain wall with frozen spontaneous strains away from equilibrium. The potential is linear for large values of X and the slope increases with the coupling. Thus, the retracting force to the minimum of the potential converges to a constant which increases with the strength of magnetoelastic coupling.

7. Pinning of a 180° Domain Wall with Frozen Relative Strains

In 180° domain walls the spontaneous strain is a constant and cannot pin a domain wall. Nevertheless, a domain wall induces relative strains localized at the domain wall. These strains minimize the energy for a given domain wall and thus a shift or other excitation of the domain wall profile with frozen strains still lead to an increase of the energy. This motivates the idea that 180° magnetoelastic domain walls with frozen relative strains are also pinned as the 90° walls with spontaneous strains. Thus, we study pinning effects for 180° domain walls similar to the previous chapter.

7.1. Localized Modes of Excitations of the Domain Wall

7.1.1. Derivation of the Eigenvalue Equation of a Domain Wall Excitation

To receive the eigenvalue equation for excitations in a 180° domain wall we follow the same steps as for the 90° domain wall. We begin with the Euler Lagrange equation which for the 180° case with the anisotropy function $\not{f}_{180}$ takes the form

$$\tau^2 \ddot{\phi} = x_{\mathrm{DW}}^2 \nabla^2 \phi - \frac{1}{2}\sin(2\phi) - 2\frac{\lambda}{K_2}\left(-(u_{xx} - u_{yy})\sin(2\phi) + 2u_{xy}\cos(2\phi)\right). \tag{7.1}$$

We assume that ϕ_0 is the static solution of eq. 6.2 for a 180° domain wall along its easy axis $\xi := (x+y)/\sqrt{2}$ as in sec. 3.1 with the corresponding strains

$$\begin{aligned} u_{xx} - u_{yy} &= -\frac{u_0 K_2}{\lambda}\cos(2\phi_0) \\ 2u_{xy} &= -\frac{u_0 K_2}{\lambda \nu_e}\sin(2\phi_0) \end{aligned}$$

(cf. eq. 3.3 and 3.6). Again we consider a small deviation ϕ_1 such that $\phi_0 + \phi_1$ solves eq. 7.1 and with $|\phi_1| \ll |\phi_0|$. We assume ϕ_1 only varies along ξ and has the time dependence $\phi_1(\xi, t) = \varphi(\xi)\exp(i\omega t)$. The linearized equation for φ then takes the form

$$\begin{aligned}\tau^2\omega^2\varphi &= -x_{\mathrm{DW}}^2\partial_\xi^2\varphi + \left[\cos(2\phi_0) - 4u_0(u_{xx}-u_{yy})\cos(2\phi_0) - 4u_0(2u_{xy})\sin(2\phi_0)\right]\varphi \\ &= -x_{\mathrm{DW}}^2\partial_\xi^2\varphi + \left[\cos(2\phi_0) + 4u_0\cos^2(2\phi_0) + \frac{4u_0}{\nu_e}\sin^2(2\phi_0)\right]\varphi\end{aligned} \tag{7.2}$$

We approximate $\cos(\phi_0) = -\tanh(\xi/x_{\mathrm{DW}}^\lambda)$ similar to chapter 5 with x_{DW}^λ from sec. 4.2.1. With the definitions $\mathcal{X} := \xi/x_{\mathrm{DW}}$ and $\alpha_\lambda = x_{\mathrm{DW}}/x_{\mathrm{DW}}^\lambda$ we receive the equation

$$\begin{aligned}\tau^2\omega^2\varphi = -\partial_{\mathcal{X}}^2\varphi + \Big[&1 - 2\,\mathrm{sech}^2(\alpha_\lambda\mathcal{X}) + 4u_0(1-2\,\mathrm{sech}(\alpha_\lambda\mathcal{X}))^2 \\ &+\frac{16u_0}{\nu_e}\tanh^2(\alpha_\lambda\mathcal{X})\,\mathrm{sech}^2(\alpha_\lambda\mathcal{X})\Big]\varphi.\end{aligned} \tag{7.3}$$

We call the term in the square brackets the potential V_{180} and define $\mathcal{H}_{180} := -\partial_{\mathcal{X}}^2 + V_{180}$ as we did in the situation of the 90° domain wall. The potential is shown in Fig. 7.1. It has the same properties for $\mathcal{X} \to \infty$ as V_{90} and is equal to V_{90} for $u_0 = 0$, thus it has free states for eigenvalues above $1 + 4u_0$ and can have bound states with eigenvalues below. We attempt to compute the bound states with similar methods as in the previous chapter.

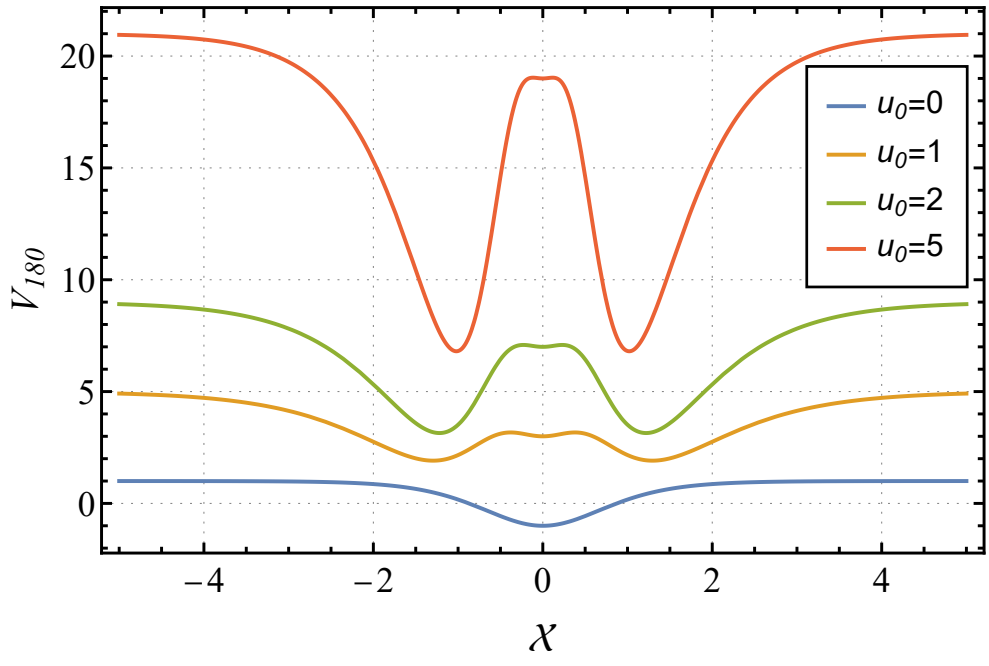

Figure 7.1.: Potential $V_{180}(\mathcal{X})$ for different values of u_0 and $1/\nu_e = 0.5$.

7.1.2. Ground State Eigenvalue with the WKB Approximation

We begin with the WKB approximation to find the number of bound states and to receive a first estimate of the eigenvalue with respect to u_0. Similar to sec. 6.1.2 we compute the lefthandside of eq. 6.5 and solve it for $n = 0$ to receive the ground state by scanning through multiple values for E_0. In some cases there are more than two turning points which have to be computed numerically (Cf. Fig. 7.1). Then, the lefthandside of eq. 6.5 is divided into sums of integrals between neighbouring turning points such that $E_0 > V_{180}(\mathcal{X})$ along all integration intervals. The results for the ground state eigenvalue from these computations for $1/\nu_e = 0.5$ are shown in Fig. 7.2. For sufficiently large u_0 the data approaches a linear function. We perform a linear fit on the data to receive the large u_0 scaling of the ground state eigenvalue of $\mathcal{H}_{180}$, where the WKB approximation is the most accurate [72]. The fit is shown in fig. 7.2 and the fitting parameters are in Tab. 7.1. To generalize the result, we repeat the calculations for different values of ν_e. The eigenvalues with respect to the magenetoelastic coupling as well as their linear fits are shown in the appendix D.2. The fitting parameters a and b are fitted themselves as a function of $1/\nu_e$ to find the corresponding dependency. This is shown in Fig. 7.3 with fitting parameters is Tab. 7.2. We finally obtain the result for the lowest order eigenvalue of eq. 7.3 with the WKB approximation in the regime of large u_0

$$\tau^2\omega^2 = (1.60\sqrt{1 + 4.08/\nu_e} - 1.07)u_0 + 0.337/\nu_e + 1.13. \tag{7.4}$$

Since the eigenvalue is nonzero for $u_0 \neq 0$, we can conclude that the domain wall is pinned by the relative strains of a 180° domain wall. Further we see that the eigenfrequency is smaller than in the 90° case from the previous chapter. Thus, the pinning by relative strains is weaker than by spontaneous strains. The strength of the pinning will be further investigated in sec. 7.2. For the next order eigenvalue $n = 1$ eq. 6.5 has no solutions for $E_1 < 1 + 4u_0$ (and no turning points above). Therefore, as for the 90° domain wall there is only one bound state, for which we can use the variational principle to find an upper limit of the eigenvalue. We use this method in the next section in order to find the scaling in the regime of low u_0 and hence low eigenvalue, where the WKB approximation is inaccurate.

a	b
1.72 ± 0.01	1.30 ± 0.03

Table 7.1.: Parameters of the fit in Fig. 7.2 to the model $au_0 + b$.

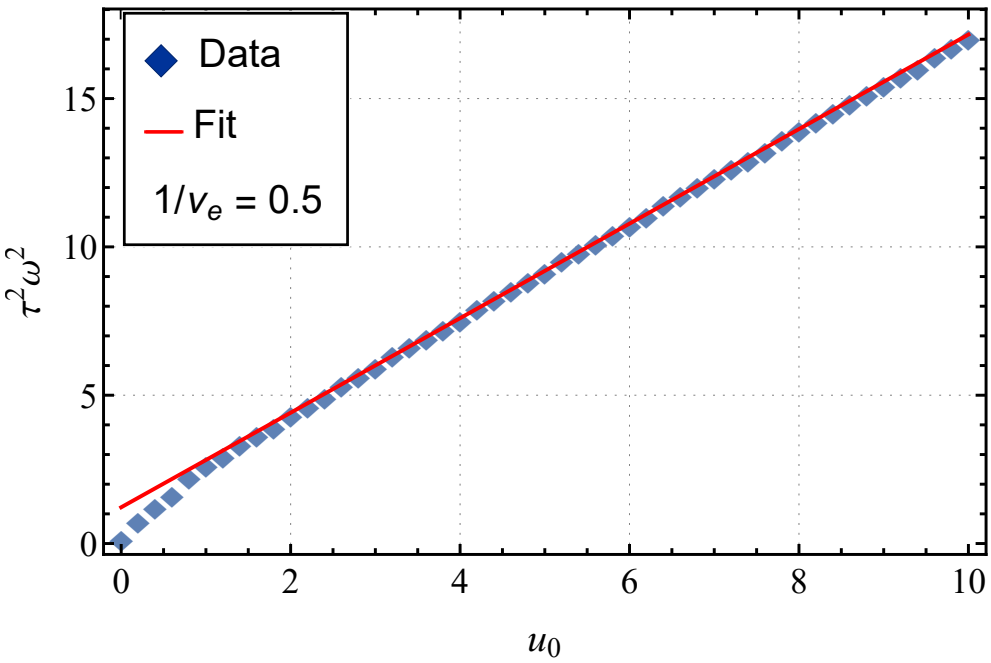

Figure 7.2.: Data and linear fit of the lowest order eigenvalue of eq. 7.3 with $1/\nu_e = 0.5$ determined over the WKB approximation. The parameters of the fit are given in Tab. 7.1. The error bars are to small to be shown in the plot.

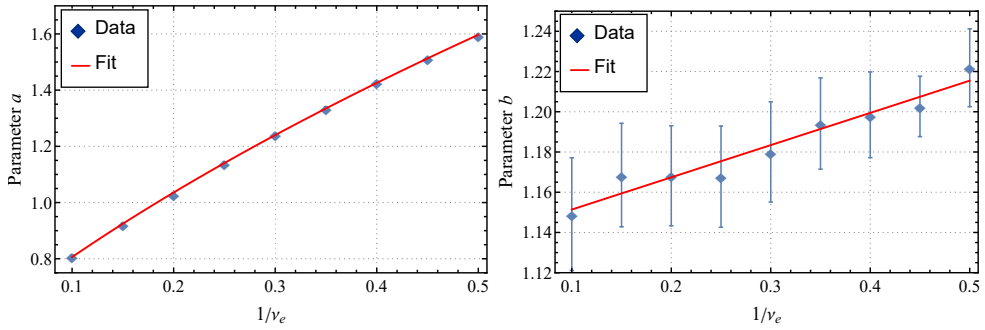

Figure 7.3.: Data and fits of the fitting parameter form the linear fits of Fig. 7.2 and D.2 with respect to $1/\nu_e$. The parameter a (left) is the slope of the fits and the parameter b (right) is the y-intercept. The parameters of the shown fits are in Tab. 7.2.

	α	β	γ
Param. a	1.60 ± 0.08	4.08 ± 0.28	-1.07 ± 0.08
Param. b		0.337 ± 0.026	1.13 ± 0.01

Table 7.2.: Parameters of the fits in Fig. 7.3. The fit model was $\alpha\sqrt{1+\beta/\nu_e}+\gamma$ for the parameter a and $\beta/\nu_e+\gamma$ for the parameter b.

7.1.3. Ground State Eigenvalue with the Variational Principle

We now want to find an estimate for the ground state eigenvalue when u_0 is low and therefore repeat the steps from sec. 6.1.3 for $\mathcal{H}_{180}$ i.e. we compute $\langle\varphi_\beta|\,\mathcal{H}_{180}\,|\varphi_\beta\rangle$ for an approximate φ_β for the ground state and minimize the expression with respect to β. As an approximate for the ground state we choose $\varphi_\beta(\mathcal{X}) = \sqrt{\beta/2}\,\mathrm{sech}(\beta\mathcal{X})$ because for $u_0 = 0$ φ_1 is the exact solution for the ground state. Therefore, the ground state wave function should not differ significantly from the test function as long as u_0 is small enough. When u_0 increases the approximation is not valid anymore, due to the different shape of the potential (Cf. Fig. 7.1). The result of this calculation for $1/\nu_e = 0.5$ is shown in Fig. 7.4 together with a linear fit. The fitting parameters are in Tab. 7.3. To have the solution for arbitrary ν_e we repeat the calculations for different values of ν_e. The fitting parameters of the linear fits for the different ν_e are then fitted as well with respect to $1/\nu_e$. This is shown in Fig. 7.5 with the parameters of the new fits in Tab. 7.4. These results provide an upper bound of the ground state eigenvalue of

$$\tau^2\omega^2 = (5.74\sqrt{1+0.704/\nu_e} - 3.97)u_0 + 0.204/\nu_e + 0.194. \tag{7.5}$$

In the regime of low u_0 this upper bound can also be used as an estimate of the ground state eigenvalue as mentioned above. We again also attempt to determine the eigenvalues over Mathematica to quantify again the scaling f the eigenvalues for large u_0.

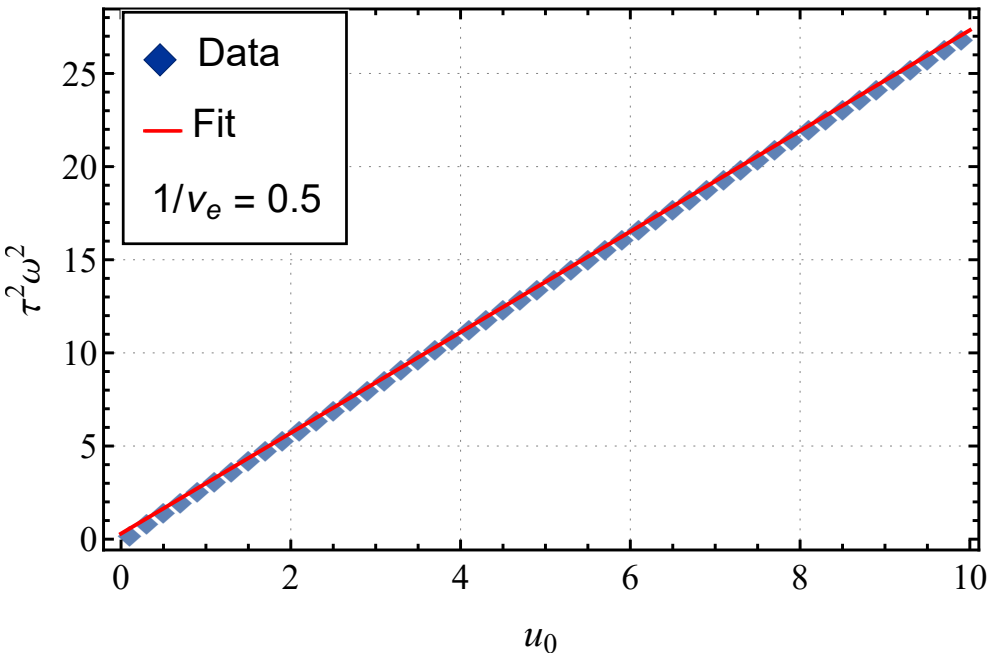

Figure 7.4.: Data and linear fit of the lowest order eigenvalue of eq. 7.3 with $1/\nu_e = 0.5$ determined over the variational principle. The parameters of the fit are given in Tab. 7.3. The error bars are to small to be shown in the plot.

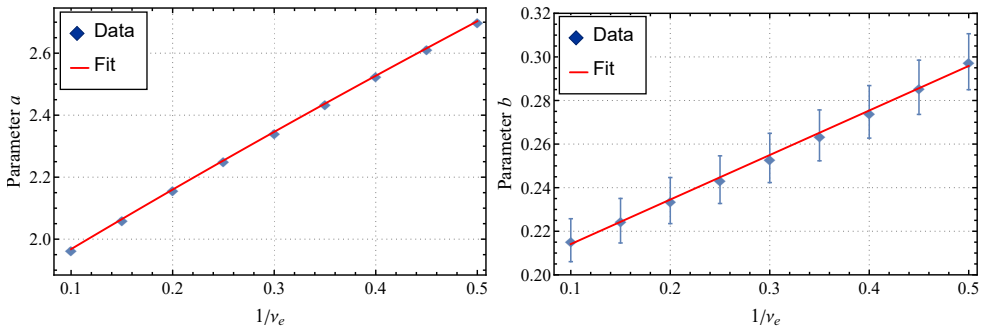

Figure 7.5.: Data and fits of the fitting parameter form the linear fits of Fig. 7.4 and D.3 with respect to $1/\nu_e$. The parameter a (left) is the slope of the fits and the parameter b (right) is the y-intercept. The parameters of the shown fits are in Tab. 7.4.

a	b
2.70 ± 0.01	0.300 ± 0.013

Table 7.3.: Parameters of the fit in Fig. 7.4 to the model $au_0 + b$.

	α	β	γ
Param. a	5.74 ± 0.21	0.704 ± 0.028	-3.97 ± 0.21
Param. b		0.204 ± 0.004	0.194 ± 0.001

Table 7.4.: Parameters of the fits in Fig. 7.5. The fit model was $\alpha\sqrt{1+\beta/\nu_e}+\gamma$ for the parameter a and $\beta/\nu_e + \gamma$ for the parameter b.

7.1.4. Ground State Eigenvalue with the Software Mathematica

The variational principle provides results close to the real eigenvalues, when the test function approximates the real ground state sufficiently well. This is the case for small u_0, which is why the quantitative scaling in the low u_0 regime can be taken from eq. 7.5. For large u_0 we want to reduce the error, which comes from the WKB approximation. Therefore, determine the ground state eigenvalue of eq. 7.3 again over the function "NDEigensystem" from Mathematica (cf. sec. 6.1.4). First we take a look at a solution for the ground state eigenvalue in Fig. 7.6 together with a fit. We see a similar linear behaviour for large u_0 as in sec. 7.1.2. For the best results we have to again determine an optimal range which we put in to the function as the region. For this the solutions for different ranges were fitted with the linear model $au_0 + b$ and the results of the fitting parameter with respect to the range for $1/\nu_e = 0.5$ is shown in Fig. 7.7. For low ranges the parameters oscillate significantly with respect to the ranges. Within the segment of ranges in between 80 and 120 $x^{\lambda}_{\mathrm{DW}}$, the parameter a is almost constant and is similar to the results from the WKB approximation. Thus we choose the mean (weighted by the errors) of all the fitting parameter solutions in this segment as an estimate of the real value. Similar to the previous sections we repeat the calculations for different values of ν_e to find a general expression for the ground state eigenvalue. The estimates of the parameters a and b with respect to $1/\nu_e$ are visualized in Fig. 7.8. This data was fitted similar as in the previous two sections and the fitting parameters are in Tab. 7.6. We receive as an estimate for the eigenvalue for large u_0

$$\tau^2\omega^2 = (2.47\sqrt{1+1.72/\nu_e} - 2.03)u_0 + 0.0127/\nu_e + 0.868. \tag{7.6}$$

We have shown that 180° domain walls are pinned by relative strains localized at the domain wall. Similar to the situation of 90° domain wall pinned by spontaneous strains, the frequency of the lowest magnon mode scales with the

magnetoelastic coupling over $\omega \sim \sqrt{u_0}$. As we did for the 90° domain wall we will also compute the force which is necessary to overcome the pinning of a 180° wall in the following section.

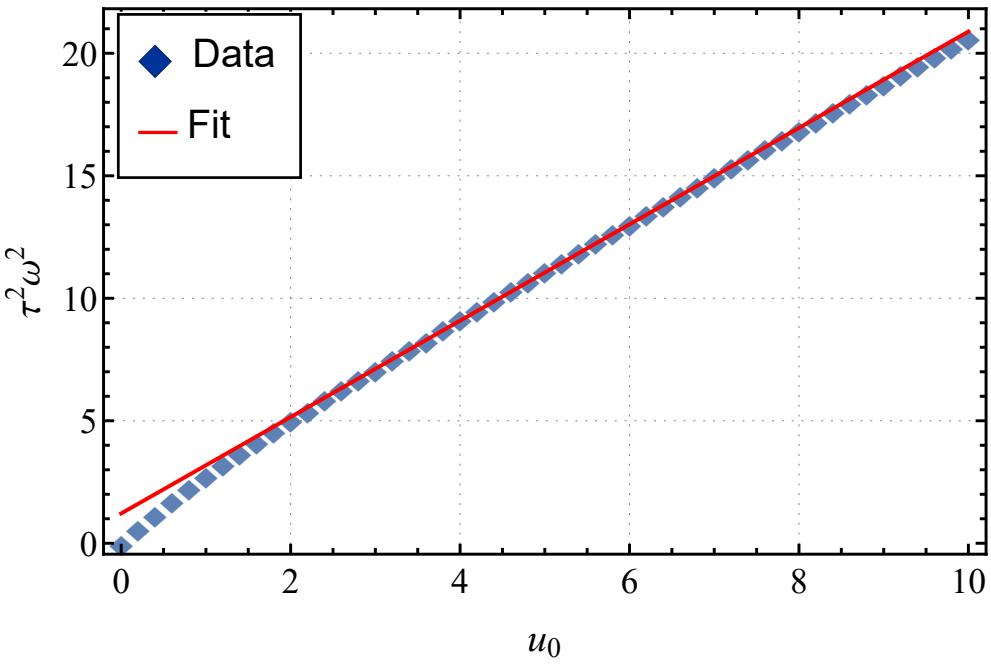

Figure 7.6.: Data and linear fit of the lowest order eigenvalue of $\mathcal{H}_{180}$ computed with Mathematica in a range of 10 $x^{\lambda}_{\mathrm{DW}}$. The fitting parameters are shown in Tab. 7.5.

a	b
1.97 ± 0.01	1.22 ± 0.04

Table 7.5.: Fitting parameters of the fit in Fig. 7.6 for the model $au_0 + b$.

α	β	γ
2.47 ± 0.94	1.72 ± 0.61	-2.03 ± 1.01
	-0.0127 ± 0.0130	0.868 ± 0.004

Table 7.6.: Fitting parameters of the fit in Fig. 7.6. The fit model was $\alpha\sqrt{1+\beta/\nu_e} + \gamma$ for the parameter a and $\beta/\nu_e + \gamma$ for the parameter b.

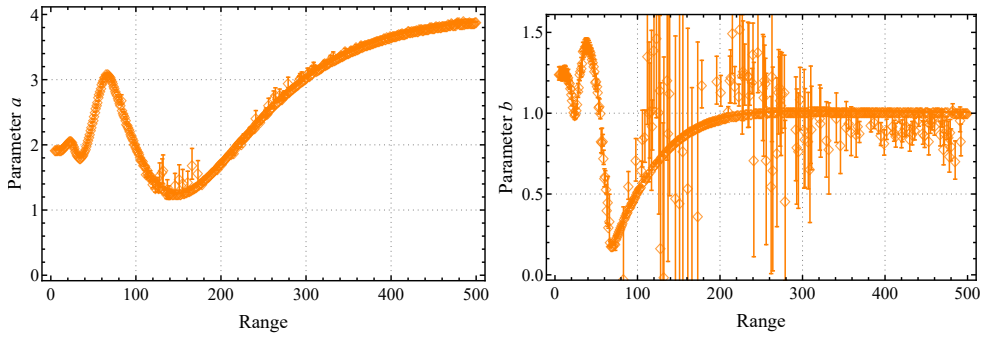

Figure 7.7.: Fitting parameters of the eigenvalues of $\mathcal{H}_{180}$ with respect to u_0. The eigenvalues were determined with Mathematica for different ranges in the input regions and the fit model was $au_0 + b$.

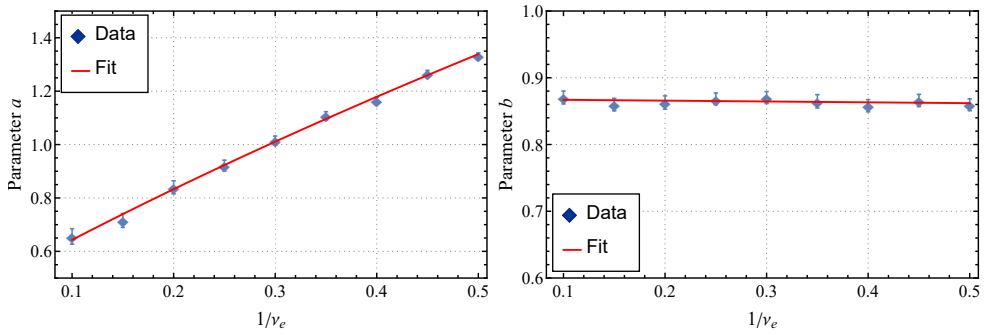

Figure 7.8.: Fitting parameters of the eigenvalues of $\mathcal{H}_{180}$ with respect to u_0. The eigenvalues were determined with Mathematica for different ranges in the input regions and the fit model was $au_0 + b$.

7.2. Pinning Force

Similar to a 90° domain wall we can pin a 180° domain wall by frozen strains. Since the relative and not spontaneous strains are responsible for the pinning in the 180° case, the strength of the pinning is expected to be lower than for a 90° domain wall. This is demonstrated by the lower eigenfrequencies, which were computed in the previous sections and we can further show this effect by computing the pinning force of the 180° wall. For this we calculate the pinning potential within the approximation $\cos\phi = -\tanh(\alpha_\lambda \mathcal{X})$

$$
\begin{aligned}
U_{\text{pin}}(X) =& \int_{\mathbb{R}} d\mathcal{X}\ \mathcal{W}(\phi(\mathcal{X}-X), \hat{u}(\mathcal{X})) \\
=& 4u_0 \int_{\mathbb{R}} \Big[-1 + (1 - 2\,\text{sech}(\alpha_\lambda \mathcal{X})(1 - 2\,\text{sech}(\alpha_\lambda(\mathcal{X}-X)) \\
&+ \frac{4}{\nu_e} \tanh(\alpha_\lambda \mathcal{X})\,\text{sech}(\alpha_\lambda \mathcal{X})\tanh(\alpha_\lambda(\mathcal{X}-X))\,\text{sech}(\alpha_\lambda(\mathcal{X}-X)) \Big] \\
=& \frac{8u}{\alpha_\lambda} \Big[2\pi + (16 + 8X(1-\nu_e)\frac{\exp(X)(1+\exp(2X)))}{\nu_e(-1+\exp(2X))^2} \\
&+ 16X(3+\nu_e)\frac{\exp(3X)}{\nu_e(-1+\exp(2X))^3} \Big]
\end{aligned}
\tag{7.7}
$$

and the repulsive force $F(X) = -U'_{\text{pin}}(X)$ in units of $1/x^\lambda_{\text{DW}}$. Again a constant was added into the energy density for convergence. Potential and force are plotted in Fig. 7.9 for $1/\nu_e = 0.5$. We see that the repulsive force decreases beyond a certain X, which happens because the strains, which are responsible for the pinning, are only located at the domain wall. The pinning force F_{pin} corresponds to the maximum of F similar to sec. 6.2 and is computed for multiple values of ν_e. The dependency from F_{pin} of $1/\nu_e$ is plotted and fitted in Fig. 7.10 with fitting parameters in Tab. 7.7. From this we can determine a general formula of the pinning force

$$
F_{\text{pin}} = 4u_0(0.213(1 + 1.75/\nu_e)^2 + 0.633)/x^\lambda_{\text{DW}}. \tag{7.8}
$$

In the regime $1/\nu_e \in [0, 0.5]$ (i.e. $\nu \in [0, 0.5]$ which is motivated by [58]) the function in the brackets is always smaller than 1. The pinning force of a 90° domain wall therefore is more than two times larger than for a 180° domain wall. This fits to the expectation that the strains, localized at the domain wall induce a weaker pinning than the global spontaneous strains. The pinning by spontaneous and relative strains demonstrates that a strong magnetoelastic coupling stabilizes an AFM multi-domain system against electromagnetic noise. Thus, AFMs with strong magnetoelastic coupling may have a higher stability as memories against disturbing signals and require further investigation, which goes over the scope of this work. In conclusion we have seen in the last two chapters, that not only static but also dynamic properties of AFMs are influenced by the interaction between strains and Néel vector, such that the orientation, shape and pinning of a domain wall is determined by the interaction strength.

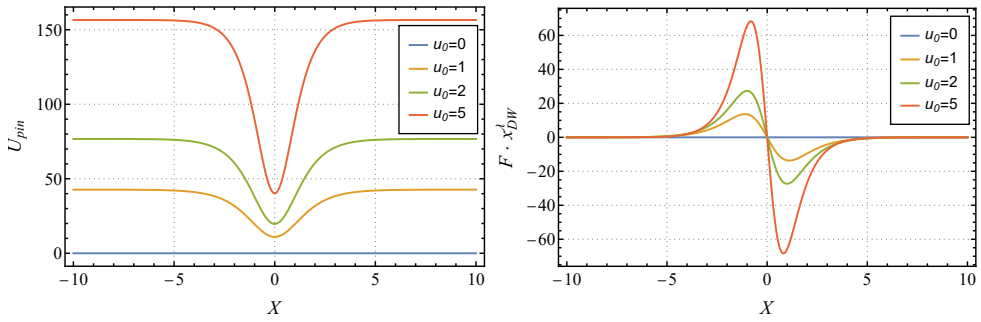

Figure 7.9.: Potential (left) and force (right) which correspond to a shift of a 180° domain wall with frozen relative strains away from equilibrium. The pinning potential approaches a constant value for large values of $\mathcal{X}$ and the repulsive force therefore decreases to 0 after going through an extremum.

α	β	γ
0.213 ± 0.004	1.75 ± 0.03	0.633 ± 0.005

Table 7.7.: Fitting parameters of the fit in Fig. 7.10 to the model $\alpha(1+\beta/\nu_e)+\gamma$.

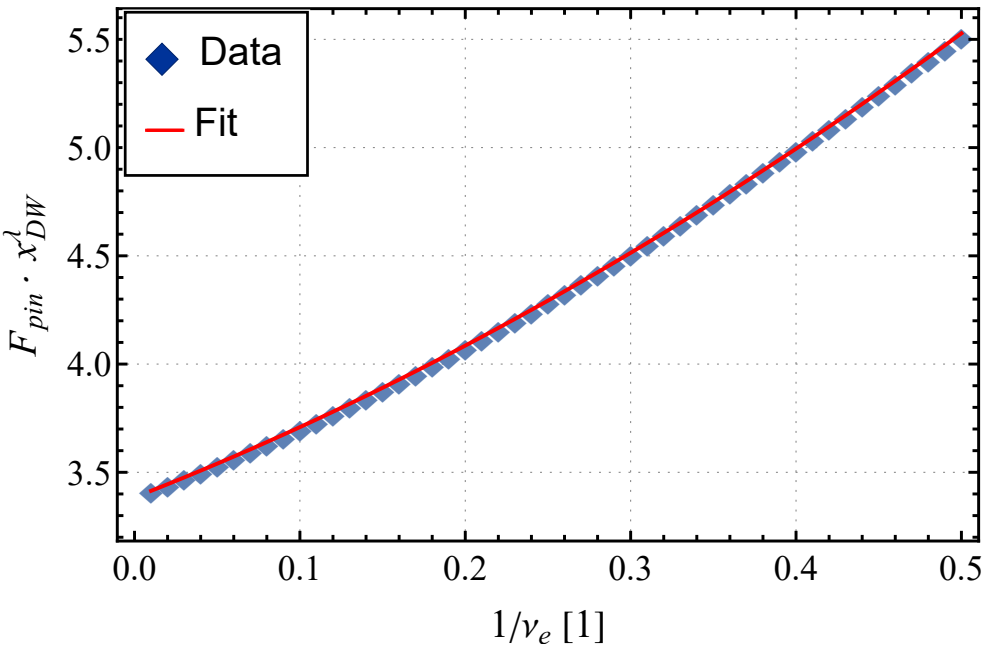

Figure 7.10.: The Pinning force against the parameter ν_e. The calculated data (blue) was fitted which is also shown (red). The fitting parameters are in Tab. 7.7

8. Conclusion and Outlook

We have computed the energy of magnetic domain walls in collinear AFMs in presence of magnetoelastic interactions with respect to the orientation of the domain walls in the system. We have seen that incompatibilities of spontaneous strains for 90° domain walls increase the energy and lead to two preferred axes for the domain wall alignment, where the incompatibility is 0. Further without incompatibilities in 180° domain walls, the strains which are localized at the domain wall also induce a similar anisotropy of the domain wall.
We have shown that the width of a domain wall shrinks with stronger magnetoelastic coupling and also quantified this effect. For a flat domain wall strains act as an effective uniaxial anisotropy along the currents Néel vector axis in the respective domains. Thus, the anisotropy constant in the domain wall width without coupling is rescaled to the sum of anisotropy and magnetoelastic coupling strength. Such an increase in the anisotropy then naturally leads to thinner domain walls.
To further explore the domain wall anisotropy we determined the shape of a closed domain wall loop under magnetoelastic coupling. When the loop has a fixed length, the minimal energy always corresponds to a rectangle whose sides go along the domain wall easy axes, independent of all coupling constants. In this case the shape of domain wall loop is purely determined by the effect of the magnetoelastic coupling. If the area enclosed by the loop is fixed the anisotropy and exchange stiffness, which prefer a circular shape, compete against the magnetoelastic coupling and we receive shapes inbetween circles and squares. How far a shape tends to a circle or square shape is determined by the ratio of magnetoelastic coupling to anisotropy.
Finally, we have shown that 90° domain walls are pinned when the spontaneous strains are frozen. The role of strains as an additional anisotropy in both domains lead to an increase in the energy when the domain wall profile is changed, thus creating a localised magnon mode. We have quantified this mode by computing its oscillation frequency and further determined the strength of the pinning by calculating the force which acts on the domain wall after a shift from the pinning center. We repeated the steps for 180° domain wall but the pinning is now induced by the strains which are localized at the domain wall and not the spontaneous strains. Thus, while the repulsive force of a 90° wall saturates to a fixed value, as the spontaneous strains are present in the whole domain, in a 180° wall the force decreases to 0 far away from the wall, when the strains at the domain wall are decayed.

To proceed with the investigation of the static phenomena, a possible way is to study boundary effects onto the domain wall anisotropy. From this, we can move on and place the AFM onto a nonmagnetic substrate. The incompatibility of spontaneous strains at the AFM substrate interface leads to a multi-domain system and may also effect the shape of the domain walls. If we replace the paramagnetic substrate by a FM, the interaction between the order parameters of FM and AFM will further influence the domain wall anisotropy. The demagnetization field of the FM and the magnetoelastic interactions in the AFM strive to different domain structures. Thus, a strong coupling between FM and AFM order parameters will possibly lead to some shape in between structures and to a new domain wall anisotropy. Especially the closed domain wall loop will change its shape away from the purely magnetoelastic square. Aside of this, it would be useful to investigate the effect of the magnetoealstic coupling onto other AFM quantities e.g. the spin flop field in uniaxial AFMs [74]. Another step to go from this work, is to consider more complex magnetic profile than a two domain system. The obtained knowledge of how strains and magnetic degrees of freedom interact could then be compared to experimental data. This will allow to find the role which the magnetoelastic coupling plays in the domain profile and helps to understand the equilibrium domain structure of AFMs.

In the dynamical regime, a possible next step is to compute more quantities of the pinned domain wall e.g. reflection and transmission coefficient of spin waves. In the case of a 90° wall it could also help to make the calculations more accurate by including the relative strains. Another way to proceed is to drop the approximation that the lattice is frozen and to include the time dependency of strains. This will lead to very complex differential equations and requires numerical simulations or simplified situations e.g. a domain wall moving at constant speed but will help to determine the dynamical behaviour of an AFM on longer time scales. Another suggested direction for future research, is to study the switching of the AFM state by applying strains. The role of the strain as an effective anisotropy allows to define an easy axis and therefore the magnetic profile. With an appropriate change of the strain profile, the easy axis and thus the magnetic profile will change. To study the mechanism of such a switching we need to consider the dynamics of the Néel vector under a time dependent external strain field. Experiments already provided results in this direction [75], so a theoretical study would be desirable.

In conclusion, we have shown that the presence of magnetoelastic interaction influences static and dynamic properties of AFMs, thus making it necessary to study different effects from the interaction in order to understand the behaviour of the AFM domain structure.

A. Strains Corresponding to a Uniform Magnetic State

In order to compute the spontaneous strains for a magnetic system we need to know the strains corresponding to a uniform magnetic profile. We find them by minimizing the energy terms from chapter 2 for constant strains

$$0 = \frac{\partial(\mathcal{W}_{elas} + \mathcal{W}_{me})}{\partial u_{ij}}, \quad i,j \in \{x,y,z\}, \tag{A.1}$$

such that the stress in the system is 0. This provides six equations which define the equilibrium strain profile

$$0 = \frac{2\mu(1-\nu)}{1-2\nu}u_{xx} + \frac{2\mu\nu}{1-2\nu}(u_{yy}+u_{zz}) + \lambda(n_x^2 - n_y^2) \tag{A.2}$$
$$0 = \frac{2\mu(1-\nu)}{1-2\nu}u_{yy} + \frac{2\mu\nu}{1-2\nu}(u_{zz}+u_{xx}) - \lambda(n_x^2 - n_y^2) \tag{A.3}$$
$$0 = \frac{2\mu(1-\nu)}{1-2\nu}u_{zz} + \frac{2\mu\nu}{1-2\nu}(u_{xx}+u_{yy}) \tag{A.4}$$
$$0 = 4\mu u_{xy} + 4\lambda n_x n_y \tag{A.5}$$
$$0 = 4\mu u_{yz} \tag{A.6}$$
$$0 = 4\mu u_{zx} \tag{A.7}$$

Equations A.5, A.6 and A.7 directly show

$$u_{xy} = -\frac{\lambda}{2\mu}2n_x n_y \tag{A.8}$$
$$u_{yz} = u_{zx} = 0 \tag{A.9}$$

Subtracting equation A.3 from A.2 gives

$$\begin{aligned} 0 &= \frac{2\mu(1-\nu)}{1-2\nu}(u_{xx}-u_{yy}) - \frac{2\mu\nu}{1-2\nu}(u_{xx}-u_{yy}) + 2\lambda(n_x^2 - n_y^2) \\ &= 2\mu(u_{xx}-u_{yy}) + 2\lambda(n_x^2 - n_y^2) \end{aligned}$$

After reordering and with similar calculations for equation A.4 we get

$$u_{xx} - u_{yy} = -\frac{\lambda}{\mu}(n_x^2 - n_y^2) \tag{A.10}$$

$$u_{xx} - u_{zz} = -\frac{\lambda}{2\mu}(n_x^2 - n_y^2) \tag{A.11}$$

$$u_{yy} - u_{zz} = \frac{\lambda}{2\mu}(n_x^2 - n_y^2) \tag{A.12}$$

Now we can add equations A.11 and A.12, which gives $2u_{zz} = u_{xx} + u_{yy}$. Together with equation A.4 it follows that $u_{zz} = 0$ and therefore

$$u_{xx} = -\frac{\lambda}{2\mu}(n_x^2 - n_y^2) \tag{A.13}$$

$$u_{yy} = \frac{\lambda}{2\mu}(n_x^2 - n_y^2) \tag{A.14}$$

The spontaneous strain of a multi-domain system then takes the in this section computed values for in each domain respectively and flips instantly at the domain walls.

B. Solution of the 2D Navier Equation with a Force with One Dimensional Domain

Note: All calculation rules, that were used here for the Fourier transform were taken from [76].
Consider the equation

$$\nabla^2\mathbf{u}(\xi,\eta) + \sigma\nabla(\nabla\cdot\mathbf{u}(\xi,\eta)) = \mathbf{f}(\xi) = \partial_\xi\boldsymbol{\alpha}(\xi) \tag{B.1}$$

with $\mathbf{u} = (u_\xi, u_\eta)^T \in L^1_{\text{loc}}(\mathbb{R}^2)$, $\boldsymbol{\alpha} = (\alpha_\xi, \alpha_\eta)^T \in L^1_{\text{loc}}(\mathbb{R}^2)$ and $\nabla = \mathbf{e}_\xi\partial\xi + \mathbf{e}_\eta\partial\eta$, where L^1_{loc} is the space of locally integrable functions. The derivatives are interpreted as weak derivatives. We want to Fourier transform the upper equation, but since the functions only need to be locally integrable we cannot necessarily do this. If we further restrict the functions to be non diverging we can formally still define a Fourier transform, where possible divergences in the Fourier integral, will be given by a δ-function e.g. $\int_{\mathbb{R}} dx \exp(ikx) = 2\pi\delta(k)$ (cf. [77]). Let $\mathbf{v}$ be the Fourier transform of $\mathbf{u}$ and $\boldsymbol{\beta}$ be the Fourier transform of $\boldsymbol{\alpha}$. Then the full Fourier transformation of eq. B.1 gives

$$-\mathbf{k}^2\mathbf{v}(k_\xi,k_\eta) - \sigma\mathbf{k}(\mathbf{k}\cdot\mathbf{v}(k_\xi,k_\eta)) = 2\pi k_\xi\delta(k_\eta)\boldsymbol{\beta}(k_\xi). \tag{B.2}$$

The upper equation can be solved for the components v_ξ and v_η of $\mathbf{v}$ to receive

$$\begin{aligned} v_\xi(k_\xi,k_\eta) &= -\sqrt{2\pi}ik_\xi\delta(k_\eta)\frac{\left(k_\xi^2 + (1+\sigma)k_\eta^2\right)\beta_\xi(k_\xi) - \sigma k_\xi k_\eta\beta_\eta(k_\xi)}{(1+\sigma)(k_\xi^2+k_\eta^2)^2} \\ v_\eta(k_\xi,k_\eta) &= -\sqrt{2\pi}ik_\xi\delta(k_\eta)\frac{-\sigma k_\xi k_\eta\beta_\xi(k_\xi) + \left((1+\sigma)k_\xi^2 + k_\eta^2\right)\beta_\eta(k_\xi)}{(1+\sigma)(k_\xi^2+k_\eta^2)^2} \end{aligned} \tag{B.3}$$

We transform back into the real space by first computing the integral

$$\begin{aligned} \tilde{v}_\xi(k_\xi) &:= \frac{1}{\sqrt{2\pi}}\int_{\mathbb{R}} dk_\eta v_\xi(k_\xi,k_\eta)\exp(-ik_\eta\eta) = -i\frac{\beta_\xi(k_\xi)}{(1+\sigma)k_\xi} \\ \tilde{v}_\eta(k_\xi) &:= \frac{1}{\sqrt{2\pi}}\int_{\mathbb{R}} dk_\eta v_\eta(k_\xi,k_\eta)\exp(-ik_\eta\eta) = -i\frac{\beta_\eta(k_\xi)}{k_\xi} \end{aligned} \tag{B.4}$$

Multiplying these expressions with ik_ξ and performing an inverse Fourier transform then yields

$$\begin{aligned}\partial_\xi u_\xi(\xi) &= \frac{\alpha_\xi(\xi)}{1+\sigma} \\ \partial_\xi u_\eta(\xi) &= \alpha_\eta(\xi)\end{aligned}$$

as the homogeneous solution of eq. B.1. The dependency of η got lost in the integral of eq. B.4 so derivatives of $\mathbf{u}$ with respect to η are 0. If we interpret $\mathbf{u}$ as a displacement, the associated strains then are

$$\begin{aligned}u_{\xi\xi}(\xi) = \partial_\xi u_\xi(\xi) &= \frac{\alpha_\xi(\xi)}{1+\sigma} \\ u_{\xi\eta} &= \frac{1}{2}\partial_\xi u_\eta(\xi) = \frac{\alpha_\xi(\xi)}{2} \\ u_{\eta\eta} &= 0\end{aligned} \tag{B.5}$$

C. Simulation of the Domain Wall Anisotropy with MuMax3

C.1. 180° Domain Wall

MuMax3 is a software to simulate FMs in a micromagnetic picture. In the static case the software can also be used for an AFM, when the normalized magnetization $\mathbf{m}$ is interpreted as the Néel vector and demagnetization is turned off. We simulate a thin film of one cell along z and a square geometry of 128 cells in the xy-plane. The cell size is 3.5 nm and the saturation magnetization i.e. the absolute value of the magnetization in each cell was chosen to be M_sat 800 kA/m. For our simulation we used the already available exchange interaction and uniaxial anisotropy (along z). They are defined over the parameters A (which is the same as we use in the calculations) and $Ku1$ ($= K_1$). Further we implemented a field to imitate another uniaxial anisotropy along x with the strength parameter Kx ($= K_2$). This is done by defining a new energy density $\mathcal{W}$ which corresponds to the anisotropy energy density and the effective magnetic field $-\partial\mathcal{W}/\partial(\mathbf{m}M\_sat)$. The strains are introduced as fields which depend on the magnetization corresponding to eq. 3.6 and the energy densities containing strains as well as their effective fields are included in the system. The strength of the magnetoelastic coupling is tuned by the parameter l such that $u_0 = l/Kx$. All the parameters, that were used are in Tab. C.1. For four different values of l we scan through different angles of ψ and determine the energy of the domain wall. This is done by an initializing a two domain system with a wall normal to ψ and relaxing the system. In order to not have boundary effects the square geometry is rotated with the domain wall. The results from the simulation are shown in Fig. C.1. They reproduce the qualitative results from the calculations but the depth of the minima varies compared to Fig. 3.1. This is not surprising, since we compare an infinite and continuous to a finite and discrete system. Nevertheless, the similar qualitative behaviour verifies the results obtained in sec. 3.1 also for finite size systems.

A [J/m]	$Ku1$ [J/m^3]	Kx [J/m^3]
10^{-11}	-10^5	10^3

Table C.1.: Parameters which are used in the simulation of the two domain system for every simulation. M_sat is the saturation magnetization

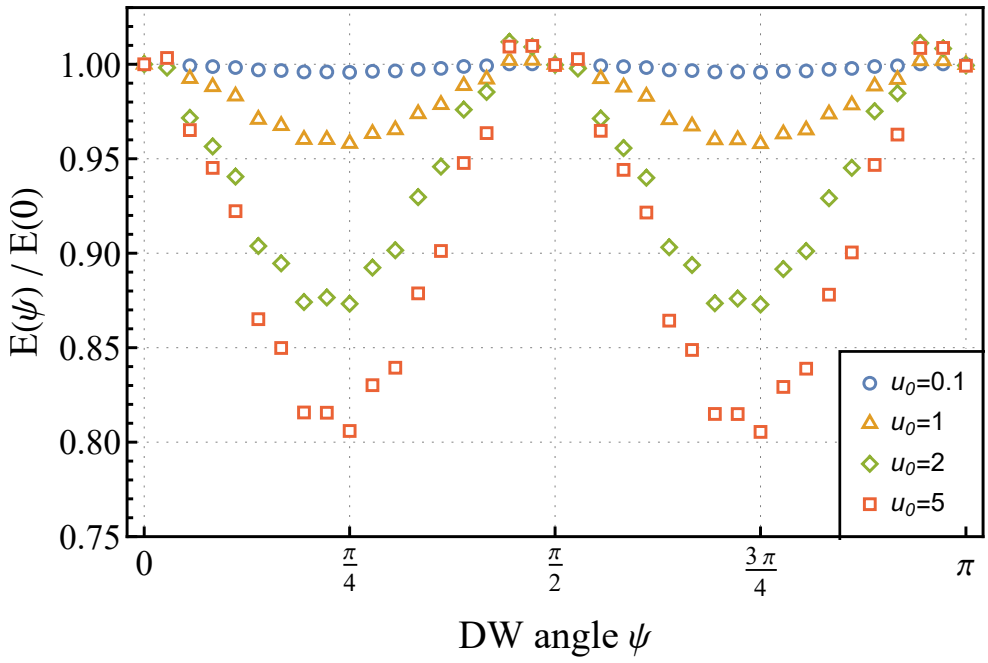

Figure C.1.: Energy E for a 180° domain wall plotted against the domain wall orientation angle ψ for different values of the dimensionless magnetoelastic coupling parameter $u_0 = l/Kx$ determined with MuMax3.

C.2. 90° Domain Wall

Now we want to also simulate a 90° domain wall with spontaneous strains. For this we replace the uniaxial anisotropy along x by an in plane anisotropy with x and y as easy axes with the strength $Kxy = Kx$. Other parameters stay the same. The strain fields are now constants in two regions and thus are introduced as an uniaxial anisotropy in the respective domains. Since the spontaneous strains are quadratic in the Néel vector of the domain and the strains itself occur quadratically in the elastic energy density the anisotropy is of fourth order. Together with the compensating strains the strain scales with ψ over $u_{xx} \sim \pm 1 + \cos(2\psi)$ and $u_{yy} \sim \mp 1 + \cos(2\psi)$. The elastic energy

density consists of terms with $u_{xx}^2 + u_{yy}^2$ and $u_{xx}u_{yy}$ and the strength of the additional anisotropy will therefore be $l(1 + \cos^2(2\psi))$ with the strength parameter l. The results for the energy are shown in Fig. C.2. There we see minima at the expected angles and further that the depth of the minima is significant larger than for the situation of a 180° domain wall with relative strains. While the first result may be viewed as trivial due to the strength of the effective anisotropy the second observation demonstrates that the effect of incompatibilities onto the equilibrium domain energy is much larger than the effects of relative strains as argued before. This verifies the argument that it is enough to consider incompatibilities for non 180° domain walls to find their anisotropy.

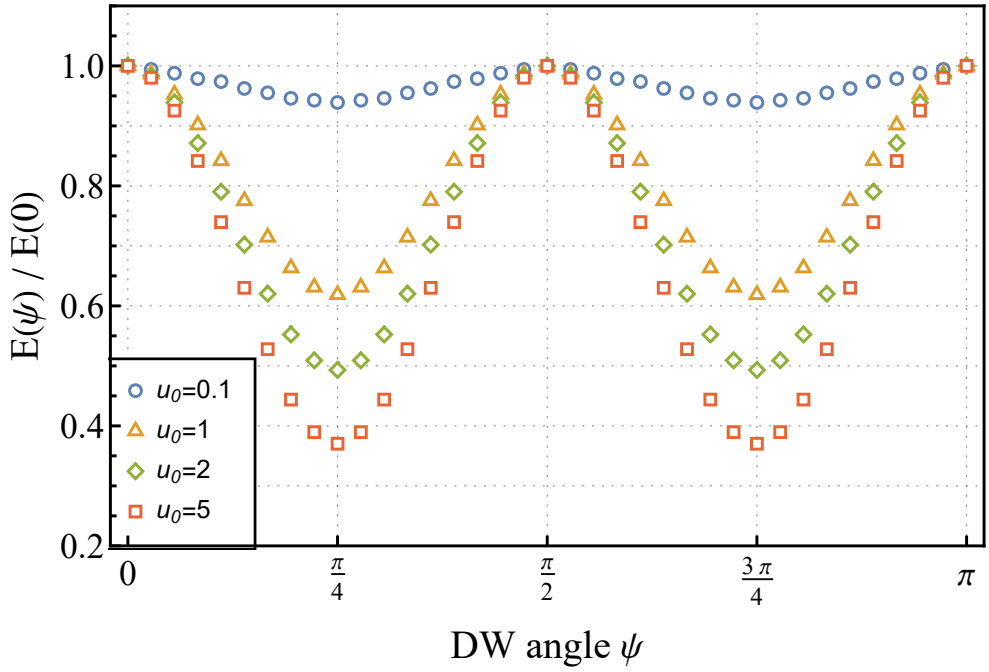

Figure C.2.: Energy E for a 90° domain wall plotted against the domain wall orientation angle ψ for different values of the dimensionless magnetoelastic coupling parameter $u_0 = l/Kxy$ determined with MuMax3.

D. Additional Material Calculations of Pinned Domain Walls

D.1. Variational Principle for a Pinned 90° Domain Wall with Different Test functions

In this section we apply the variational principle from sec. 6.1.3 to more test functions in order to justify the result from the hyperbolic approach. We consider a Gaussian and a Lorentzian as test functions. These approximations of the ground state with a Gaussian and Lorentzian have the following form

$$\psi_\beta^G(\mathcal{X}) = \left(\frac{2\beta}{\pi}\right)^{1/4} \exp(-\beta\mathcal{X}^2)$$
$$\psi_\beta^L(\mathcal{X}) = \left(\frac{2\beta^3}{\pi}\right)^{1/2} \frac{1}{\beta^2+\mathcal{X}^2}.$$

Similar to sec. 6.1.3 we scan through β and search for the minimum in $\langle\psi_\beta^{G/L}|\,\mathcal{H}_{90}\,|\psi_\beta^{G/L}\rangle$. The results with linear fit are shown in Fig. D.1 and the fitparameters are in Tab. D.1

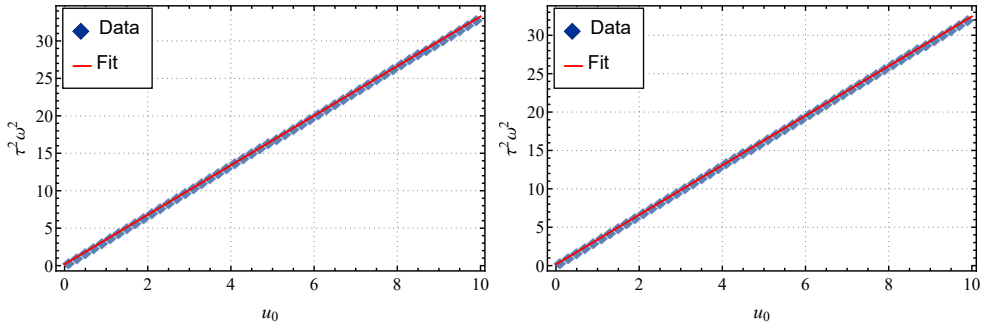

Figure D.1.: Data and linear fit of the lowest order eigenvalue of eq. 6.4 determined over the variational principle with a Gaussian (left) and Lorentzian (right) test function. The parameters of the fit are given in Tab. D.1. The error bars are to small to be shown in the plot.

	a	b
G	3.31 ± 0.01	0.178 ± 0.006
L	3.27 ± 0.01	0.154 ± 0.005

Table D.1.: Parameters of the fit in Fig. D.1 to the model $au_0 + b$. The label G or L distinguishes between the Gaussian and Lorentzian test function.

D.2. Ground State Eigenvalues for a pinned 180° Domain Wall for Different Poisson Ratios

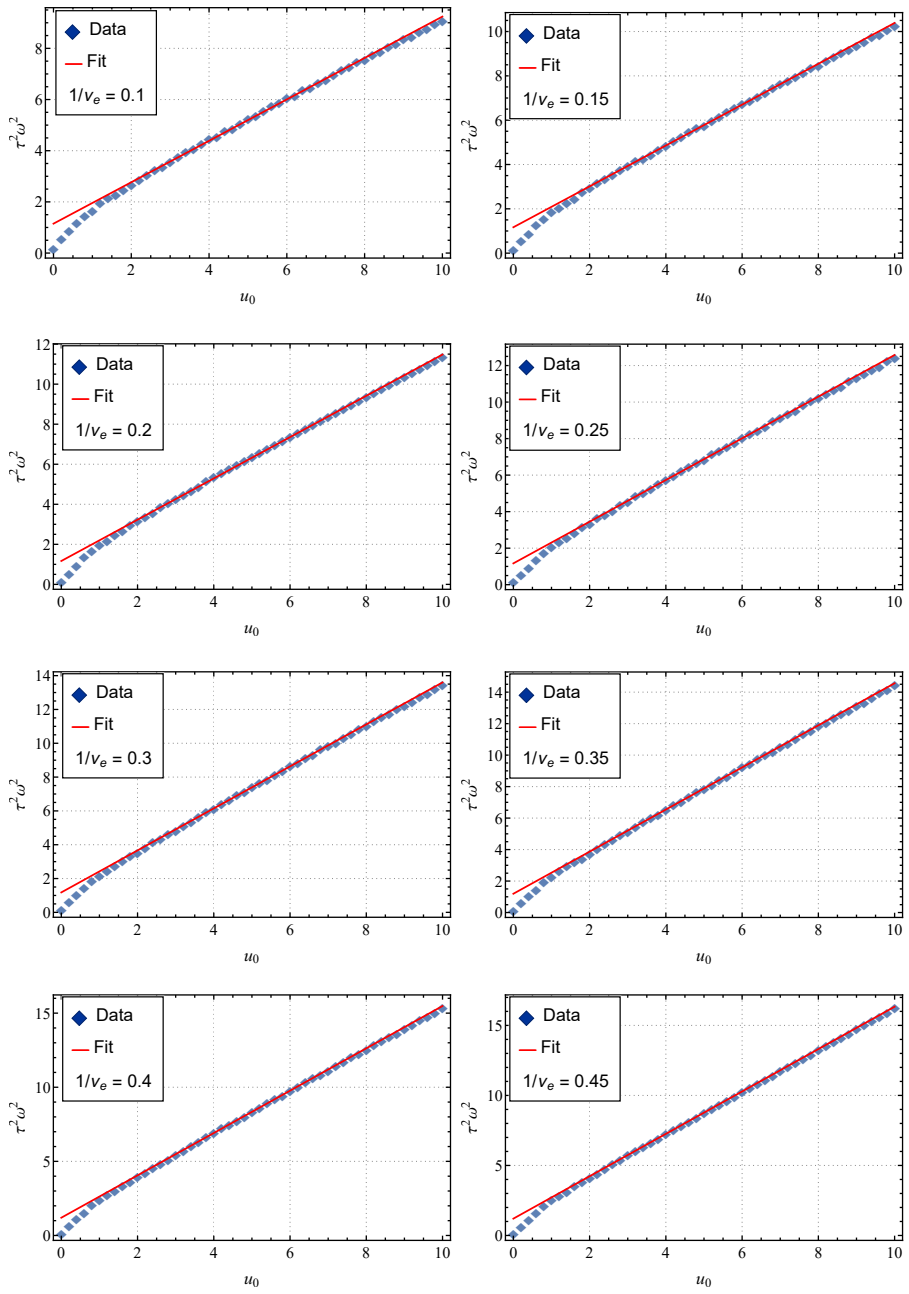

Figure D.2.: Data and Fits for the ground state eigenvalues, which were determined over the WKB approximation in sec. 7.1.2. The Fitmodel is $au_0 + b$, the fitparameters are in Tab. D.2. The errors are to small to be visualized in the plot.

	a	b
$1/\nu_e = 0.1$	0.837 ± 0.005	1.18 ± 0.03
$1/\nu_e = 0.15$	0.968 ± 0.005	1.18 ± 0.03
$1/\nu_e = 0.2$	1.09 ± 0.01	1.19 ± 0.03
$1/\nu_e = 0.25$	1.21 ± 0.01	1.21 ± 0.03
$1/\nu_e = 0.3$	1.32 ± 0.01	1.22 ± 0.03
$1/\nu_e = 0.35$	1.43 ± 0.01	1.25 ± 0.03
$1/\nu_e = 0.4$	1.53 ± 0.01	1.27 ± 0.03
$1/\nu_e = 0.45$	1.63 ± 0.01	1.28 ± 0.03

Table D.2.: Parameters of the fits in Fig. D.2 to the model $au_0 + b$.

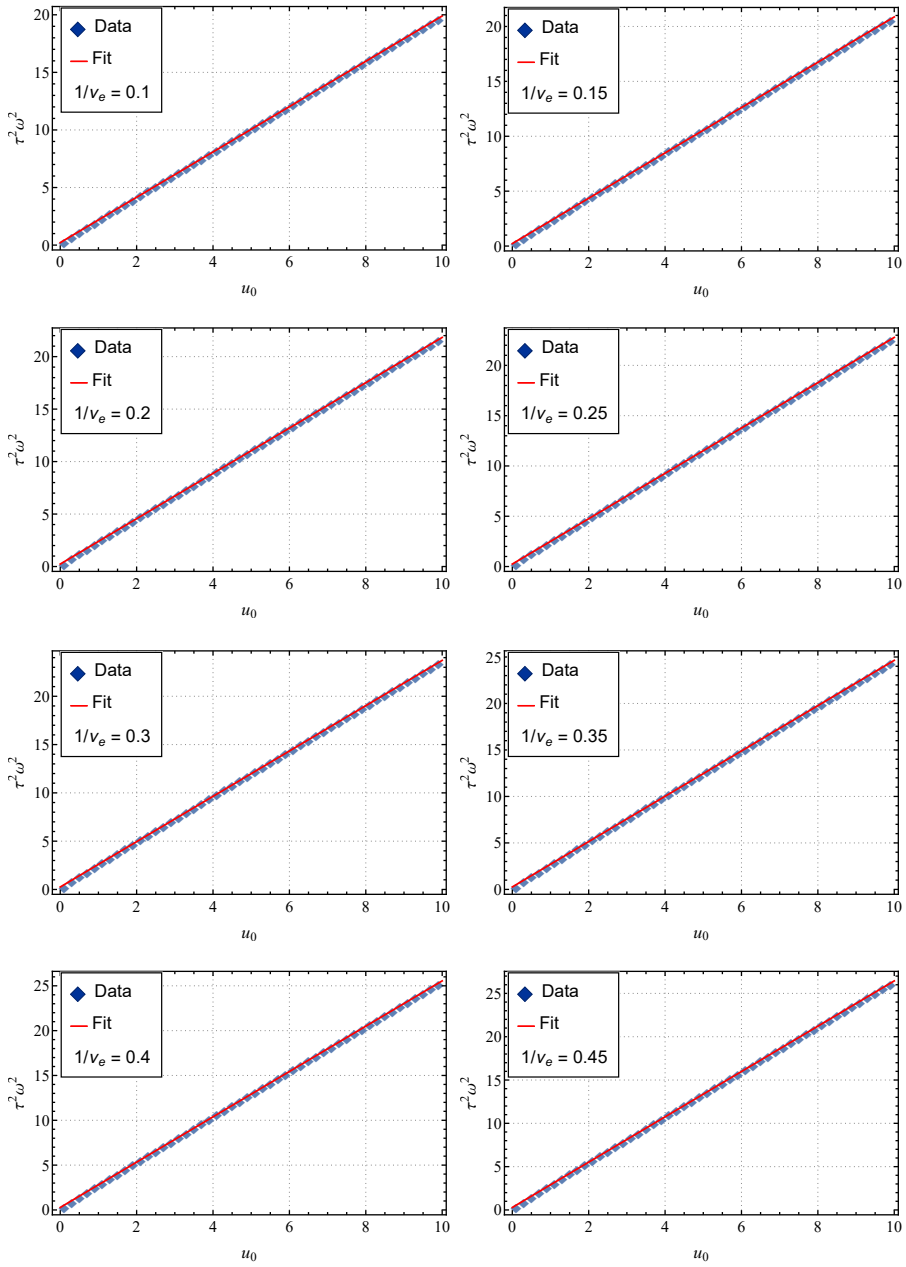

Figure D.3.: Data and Fits for the ground state eigenvalues, which were determined over the variational principle in sec. 7.1.3. The Fitmodel is $au_0 + b$, the fitparameters are in Tab. D.3. The errors are to small to be visualized in the plot.

	a	b
$1/\nu_e = 0.1$	1.97 ± 0.01	0.216 ± 0.009
$1/\nu_e = 0.15$	2.06 ± 0.01	0.225 ± 0.010
$1/\nu_e = 0.2$	2.16 ± 0.01	0.234 ± 0.010
$1/\nu_e = 0.25$	2.25 ± 0.01	0.244 ± 0.011
$1/\nu_e = 0.3$	2.35 ± 0.01	0.254 ± 0.011
$1/\nu_e = 0.35$	2.44 ± 0.01	0.264 ± 0.012
$1/\nu_e = 0.4$	2.53 ± 0.01	0.275 ± 0.012
$1/\nu_e = 0.45$	2.62 ± 0.01	0.286 ± 0.012

Table D.3.: Parameters of the fits in Fig. D.3 to the model $au_0 + b$.

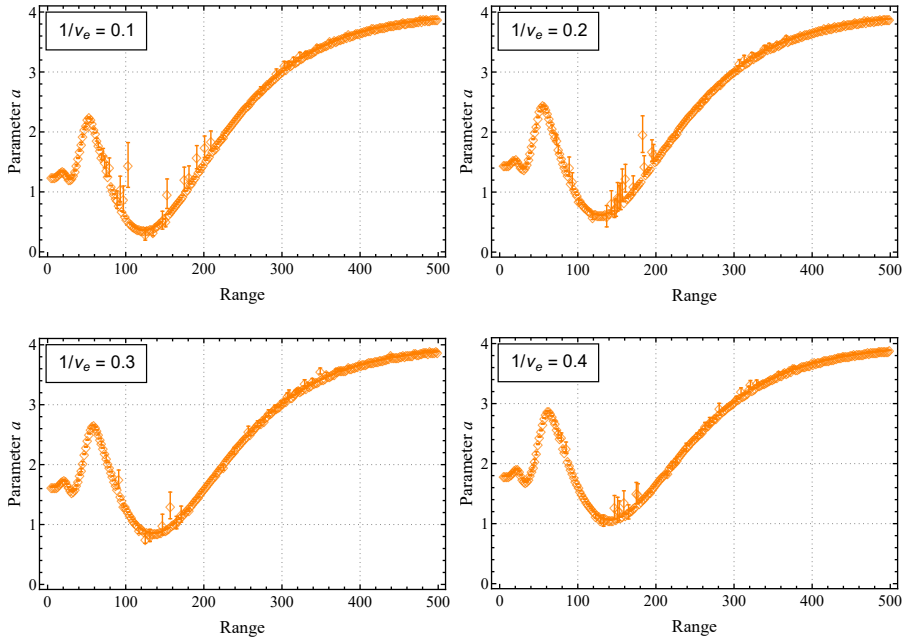

Figure D.4.: Fitting parameter a of the fit with the model au_0+b to the Eigenvalue of $\mathcal{H}_{180}$ with respect to the strength of the magnetoelastic coupling u_0 for different values of ν_e.

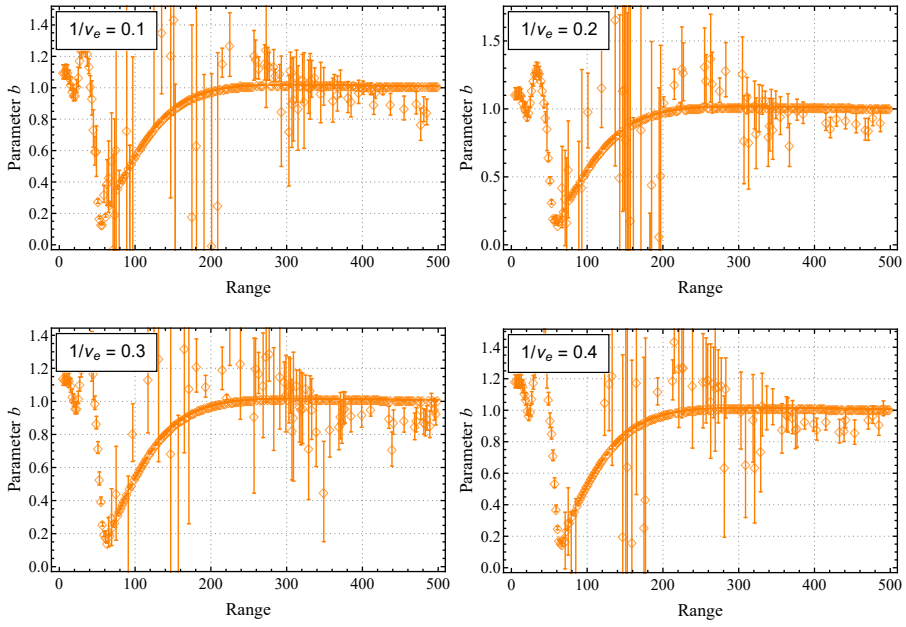

Figure D.5.: Fitting parameter a of the fit with the model au_0+b to the Eigenvalue of $\mathcal{H}_{180}$ with respect to the strength of the magnetoelastic coupling u_0 for different values of ν_e.

Bibliography

[1] Bandyopadhyay, Supriyo ; Cahay, Marc:
Introduction to spintronics.
CRC press, 2015

[2] Zhao, Weisheng ; Prenat, Guillaume:
Spintronics-based computing.
Springer, 2015

[3] Willoughby, Arthur ; Capper, Peter ; Kasap, Safa:
Spintronics for next generation innovative devices.
Wiley Online Library, 2015

[4] Hirohata, Atsufumi ; Takanashi, Koki:
Future perspectives for spintronic devices.
In: *Journal of Physics D: Applied Physics* 47 (2014), Nr. 19, S. 193001

[5] Puebla, Jorge ; Kim, Junyeon ; Kondou, Kouta ; Otani, Yoshichika:
Spintronic devices for energy-efficient data storage and energy harvesting.
In: *Communications Materials* 1 (2020), Nr. 1, S. 1–9

[6] Heide, C:
Spin currents in magnetic films.
In: *Physical review letters* 87 (2001), Nr. 19, S. 197201

[7] Chappert, Claude ; Fert, Albert ; Van Dau, Frédéric Nguyen:
The emergence of spin electronics in data storage.
In: *Nanoscience And Technology: A Collection of Reviews from Nature Journals* (2010), S. 147–157

[8] Dietl, Tomasz ; Awschalom, David D. ; Kaminska, Maria ; Ohno, Hideo:
Spintronics.
Academic Press, 2009

[9] Žutić, Igor ; Fabian, Jaroslav ; Sarma, S D.:
Spintronics: Fundamentals and applications.
In: *Reviews of modern physics* 76 (2004), Nr. 2, S. 323

[10] Ohno, Hideo:
A window on the future of spintronics.
In: *Nature materials* 9 (2010), Nr. 12, S. 952–954

[11] Bozorth, Richard M.:

Ferromagnetism.
1993

[12] White, Robert M. ; White, Robert M. ; Bayne, Bradford:
Quantum theory of magnetism. Bd. 1.
Springer, 1983

[13] Lienau, Richard M.:
Method and apparatus for reading data from a ferromagnetic memory cell.
März 29 2005. –
US Patent 6,873,546

[14] Mark, S ; Dürrenfeld, P ; Pappert, K ; Ebel, L ; Brunner, K ; Gould, C ; Molenkamp, LW:
Fully electrical read-write device out of a ferromagnetic semiconductor.
In: *Physical review letters* 106 (2011), Nr. 5, S. 057204

[15] Chang, Liu ; Wang, Min ; Liu, Lei ; Luo, Siwei ; Xiao, Pan:
A brief introduction to giant magnetoresistance.
In: *arXiv preprint arXiv:1412.7691* (2014)

[16] Parkin, Stuart S. ; Hayashi, Masamitsu ; Thomas, Luc:
Magnetic domain-wall racetrack memory.
In: *Science* 320 (2008), Nr. 5873, S. 190–194

[17] Parkin, Stuart ; Yang, See-Hun:
Memory on the racetrack.
In: *Nature nanotechnology* 10 (2015), Nr. 3, S. 195–198

[18] Dor, Oren B. ; Yochelis, Shira ; Radko, Anna ; Vankayala, Kiran ; Capua, Eyal ; Capua, Amir ; Yang, See-Hun ; Baczewski, Lech T. ; Parkin, Stuart Stephen P. ; Naaman, Ron u. a.:
Magnetization switching in ferromagnets by adsorbed chiral molecules without current or external magnetic field.
In: *Nature communications* 8 (2017), Nr. 1, S. 1–7

[19] Lintelo, Johannes Gerardus T.:
Magnetic stray fields of periodically arranged Co-Crmicro strips.
(1993)

[20] Bedau, D ; Liu, H ; Sun, JZ ; Katine, JA ; Fullerton, EE ; Mangin, S ; Kent, AD:
Spin-transfer pulse switching: From the dynamic to the thermally activated regime.
In: *Applied Physics Letters* 97 (2010), Nr. 26, S. 262502

[21] Garello, Kevin ; Avci, Can O. ; Miron, Ioan M. ; Baumgartner, Manuel ; Ghosh, Abhijit ; Auffret, Stéphane ; Boulle, Olivier ; Gaudin, Gilles ; Gambardella, Pietro:
Ultrafast magnetization switching by spin-orbit torques.

In: *Applied Physics Letters* 105 (2014), Nr. 21, S. 212402

[22] Prenat, Guillaume ; Jabeur, Kotb ; Vanhauwaert, Pierre ; Di Pendina, Gregory ; Oboril, Fabian ; Bishnoi, Rajendra ; Ebrahimi, Mojtaba ; Lamard, Nathalie ; Boulle, Olivier ; Garello, Kevin u. a.:
Ultra-fast and high-reliability SOT-MRAM: From cache replacement to normally-off computing.
In: *IEEE Transactions on Multi-Scale Computing Systems* 2 (2015), Nr. 1, S. 49–60

[23] Baumgartner, Manuel ; Garello, Kevin ; Mendil, Johannes ; Avci, Can O. ; Grimaldi, Eva ; Murer, Christoph ; Feng, Junxiao ; Gabureac, Mihai ; Stamm, Christian ; Acremann, Yves u. a.:
Spatially and time-resolved magnetization dynamics driven by spin–orbit torques.
In: *Nature nanotechnology* 12 (2017), Nr. 10, S. 980

[24] Baltz, V ; Manchon, Aurelien ; Tsoi, M ; Moriyama, T ; Ono, T ; Tserkovnyak, Y:
Antiferromagnetic spintronics.
In: *Reviews of Modern Physics* 90 (2018), Nr. 1, S. 015005

[25] Jungwirth, T. ; Marti, X. ; Wadley, P. ; Wunderlich, J.:
Antiferromagnetic spintronics.
In: *Nature Nanotechnology* 11 (2016), S. 231–241

[26] Jungwirth, Tomas ; Marti, X ; Wadley, P ; Wunderlich, J:
Antiferromagnetic spintronics.
In: *Nature nanotechnology* 11 (2016), Nr. 3, S. 231

[27] Gomonay, O ; Jungwirth, T ; Sinova, Jairo:
Concepts of antiferromagnetic spintronics.
In: *physica status solidi (RRL)–Rapid Research Letters* 11 (2017), Nr. 4, S. 1700022

[28] Jungfleisch, Matthias B. ; Zhang, Wei ; Hoffmann, Axel:
Perspectives of antiferromagnetic spintronics.
In: *Physics Letters A* 382 (2018), Nr. 13, S. 865–871

[29] Néel, M. Louis:
Propriétés magnétiques des ferrites ; ferrimagnétisme et antiferromagnétisme.
In: *Ann. Phys.* 12 (1948), Nr. 3, S. 137–198

[30] Loth, Sebastian ; Baumann, Susanne ; Lutz, Christopher P. ; Eigler, DM ; Heinrich, Andreas J.:
Bistability in atomic-scale antiferromagnets.
In: *Science* 335 (2012), Nr. 6065, S. 196–199

[31] Baldrati, Lorenzo ; Schmitt, Christin ; Gomonay, Olena ; Lebrun, Romain ; Ramos, Rafael ; Saitoh, Eiji ; Sinova, Jairo ; Kläui, Mathias:
Efficient spin torques in antiferromagnetic CoO/Pt quantified by comparing field-and current-induced switching.
In: *Physical review letters* 125 (2020), Nr. 7, S. 077201

[32] Sulymenko, OR ; Prokopenko, OV:
Generation of THz-frequency electromagnetic signals in antiferromagnetic multilayered nanostructures biased by a spin current.
In: *2017 IEEE International Young Scientists Forum on Applied Physics and Engineering (YSF)* IEEE, 2017, S. 279–282

[33] Sulymenko, OR ; Prokopenko, OV:
Generation of THz-Frequency Electromagnetic Signals in Antiferromagnetic Nano-Oscillators.
In: *2018 IEEE 38th International Conference on Electronics and Nanotechnology (ELNANO)* IEEE, 2018, S. 60–63

[34] Miron, Ioan M. ; Garello, Kevin ; Gaudin, Gilles ; Zermatten, Pierre-Jean ; Costache, Marius V. ; Auffret, Stéphane ; Bandiera, Sébastien ; Rodmacq, Bernard ; Schuhl, Alain ; Gambardella, Pietro:
Perpendicular switching of a single ferromagnetic layer induced by in-plane current injection.
In: *Nature* 476 (2011), Nr. 7359, S. 189–193

[35] Todorovic, Mladen ; Schultz, Sheldon ; Wong, Joyce ; Scherer, Axel:
Writing and reading of single magnetic domain per bit perpendicular patterned media.
In: *Applied Physics Letters* 74 (1999), Nr. 17, S. 2516–2518

[36] Hoffman, Silas ; Tserkovnyak, Yaroslav ; Khalili Amiri, Pedram ; Wang, Kang L.:
Magnetic bit stability: Competition between domain-wall and monodomain switching.
In: *Applied Physics Letters* 100 (2012), Nr. 21, S. 212406

[37] Brown, William F.:
Magnetostatic principles in ferromagnetism. Bd. 1.
North-Holland Publishing Company, 1962

[38] Tanner, BK:
Antiferromagnetic domains.
In: *Contemporary Physics* 20 (1979), Nr. 2, S. 187–210

[39] Teodosiu, Cristian:
Elastic models of crystal defects.

Springer Science & Business Media, 2013

[40] Brown, William F.:
Magnetoelastic interactions. Bd. 9.
Springer, 1966

[41] Callen, Earl R. ; Callen, Herbert B.:
Static magnetoelastic coupling in cubic crystals.
In: *Physical Review* 129 (1963), Nr. 2, S. 578

[42] Giot, Maud ; Chapon, Laurent C. ; Androulakis, John ; Green, Mark A. ; Radaelli, Paolo G. ; Lappas, Alexandros:
Magnetoelastic Coupling and Symmetry Breaking in the Frustrated Antiferromagnet α- NaMnO 2.
In: *Physical review letters* 99 (2007), Nr. 24, S. 247211

[43] Gomonay, Helen ; Loktev, Vadim M.:
Magnetostriction and magnetoelastic domains in antiferromagnets.
In: *Journal of Physics: Condensed Matter* 14 (2002), Nr. 15, S. 3959

[44] Ellis, Matthew O. ; Evans, Richard F. ; Ostler, Thomas A. ; Barker, Joseph ; Atxitia, U ; Chubykalo-Fesenko, O ; Chantrell, Roy W.:
The Landau–Lifshitz equation in atomistic models.
In: *Low Temperature Physics* 41 (2015), Nr. 9, S. 705–712

[45] Bower, Allan F.:
Applied mechanics of solids.
CRC press, 2009

[46] Brown Jr, William F.:
Micromagnetics, domains, and resonance.
In: *Journal of Applied Physics* 30 (1959), Nr. 4, S. S62–S69

[47] Alouges, Francois:
Mathematical models in micromagnetism: an introduction.
In: *ESAIM: Proceedings* Bd. 22 EDP Sciences, 2008, S. 114–117

[48] Cullity, Bernard D. ; Graham, Chad D.:
Introduction to magnetic materials.
John Wiley & Sons, 2011

[49] Slaughter, William S. ; Verlag, B:
The linearized theory of elasticity.
2003

[50] Balluffi, Robert W.:
Introduction to elasticity theory for crystal defects.
World Scientific Publishing Company, 2016

[51] Brown Jr, William F.:
Theory of magnetoelastic effects in ferromagnetism.

In: *Journal of Applied Physics* 36 (1965), Nr. 3, S. 994–1000

[52] Gomonay, Olena ; Kondovych, S ; Loktev, V:
Shape-induced anisotropy in antiferromagnetic nanoparticles.
In: *Journal of magnetism and magnetic materials* 354 (2014), S. 125–135

[53] Hubert, Olivier:
Multiscale magneto-elastic modeling of magnetic materials including isotropic second order stress effect.
In: *Journal of Magnetism and Magnetic Materials* 491 (2019), S. 165564

[54] Kleemann, W ; Schafer, FJ ; Nouet, J:
Structural phase transitions in ferroelastic RbAlF4. II. Linear birefringence investigations.
In: *Journal of Physics C: Solid State Physics* 15 (1982), Nr. 2, S. 197

[55] Levola, T ; Kleemann, W:
Magnetic specific heat and structural phase transitions in (CH 3) 4 NMnCl 3 (TMMC) and TMMC: Cu 2+ studied by crystal optics.
In: *Physical Review B* 32 (1985), Nr. 7, S. 4697

[56] Eshelby, John D.:
The determination of the elastic field of an ellipsoidal inclusion, and related problems.
In: *Proceedings of the royal society of London. Series A. Mathematical and physical sciences* 241 (1957), Nr. 1226, S. 376–396

[57] Eshelby, John D.:
The elastic field outside an ellipsoidal inclusion.
In: *Proceedings of the Royal Society of London. Series A. Mathematical and Physical Sciences* 252 (1959), Nr. 1271, S. 561–569

[58] Sas, Wojciech ; Gabryś, Katarzyna ; Szymański, Alojzy u. a.:
Determination of Poisson's ratio by means of resonant column tests.
In: *Electron. J. Pol. Agricu. Univ. EJPAU* 16 (2013), Nr. 03

[59] Vansteenkiste, Arne ; Leliaert, Jonathan ; Dvornik, Mykola ; Helsen, Mathias ; Garcia-Sanchez, Felipe ; Van Waeyenberge, Bartel:
The design and verification of MuMax3.
In: *AIP advances* 4 (2014), Nr. 10, S. 107133

[60] Eshelby, JD:
Dislocations in visco-elastic materials.
In: *Philosophical Magazine* 6 (1961), Nr. 68, S. 953–963

[61] Rodrigues, Davi R. ; Abanov, Ar ; Sinova, J ; Everschor-Sitte, K:
Effective description of domain wall strings.
In: *Physical Review B* 97 (2018), Nr. 13, S. 134414

[62] Kravchuk, Volodymyr P. ; Gomonay, Olena ; Sheka, Denis D. ; Rodrigues, Davi R. ; Everschor-Sitte, Karin ; Sinova, Jairo ; Brink, Jeroen van d. ; Gaididei, Yuri:
Spin eigenexcitations of an antiferromagnetic skyrmion.
In: *Physical Review B* 99 (2019), Nr. 18, S. 184429

[63] Lamé, Gabriel:
Examen des différentes méthodes employées pour résoudre les problèmes de géométrie.
Mme. Ve. Courcier, imprimeur-libraire, 1818

[64] Loria, Gino:
Spezielle Ebene Algebraische Kurven von Höherer als der Vierten Ordnung.
In: *Geometrie.*
Springer, 1921, S. 571–634

[65] Artin, Emil:
The gamma function.
Courier Dover Publications, 2015

[66] Schmidt, Mikołaj K ; Poulton, Christopher G. ; Steel, Michael J.:
Acoustic diamond resonators with ultrasmall mode volumes.
In: *Physical Review Research* 2 (2020), Nr. 3, S. 033153

[67] Zhang, De-Lin ; Zhu, Jie ; Qu, Tao ; Lattery, Dustin M. ; Victora, RH ; Wang, Xiaojia ; Wang, Jian-Ping:
High-frequency magnetoacoustic resonance through strain-spin coupling in perpendicular magnetic multilayers.
In: *Science advances* 6 (2020), Nr. 38, S. eabb4607

[68] Mondal, Sucheta ; Abeed, Md A. ; Dutta, Koustuv ; De, Anulekha ; Sahoo, Sourav ; Barman, Anjan ; Bandyopadhyay, Supriyo:
Hybrid magnetodynamical modes in a single magnetostrictive nanomagnet on a piezoelectric substrate arising from magnetoelastic modulation of precessional dynamics.
In: *ACS applied materials & interfaces* 10 (2018), Nr. 50, S. 43970–43977

[69] Dasgupta, Sayak ; Kim, Se K. ; Tchernyshyov, Oleg:
Gauge fields and related forces in antiferromagnetic soliton physics.
In: *Physical Review B* 95 (2017), Nr. 22, S. 220407

[70] Kac, Mark u. a.:
PM Morse and H. Feshbach, Methods of theoretical physics.
In: *Bulletin of the American Mathematical Society* 62 (1956), Nr. 1, S. 52–54

[71] Griffiths, David J. ; Schroeter, Darrell F.:
Introduction to quantum mechanics.
Cambridge University Press, 2018

[72] Fröman, Nanny ; Fröman, Per O.:
JWKB approximation: contributions to the theory.
(1965)

[73] Inc., Wolfram R.:
Mathematica, Version 12.2. –
Champaign, IL, 2020

[74] Bogdanov, AN ; Zhuravlev, AV ; Rössler, UK:
Spin-flop transition in uniaxial antiferromagnets: Magnetic phases, reorientation effects, and multidomain states.
In: *Physical Review B* 75 (2007), Nr. 9, S. 094425

[75] Meer, Hendrik ; Schreiber, Felix ; Schmitt, Christin ; Ramos, Rafael ; Saitoh, Eiji ; Gomonay, Olena ; Sinova, Jairo ; Baldrati, Lorenzo ; Kläui, Mathias:
Direct Imaging of Current-Induced Antiferromagnetic Switching Revealing a Pure Thermomagnetoelastic Switching Mechanism in NiO.
In: *Nano Letters* (2020)

[76] Bronstein, Ilja N. ; Semendjaev, Konstantin A.:
Taschenbuch der Mathematik. Bd. 21.
Verlag Harri Deutsch, 1982

[77] Bracewell, Ronald N. ; Bracewell, Ronald N.:
The Fourier transform and its applications. Bd. 31999.
McGraw-Hill New York, 1986